2019

Synthesis and advanced spectroscopy of new and emerging energy materials

Bryan Anthony Rosales
Iowa State University

Synthesis and advanced spectroscopy of new and emerging energy materials

by

Bryan A. Rosales

A dissertation submitted to the graduate faculty

in partial fulfillment of the requirements for the degree of

DOCTOR OF PHILOSOPHY

Major: Chemistry

Program of Study Committee:

Javier Vela, Major Professor
Aaron Rossini
Emily Smith
Gordon Miller
Wenyu Huang

The student author, whose presentation of the scholarship herein was approved by the program of study committee, is solely responsible for the content of this dissertation. The Graduate College will ensure this dissertation is globally accessible and will not permit alterations after a degree is conferred.

Iowa State University

Ames, Iowa

2019

TABLE OF CONTENTS

ACKNOWLEDGEMENTS

I would like to thank my advisor, Javier Vela, for his guidance, support, and encouragement throughout my graduate studies. His constructive criticism and lengthy scientific debates trained me to be a skilled researcher with an eye for detail. I would also like to thank Aaron Rossini, Emily Smith, Matthew Panthani, and their groups for prosperous collaborations and invaluable discussions. Special thanks to Gordie Miller and Wenyu Huang for providing guidance and asking difficult questions, my research benefited immensely. Special thanks for Sarah Cady for all the NMR guidance and invaluable discussions.

Thanks to all Vela group members, past and present, for all of their support. A special thanks to Arthur (Miles) White for all the lengthy discussions and willingness to critique my ideas. Thanks to Long Men and Himashi Andaraarachchi for all the good times, laughter, and discussions throughout the years. Thanks to Alan Medina-Gonzalez, Carena Daniels, Lin Wei, Yunhua Chen, Marquix Adamson, Phil Yox, Kate Baumler, and Rafa Blome for their friendship and group lunches! Many thanks to Josie Del Pilar for all the guidance, Michelle Thompson for all the laughter, and Feng Zhu for teaching me about perovskites.

Special thanks to my wife, Ann Lii-Rosales, for being my pillar of support throughout the years. Your patience, love, support, laughter, and invaluable research discussions gave me the strength I needed every day throughout my graduate studies. Thank you for always being with me through every step of this adventure.

ABSTRACT

As the global population increases and our dependence on technology grows, we need to develop technologies that can generate energy cleanly and efficiently without releasing harmful pollutants into the environment. This dissertation describes the synthesis and characterization of new and emerging solar cell materials including methylammonium lead mixed halide perovskites, cesium germanium halide perovskites, and alkali bismuth dichalcogenides.

We begin by characterizing the methylammonium lead mixed halide perovskites by ^{207}Pb solid state nuclear magnetic resonance (ssNMR) spectroscopy. When these materials are prepared in solution, we observe the presence of dopants and semicrystalline phases that survive and persist even upon annealing. We develop a novel solid phase synthesis that successfully eliminates these semicrystalline phases; however, dopants still persist. Our results are consistent with the presence of miscibility gaps and spontaneous spinodal decomposition of mixed-halide perovskites at room temperature. These results suggest that better optoelectronic properties and improved device performance may be achieved through careful manipulation of the different phases and nanodomains present in these materials.

Next, because many technologically relevant semiconductors are composed of toxic (Cd, Pb, As) or relatively scarce (Li, In) elements, we describe the synthesis of nanocrystals of two new ternary semiconductor families: cesium germanium halide perovskites and alkali bismuth dichalcogenides. We achieve size control of cesium germanium halide perovskite nanocrystals by varying cysteammonium halide ligands in an aqueous synthesis. We observe a variety of morphologies including pyramidal, hexagonal, and spheroidal. We successfully dope Mn^{2+} into the lattice for the first time with incorporations up to 29% in bulk and 16% in nano samples. We also report a facile, low-temperature, and size-tunable (4–28 nm) solution phase synthesis of ternary alkali bismuth dichalcogenides. We observe 1.20–1.45 eV band gaps that all fall within the ideal range for solar cells with high extinction coefficients in the 10^4–10^6 cm^{-1} M^{-1} range. We computationally investigate the lowest energy superstructures that result from “coloring” that is caused by mixed-cation sites present in the rock salt lattice. The syntheses reported in this dissertation unlock two new classes of low cost and environmentally friendly semiconductors that show properties of interest for applications in energy conversion.

CHAPTER 1

INTRODUCTION

General introduction

This dissertation presents investigations into two different multinary semiconductor systems: halide perovskites and alkali bismuth dichalcogenides. Both systems are new and emerging semiconductors with properties desirable for light harvesting applications such as solar cells. Phase segregation in the methylammonium lead mixed halide perovskites is investigated by ^{207}Pb ssNMR and a novel solid phase synthetic method that successfully eliminates semicrystalline phases is reported. Next, because many of the best semiconducting materials are based on toxic heavy metals, we report synthetic tunability of colloidal semiconductor nanocrystals based on comparatively benign (germanium halide perovskites) and biocompatible (alkali bismuth dichalcogenides) elements.

Semiconductors and photovoltaic cells

Because of the large number of atoms in a solid, the number of orbitals and closely spaced energy levels are also large such that bands of energy levels exist instead of the discrete energy levels found in molecules.[1] The valence band is the highest energy band containing electrons while the conduction band is the lowest energy band void of electrons. If there is no energy difference between these bands as is the case in a metal (Figure 1), little to no energy is required to move electrons between the bands allowing electrons to move freely throughout the lattice (Figure 1). If there is a band gap caused by an energy difference between these bands as is the case for semiconductors and insulators, then energy must be supplied to the system to promote an electron from the valence band to the conduction band. The band gap energy of a semiconductor is small enough such that it fits within the solar radiation spectrum while the band gap of an insulator is large such that only the highest energy photons can excite an electron.

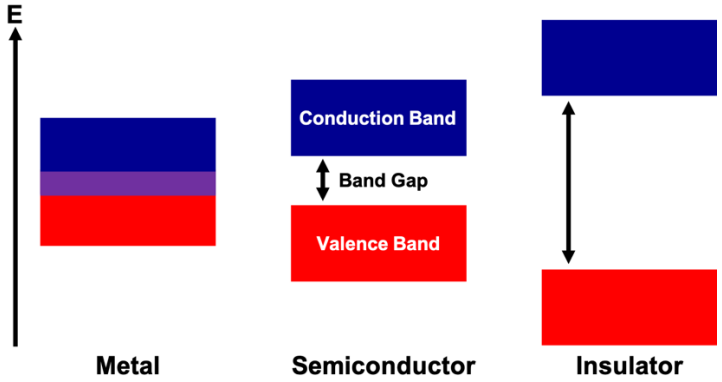

Figure 1. Illustration of the difference in energy levels for metals, semiconductors, and insulators.

The atoms in a solid are bonded to each other repetitively throughout a three-dimensional lattice. Because of this, the energy difference between the valence band and conduction band changes depending on the direction one looks in the brillouin zone of reciprocal space as shown by the band structure (Figure 2b and 2c, red lines). There is a direction in the brillouin zone that minimizes the energy difference between the valence band maximum (Figure 2b and 2c, bottom red line) and conduction band minimum (Figure 2b and 2c, top red line). If the valence band maximum and conduction band minimum occupy the same location in reciprocal space, the semiconductor is called a *direct band gap semiconductor* (Figure 2b) and a photon only needs to be the appropriate energy to be absorbed.[2] If the valence band maximum and conduction band minimum occupy different locations in reciprocal space, the semiconductor is called an in*direct band gap semiconductor* (Figure 2c) and the photon not only needs to be the appropriate energy but also needs to interact with a phonon by transferring momentum to be absorbed.[2] Direct band gap semiconductors exhibit a steep absorption coefficient onset with values typically between 10^4-10^6 cm^{-1} while indirect band gap semiconductors exhibit a broad absorption coefficient onset with values typically $< 10^3$ cm^{-1}.[2] It is also possible to have close-in-energy direct and indirect band gaps. For example, MoS_2 and $MoSe_2$ can transition from indirect band gap to direct band gap as the dimensionality of the material is reduced from a bulk crystal to a single layer (Figure 2b vs 2c) accompanied by a substantial photoluminescence enhancement (Figure 2a).[3-4]

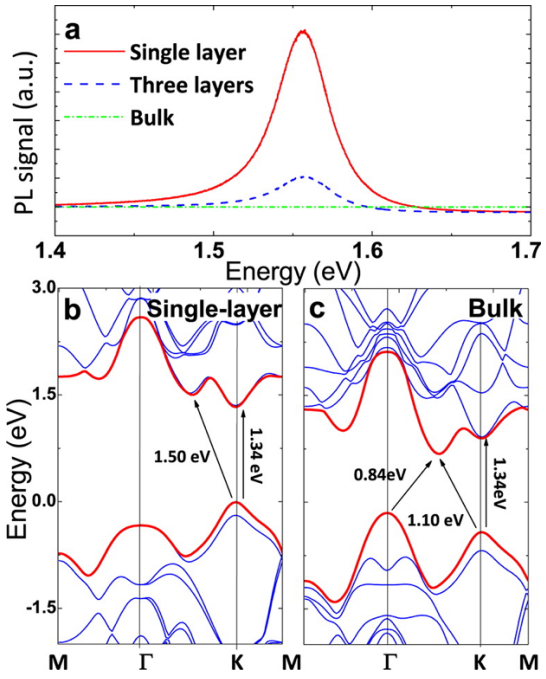

Figure 2. (a) PL of single-layer (red), three layers (blue dashed), and bulk (green dotted) $MoSe_2$. (b-c) Calculated band structure of single-layer and bulk $MoSe_2$. Reprinted with permission from ref. 3. Copyright 2012 American Chemical Society.

The properties of a semiconductor can be modified through doping.[1] When the added atoms contain more electrons in the valence shell compared to the host material, the result is a more negative material called an n-type semiconductor. When the added atoms contain fewer electrons in the valence shell, the result is a more positive material called a p-type semiconductor.

A p-n junction is created when a p-type semiconducting layer is connected to an n-type semiconducting layer (Figure 3a).[1] Excess electrons from the n-type layer will migrate to the p-type layer until an equilibrium is reached. At this point, the band gap of both layers is unchanged with the Fermi levels matching because the energy levels of the n-type layer are lowered by buildup of positive charge. If no external voltage is applied, photons of energy equal to or greater than the band gap can promote an electron from the valence band of the p-type layer into the conduction band of the n-type layer. Current can then be collected when the two layers are connected by an external circuit (Figure 3a). This process is known as the *photovoltaic effect* and optoelectronic device such as solar cells use this process to generate electricity from sunlight.

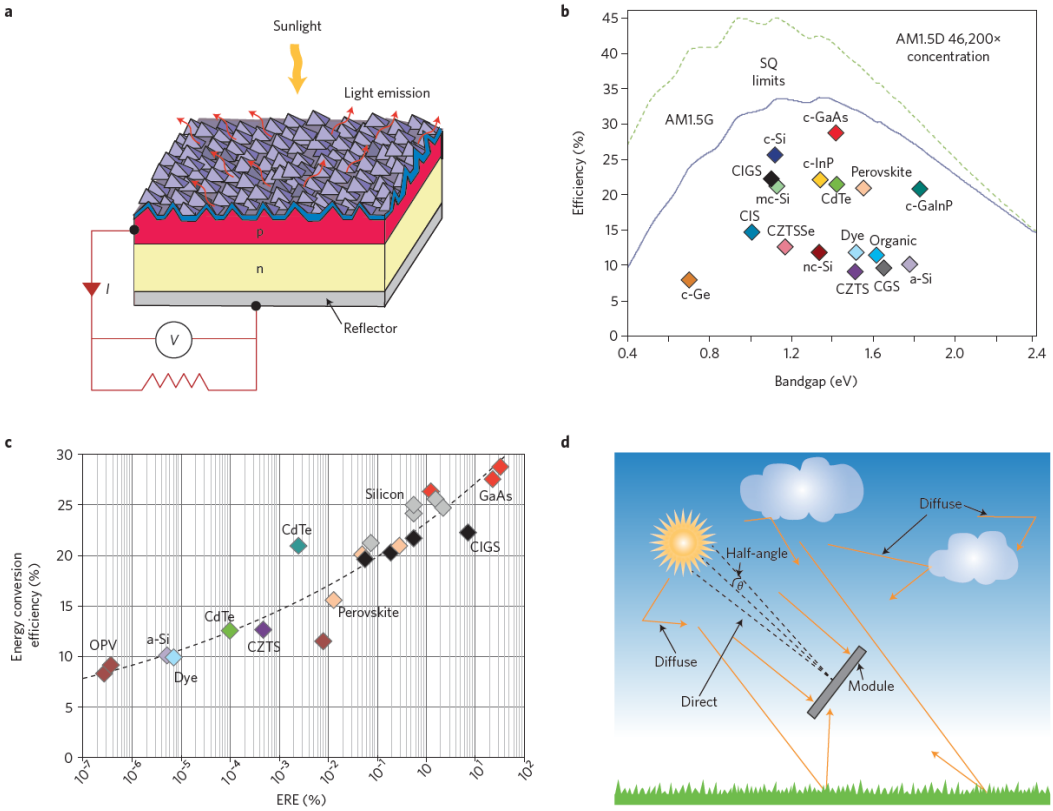

Figure 3. (a) Light absorption and emission from a solar cell under load. Current is collected from a p-n junction when connected to an external circuit. (b) Shockley-Queisser energy conversion efficiency limits under global sunlight (AM1.5G) versus band gap (solid line). The highest experimental values for various materials are shown as colored diamonds. Dashed line shows limits for direct AM1.5D sunlight conversion under maximal concentration of 46,200 suns at a cell temperature of 25 °C. (c) Energy conversion efficiency versus external radiative efficiency (ERE) for various experimental cells. (d) Angular effects in solar energy conversion, showing direct and diffuse solar components, minimum acceptance angle, and ground reflection effects. Reprinted by permission from Springer Nature: ref. #5, Copyright 2017.

While the band gap of a semiconductor is necessary to convert sunlight into electricity, the size of the band gap limits the maximum power conversion efficiency (PCE) obtainable in a solar cell. Photons of energy lower than the band gap are not absorbed while photons of higher energy are absorbed; however, only part of the energy is used to excite electrons across the band gap while the rest of the energy increases the kinetic energy of the electron (known as "hot" electrons).[6] As

hot electrons move throughout the lattice, they lose their kinetic energy in the form of heat due to lattice scattering.[6] These loss mechanisms lead to an ideal band gap range in which the band gap is neither too large nor too small. After taking these spectral losses into account along with blackbody radiation losses, recombination losses, and impedance mismatching, a fundamental PCE limit called the Shockley-Queisser limit can be calculated.[7] This limit results in a maximum PCE of 33.7% at a band gap of 1.34 eV, although PCE's above 30% are possible in a band gap range of 1.0-1.6 eV (Figure 3b).[8] The Shockley-Queisser limit is specific to single-junction solar cells and there are a variety of ways one could overcome this limit including (but not limited to) concentrating sunlight (Figure 3b, dashed line), changing the acceptance angle (Figure 3d), controlling the cell operating temperature, forming multijunction solar cells, multiple exciton generation (MEG), and incident photon wavelength manipulation.[5]

Many of the best performing solar cell materials contain toxic, heavily regulated (Cd, Pb, As) elements as well as elements that are scarce or poorly distributed in the Earth's crust (In) (Figure 3b). Therefore, much effort has gone towards developing new semiconductors based on environmentally friendly and Earth abundant elements.[9-11] Computationally screening these new semiconductors relies on identifying properties commonly found in the best performing solar cell materials and then calculating these properties for a series of new semiconductors.[12-14] Among the properties desirable that are typically calculated include the magnitude and nature of the band gap, strength of optical absorption, charge carrier effective masses, defect tolerance, dielectric constant, Rashba splitting, and band alignment with commonly used contact materials.[12]

Colloidal semiconductor nanocrystals

Nanocrystals are tiny crystalline particles with sizes in the range of 1–100 nm. While a bulk solid exhibits continuous energy states that behave as bands, the energy spacing between these states begin to increase as the size of the crystal decreases.[15] When the size becomes smaller than the Bohr exciton radius, the exciton becomes spatially confined which raises its energy.[15] A nanocrystal with size-dependent optical and electronic properties as a result of this quantum confinement effect are called *quantum dots* (Figure 4). By changing the size of a quantum dot, one can change what wavelengths of light are absorbed.

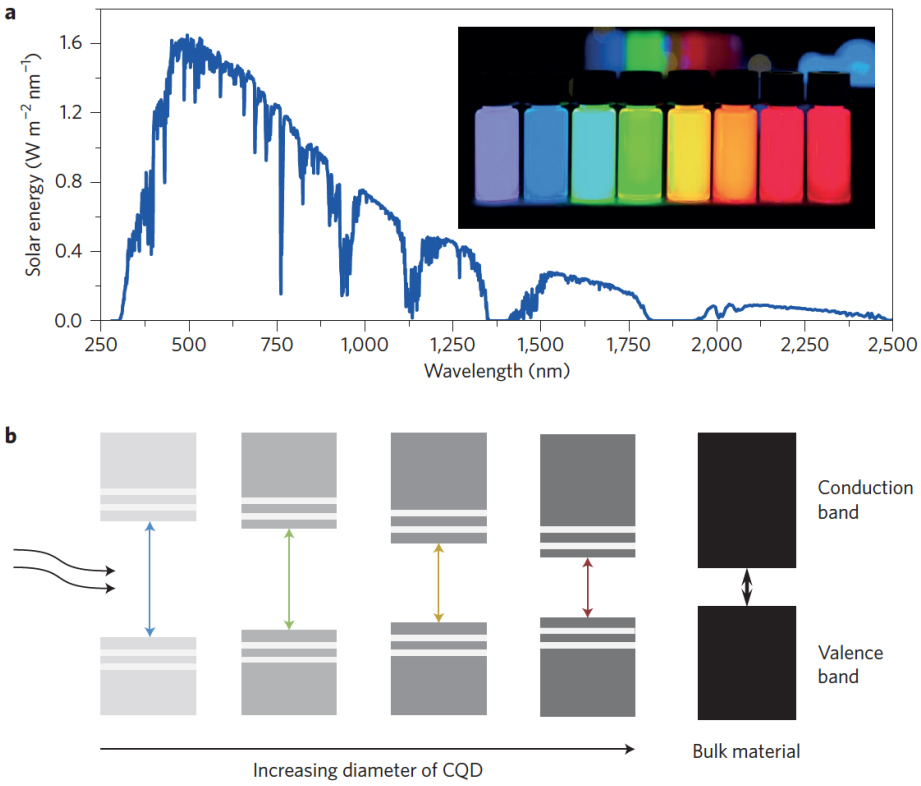

Figure 4. (a) Nanocrystal size-dependent absorption enables tuning of the quantum dot absorption spectrum. The insert shows photoluminescence of quantum dots with different crystal sizes. (b) The conduction and valence band energy levels also depend on nanocrystal size. Reprinted by permission from Springer Nature: ref. #16, Copyright 2016.

Another effect of nanostructuring is that the surface area increases as the size is reduced. With shrinking size, the role of the surface increases until it becomes the dominant factor.[17] Therefore, an understanding of the underlying surface chemistry is imperative when discussing the properties of a particular nanocrystal system.

The surface of a nanocrystal can accommodate a variety of surface ligands with designated X-, L-, and Z-type classification (Figure 5a).[18-19] X-type ligands are strongly binding, negatively charged ligands such as carboxylates or halides that can terminate a cation-rich lattice or exist as a bound ion pair. L-type ligands are weakly binding neutral donor ligands such as oleylNH_2 or PR_3 that bind to surface cations. Z-type ligands are neutral acceptor ligands such as $CdCl_2$ or PbI_2 that effectively bind to negatively charged surface species. The type of nanocrystal surface can change the nature of how the ligand binds to the surface. One example is PbS whose nanocrystals adopt

two different surface planes: a Pb-only (111) surface and a mixed Pb/S (100) surface.[17] Pb-rich (111) planes lead to favorable binding of negatively charged oleate ligands on the Pb sites while the mixed Pb/S sulfur sites of (100) lead to bidentate binding of oleic acid as an L-type ligand (Figure 5).[17]

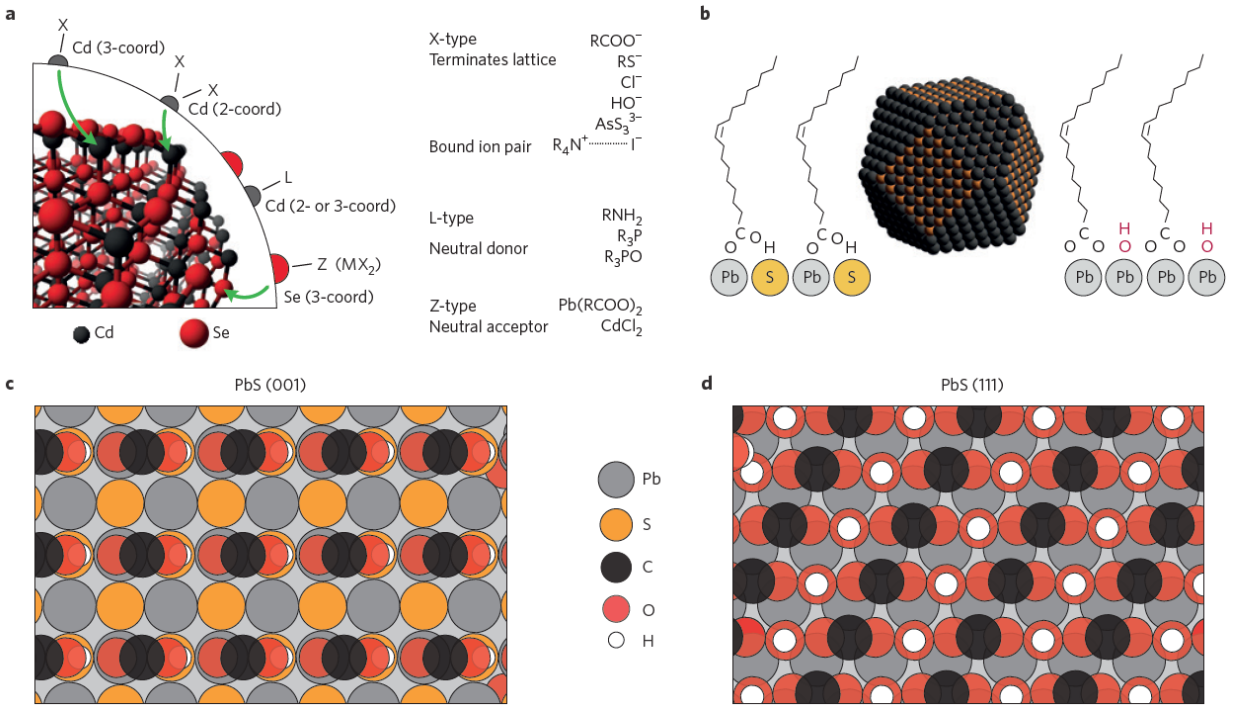

Figure 5. (a) Classification of ligand binding motifs at the surface of a CdSe nanocrystal. (b) Modelled 5-nm cuboctahedral PbS NC (center) with simplified illustrations of oleic acid binding as L-type ligand to (100) facets (left) and binding together with hydroxide as X-type oleate on Pb-terminated (111) facets (right). (c,d) Sketches of DFT-relaxed surface structure on PbS(100) and PbS(111). Reprinted by permission from Springer Nature: ref. #17, Copyright 2016.

Dangling bonds on the surface caused by incomplete surface passivation causes mid-gap trap states to form between the valence and conduction bands (Figure 6a *vs.* 6b).[16] Mid-gap trap states greatly affect the optoelectronic properties of nanocrystals. Films composed of nanocrystals exhibiting extensive mid-gap trap states are prone to a decrease in both the effective carrier mobility and exciton diffusion length.[16] Mid-gap trap states act as recombination centers that reduce the exciton excited state lifetime leading to an increase in exciton loss due to

photoluminescence (Figure 6c).[16] Therefore, much research has gone into developing effective ligand exchange methods that both remove native bulky organic ligands and completely passivate the surface with conducting short-chain inorganic ligands commonly based on metal or organic halides. One effective method is layer-by-layer (LBL) ligand exchange in which the nanocrystal solid is first assembled into a densely packed film and then soaked in a ligand exchange solution that contains additional passivants.[16] The steric hindrance of the bulky organic ligands can prevent complete ligand exchange and can even limit the access of passivants to the surface.[16] Nonetheless, record quantum dot solar cell power conversion efficiencies exceeding 13% can be achieved by this method.[20] Alternatively, more complete ligand exchange and greater surface passivation can be achieved by introducing halide ligands during synthesis or by performing a biphasic ligand exchange in solution.[16]

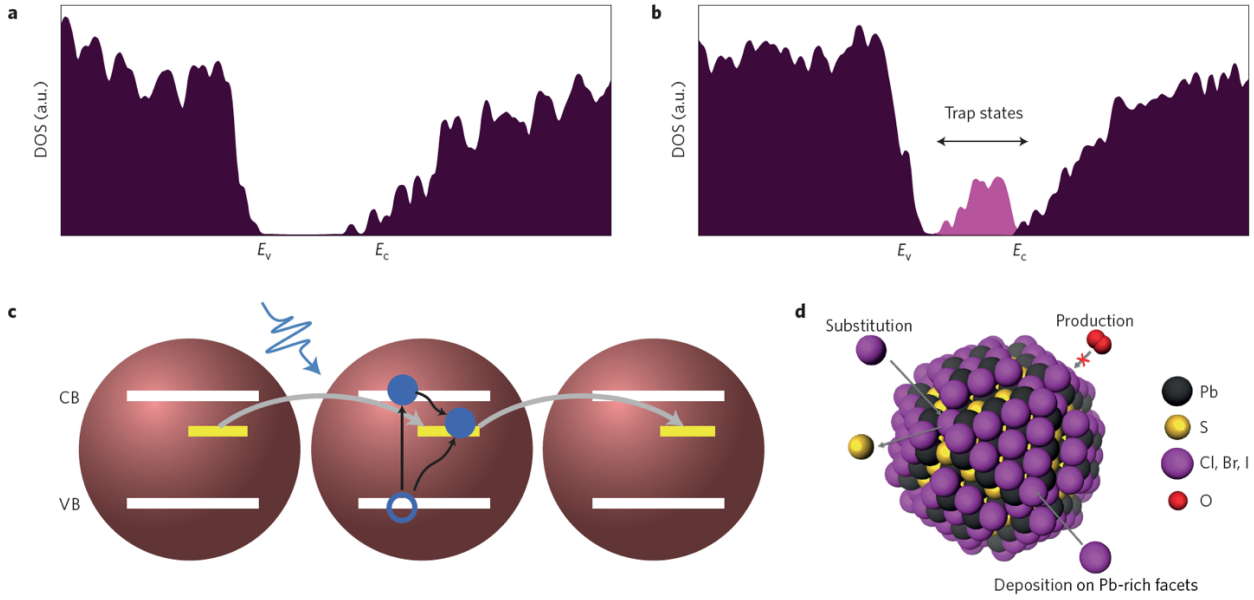

Figure 6. Density of states showing a band gap without (a) and with (b) mid-gap trap states. E_v is the energy level of the top of the valence band and E_c is the energy level of the bottom of the conduction band. (c) Mid-gap states (yellow) function as recombination centers, capturing both electrons (blue spheres) and holes (blue circles) with similar probabilities, and enabling their loss through recombination. VB is the valence band and CB is the conduction band; wavy arrow represents incoming photons. (d) Effective surface passivation seeks to eliminate electronic states within the band gap. Reprinted by permission from Springer Nature: ref. #16, Copyright 2016.

These methods enable a variety of quantum dot devices that can be made by depositing quantum dots from solution after engineering their size, shape, and surface chemistry.[21] Among devices that can be made from quantum dots include field-effect transistors, photoresistors, light-emitting diodes, and solar cells. However, challenges still remain for quantum dot devices including control over carrier type, concentration, mobility, and traps at the device interface that can limit the gain and speed of quantum dot electronics.[21]

References

(1) Miessler, G. L.; Fischer, P. J.; Tarr, D. A., *Inorganic Chemistry*; 5 ed.; Pearson Education: **2013**.

(2) Zimmermann, H., Basics of Optical Emission and Absorption. In *Integrated Silicon Optoelectronics*, Zimmermann, H. K., Ed. Springer Berlin Heidelberg: Berlin, Heidelberg, 2010; pp 1-9.

(3) Tongay, S.; Zhou, J.; Ataca, C.; Lo, K.; Matthews, T. S.; Li, J. B.; Grossman, J. C.; Wu, J. Q. Thermally Driven Crossover from Indirect toward Direct Bandgap in 2D Semiconductors: $MoSe_2$ Versus MoS_2. *Nano Lett.* **2012,** *12*, 11, 5576-5580.

(4) Mak, K. F.; Lee, C.; Hone, J.; Shan, J.; Heinz, T. F. Atomically Thin MoS_2: A New Direct-Gap Semiconductor. *Phys. Rev. Lett.* **2010,** *105*, 13, 136805.

(5) Green, M. A.; Bremner, S. P. Energy Conversion Approaches and Materials for High-Efficiency Photovoltaics. *Nat. Mater.* **2017,** *16*, 1, 23-34.

(6) Solanki, C. S.; Beaucarne, G. Advanced Solar Cell Concepts. *Energy Sustain. Dev.* **2007,** *11*, 3, 17-23.

(7) Shockley, W.; Queisser, H. J. Detailed Balance Limit of Efficiency of p-n Junction Solar Cells. *J. Appl. Phys.* **1961,** *32*, 3, 510-519.

(8) Rühle, S. Tabulated Values of the Shockley–Queisser Limit for Single Junction Solar Cells. *Solar Energy* **2016,** *130*, 139-147.

(9) Lee, L. C.; Huq, T. N.; MacManus-Driscoll, J. L.; Hoye, R. L. Z. Research Update: Bismuth-Based Perovskite-Inspired Photovoltaic Materials. *APL Mater.* **2018,** *6*, 8, 084502.

(10) Miller, N. C.; Bernechea, M. Research Update: Bismuth Based Materials for Photovoltaics. *APL Mater.* **2018,** *6*, 8, 084503.

(11) Lyu, M.; Yun, J.-H.; Chen, P.; Hao, M.; Wang, L. Addressing Toxicity of Lead: Progress and Applications of Low-Toxic Metal Halide Perovskites and Their Derivatives. *Adv. Energy Mater.* **2017,** *7*, 15, 1602512.

(12) Ganose, A. M.; Savory, C. N.; Scanlon, D. O. Beyond Methylammonium Lead Iodide: Prospects for the Emergent Field of ns^2 Containing Solar Absorbers. *Chem. Commun.* **2017,** *53*, 1, 20-44.

(13) Brandt, R. E.; Poindexter, J. R.; Gorai, P.; Kurchin, R. C.; Hoye, R. L. Z.; Nienhaus, L.; Wilson, M. W. B.; Polizzotti, J. A.; Sereika, R.; Žaltauskas, R.; Lee, L. C.; MacManus-Driscoll, J. L.; Bawendi, M.; Stevanović, V.; Buonassisi, T. Searching for "Defect-Tolerant" Photovoltaic Materials: Combined Theoretical and Experimental Screening. *Chem. Mater.* **2017,** *29*, 11, 4667-4674.

(14) Brandt, R. E.; Stevanovic, V.; Ginley, D. S.; Buonassisi, T. Identifying Defect-Tolerant Semiconductors with High Minority-Carrier Lifetimes: Beyond Hybrid Lead Halide Perovskites. *MRS Commun.* **2015,** *5*, 2, 265-275.

(15) Smith, A. M.; Nie, S. Semiconductor Nanocrystals: Structure, Properties, and Band Gap Engineering. *Acc. Chem. Res.* **2010,** *43*, 2, 190-200.

(16) Yuan, M.; Liu, M.; Sargent, E. H. Colloidal Quantum Dot Solids for Solution-Processed Solar Cells. *Nat. Energy* **2016,** *1*, 16016.

(17) Boles, M. A.; Ling, D.; Hyeon, T.; Talapin, D. V. The Surface Science of Nanocrystals. *Nat. Mater.* **2016,** *15*, 2, 141-153.

(18) Anderson, N. C.; Hendricks, M. P.; Choi, J. J.; Owen, J. S. Ligand Exchange and the Stoichiometry of Metal Chalcogenide Nanocrystals: Spectroscopic Observation of Facile Metal-Carboxylate Displacement and Binding. *J. Am. Chem. Soc.* **2013,** *135*, 49, 18536-18548.

(19) Owen, J. The Coordination Chemistry of Nanocrystal Surfaces. *Science* **2015,** *347*, 6222, 615-616.

(20) Sanehira, E. M.; Marshall, A. R.; Christians, J. A.; Harvey, S. P.; Ciesielski, P. N.; Wheeler, L. M.; Schulz, P.; Lin, L. Y.; Beard, M. C.; Luther, J. M. Enhanced Mobility $CsPbI_3$ Quantum Dot Arrays for Record-Efficiency, High-Voltage Photovoltaic Cells. *Sci. Adv.* **2017,** *3*, 10.

(21) Kagan, C. R.; Lifshitz, E.; Sargent, E. H.; Talapin, D. V. Building Devices from Colloidal Quantum Dots. *Science* **2016,** *353*, 6302.

CHAPTER 2

PERSISTENT DOPING AND PHASE SEGREGATION IN ORGANOLEAD MIXED HALIDE PEROVSKITES

Reprinted with permission from *Chem. Mater.* **2016**, *28*, 6848–6859.

Bryan A. Rosales, Long Men, Sarah D. Cady, Michael P. Hanrahan, Aaron J. Rossini, and Javier Vela

Abstract

Organolead mixed-halide perovskites such as $CH_3NH_3PbX_{3-a}X'_a$ (X, X' = I, Br, Cl) are interesting semiconductors because of their low cost, high photovoltaic power conversion efficiencies, enhanced moisture stability, and band gap tunability. Using a combination of optical absorption spectroscopy, powder X-ray diffraction (XRD) and, for the first time, ^{207}Pb solid state nuclear magnetic resonance (ssNMR), we probe the extent of alloying and phase segregation in these materials. Because ^{207}Pb ssNMR chemical shifts are highly sensitive to local coordination, electronic structure, and vary linearly with halogen electronegativity and band gap, this technique can provide the true chemical speciation and composition of organolead mixed-halide perovskites. We specifically investigate samples made by three different preparative methods: solution phase synthesis, thermal annealing, and solid phase synthesis. ^{207}Pb ssNMR reveals that nonstoichiometric dopants and semicrystalline phases are prevalent in samples made by solution phase synthesis. We show that these nanodomains are persistent after thermal annealing up to 200 °C. Further, a novel solid phase synthesis that starts from the parent, single-halide perovskites can suppress phase segregation but not the formation of dopants. Our observations are consistent with the presence of miscibility gaps and spontaneous spinodal decomposition of the mixed-halide perovskites at room temperature. This underscores how strongly different synthetic procedures impact the nanostructuring and composition of organolead halide perovskites. Better optoelectronic properties and improved device stability and performance may be achieved through careful manipulation of the different phases and nanodomains present in these materials.

Introduction

Organolead halide perovskites ($CH_3NH_3PbX_3$, X = I, Br, Cl) have emerged as promising semiconductors for photovoltaics due to their low cost, solution processability, and high power conversion efficiencies (> 21-22%).[1,2] Among their many interesting properties, organolead halide perovskites benefit from large absorption coefficients, low exciton binding energies, long exciton diffusion lengths, high dielectric constants, and intrinsic ferroelectric polarization.[3-15] Organolead mixed-halide perovskites ($CH_3NH_3PbX_{3-a}X'_a$, X, X' = I, Br, Cl) are of particular interest because they appear to further benefit from enhanced moisture stability, improved carrier relaxation time, and visible range tunability. Mixed-halide perovskites are thus useful in tandem solar cells and, because they also display intense photoluminescence, they have potential utility in light-emitting devices (LEDs).[16-37]

In spite of these advantages, questions surrounding the extent of alloying and phase segregation in mixed-halide perovskites remain. Films of $CH_3NH_3PbI_{3-x}Cl_x$ cast from precursors that contain chloride exhibit improved film coverage, tunable morphologies, increased diffusion lengths, and reduced photocurrent hysteresis compared to $CH_3NH_3PbI_3$ films prepared without chloride, even though no chloride is present by compositional analysis.[38-44] Whether chloride is incorporated into the structure is uncertain, but it has been suggested that residual chloride collects at grain boundaries.[45] In the *'$CH_3NH_3PbI_{3-a}Br_a$'* series, a recent computational study proposed that bromide-rich phases such as $CH_3NH_3PbIBr_2$ and $CH_3NH_3PbI_{0.5}Br_{2.5}$ can be thermodynamically stable against phase segregation at room temperature; however, a miscibility gap between 30-60% Br is only overcome above 70 °C.[46] Photo-induced phase segregation of organolead mixed-halide perovskites has also been observed.[47-49]

Structural issues aside, phase segregation in mixed-halide perovskites is intriguing because these materials are known to easily undergo anion exchange in solution[50-54] as well as between gas and solid phases.[55] In fact, the fast rate of diffusion and high overall mobility of halide ions throughout the crystalline perovskite lattice[55] is likely responsible for photoinduced phase separation and other unusual perovskite properties such as giant dielectric constant and photocurrent hysteresis.[56,57] More research is needed to understand whether (and which) mixed-halide perovskites form stable alloys, what other phases and impurities exist as phase-segregated domains, and how the various synthetic procedures available affect the true composition, speciation, and optoelectronic properties of these materials.

Among the techniques best suited for the study of organolead halide perovskites is ^{207}Pb solid state (ss) NMR.[58-61] The ^{207}Pb nucleus has a spin of ½, 22.6% natural abundance, and a chemical shift (δ) range spanning over 10,000 ppm.[62] All of these factors make ^{207}Pb ssNMR highly sensitive to local electronic structure, coordination environment, ligand electronegativity, and temperature. For example, the ^{207}Pb

isotropic chemical shift (δ_{iso}) of the lead dihalides (PbX_2; X = I, Br, Cl) varies linearly with halide electronegativity and ionization energy (see Supporting Information (S.I.) available).[62-67] Because the ^{207}Pb nucleus is highly sensitive to local electronic structure, ^{207}Pb ssNMR can probe all crystalline, semicrystalline, and amorphous phases, and provide information about the different lead sites that may be present in mixed-halide perovskites. However, there is currently a dearth of prior ^{207}Pb ssNMR studies on organolead perovskites. ^{2}H and ^{14}N ssNMR were used to observe phase transitions and probe dynamic motions of the $CH_3NH_3^+$ cations in $CH_3NH_3PbX_3$.[68-69] ^{1}H longitudinal relaxation times and ^{35}Cl, ^{79}Br and ^{127}I NQR spectra were used to study the motion and phase transitions in $CH_3NH_3PbX_3$.[70] Very recently, ^{1}H and ^{13}C ssNMR spectra of a variety of lead perovskites were presented.[71]

Herein, we use ^{207}Pb ssNMR to unveil the presence of both nonstoichiometric dopants and phase segregation in organolead mixed-halide perovskites. To the best of our knowledge, this is the first spectroscopic study of these materials using this technique. We find that ^{207}Pb ssNMR is uniquely complementary to other more commonly used characterization methods such as UV-Vis optical absorption and powder X-ray diffraction. Using all of these techniques together, we find that dopants are persistent in perovskites even after thermal annealing to 200 °C. Moreover, these non-stoichiometric impurities form spontaneously regardless of whether the sample is made by solution phase synthesis, thermal annealing, or solid phase synthesis. In contrast, phase segregation, forming semicrystalline or amorphous products, occurs when the sample is made by solution phase synthesis and thermal annealing, but not by solid phase synthesis. We explain these differences in the context of recent studies on the miscibility and spinodal decomposition tendencies of organolead mixed-halide perovskites.

Results and discussion

S*olution phase synthesis.* Organolead single- and mixed-halide perovskites ($CH_3NH_3PbX_3$) can be easily prepared by precipitation from solution (see Methods). In this solution phase synthesis, lead(II)- and methylammonium-halides are dissolved in N,N-dimethylformamide (DMF, X = Br, Cl) or acetonitrile (CH_3CN, X = I) followed by precipitation of the desired perovskite by the addition of toluene (Scheme 1a). A progressive blue shift in absorption edge, along with a color change from black to white, are immediately obvious as the perovskite composition changes from the less electronegative iodide to the more electronegative bromide and chloride (Figure 1a). Iodo-bromide and bromo-chloride perovskites such as *'$CH_3NH_3PbI_{1.5}Br_{1.5}$'* and *'$CH_3NH_3PbBr_{1.5}Cl_{1.5}$'*, respectively, have absorption edges that lie in between those of the parent, single-halide perovskites. In contrast, the absorption edges of iodo-chloride perovskites such as *'$CH_3NH_3PbI_{1.5}Cl_{1.5}$'* mirror that of $CH_3NH_3PbI_3$ (Figure 1b). Note: Throughout this manuscript, *hypothetical formulas calculated from the synthetic loading alone are*

italicized and written in quotation marks whereas actual compositional assignments determined from all of the experimental data combined are written in regular script (see below).

Scheme 1 (X, X' = I, Br, Cl; 3 > a > 0)

(a) *Solution phase synthesis*

$$\left(\frac{3-a}{3}\right)PbX_2 + \left(\frac{3-a}{3}\right)CH_3NH_3X \xrightarrow[(2)\ \text{toluene}]{(1)\ \text{polar solvent}} \text{`}CH_3NH_3PbX_{3-a}X'_a\text{'}$$

$$\left(\frac{a}{3}\right)PbX'_2 + \left(\frac{a}{3}\right)CH_3NH_3X'$$

(b) *Solid phase synthesis*

$$\left(\frac{3-a}{3}\right)CH_3NH_3PbX_3 + \left(\frac{a}{3}\right)CH_3NH_3PbX'_3 \xrightarrow{\Delta} \text{`}CH_3NH_3PbX_{3-a}X'_a\text{'}$$

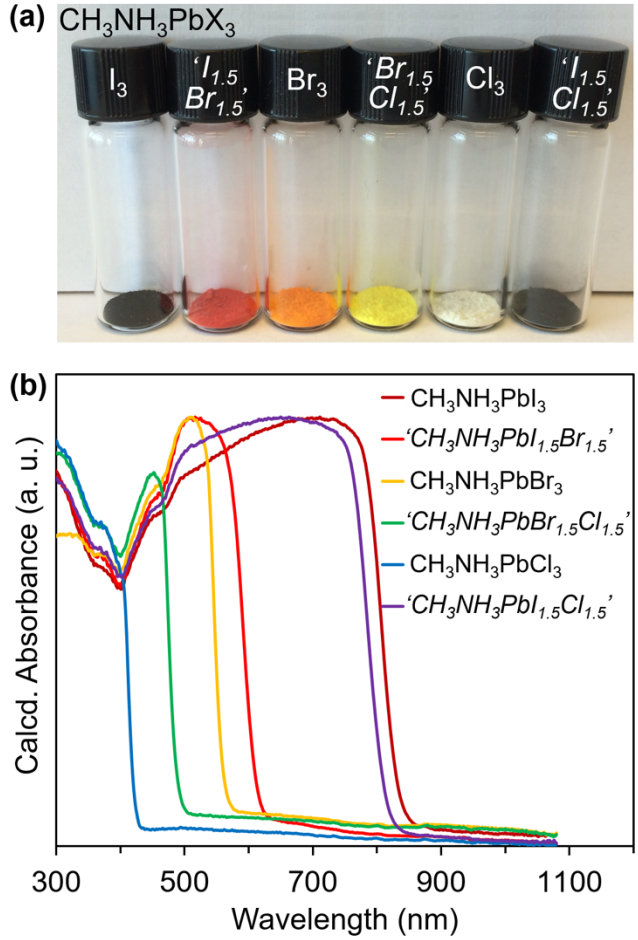

Figure 1. Representative visual image (a) and diffuse reflectance data (b) of solid organolead halide perovskites prepared by solution phase synthesis or thermal annealing (either method gives similar results). Italicized formulas in quotation marks are calculated from synthetic loading; formulas in regular script are compositional assignments made from all experimental data. The minimum at 400 nm in (b) is an instrumental artifact.

The powder X-ray diffraction (XRD) pattern of $CH_3NH_3PbI_3$ matches the tetragonal standard pattern of its most stable room temperature phase, while those of $CH_3NH_3PbBr_3$ and $CH_3NH_3PbCl_3$ match their cubic standard patterns (Figure 2a). Scanning electron microscopy (SEM) shows that samples are made of 0.3-2 μm particles (Figure 3). Iodo-bromide and bromo-chloride perovskites such as *'$CH_3NH_3PbI_{1.5}Br_{1.5}$'* and *'$CH_3NH_3PbBr_{1.5}Cl_{1.5}$'*, respectively, show single sets of XRD peaks that are intermediate between those of the parent, pure halide perovskites. Scherrer analysis of the relatively broad XRD peaks of *'$CH_3NH_3PbI_{1.5}Br_{1.5}$'* yields average single crystalline domain sizes of 36±12 nm. In contrast, iodo-chloride perovskites such as *'$CH_3NH_3PbI_{1.5}Cl_{1.5}$'* show two distinct sets of XRD peaks that clearly correspond to a physical mixture of phase-segregated $CH_3NH_3PbI_3$ and $CH_3NH_3PbCl_3$ (Figure 2a).

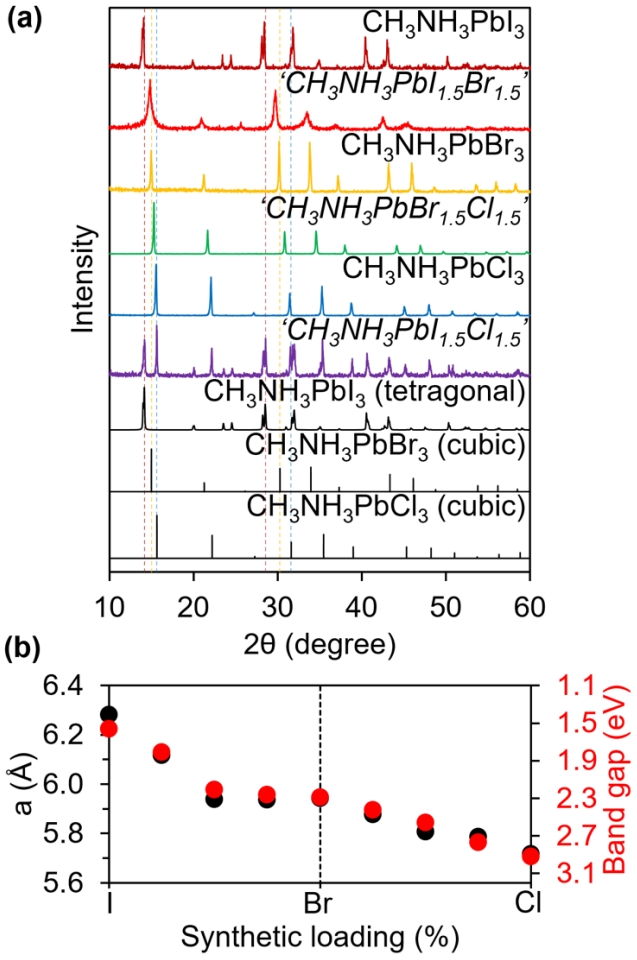

Figure 2. Powder XRD patterns (a), lattice parameter and absorption edge data (b) as a function of relative halide synthetic loading (%) for organolead halide perovskites prepared by solution phase synthesis. Italicized formulas in quotation marks are calculated from synthetic loading; formulas in regular script are compositional assignments made from all experimental data.

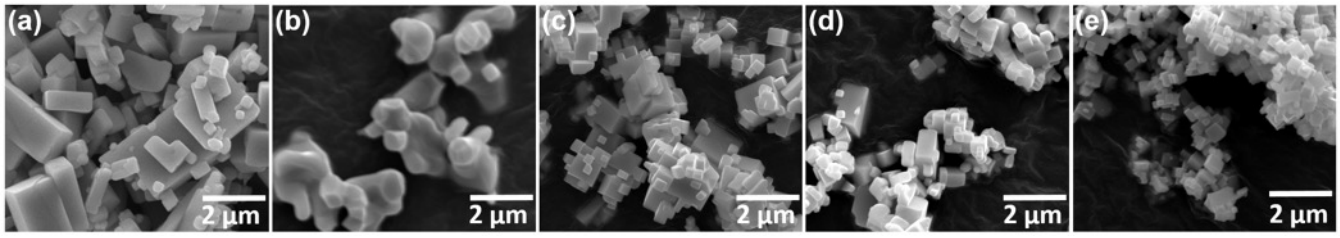

Figure 3. Representative SEM images of $CH_3NH_3PbI_3$ (a), $CH_3NH_3PbBr_3$ (c) and $CH_3NH_3PbCl_3$ (e) made by solution phase synthesis, and of *'$CH_3NH_3PbI_{1.5}Br_{1.5}$'* (b) and *'$CH_3NH_3PbBr_{1.5}Cl_{1.5}$'* (d) made by solid phase synthesis (see Methods).

As shown in Figure 2b, both the absorption edge and lattice parameter of mixed-halide perovskites show a non-linear dependence or "bowing" on the iodide to bromide ratio, but vary linearly when transitioning from bromide to chloride. In other words, the absorption edge and lattice parameter of *'$CH_3NH_3PbI_{3-a}Br_a$'* samples made with 0-50% bromide synthetic loading ($0 \leq a \leq 1.5$) are much closer to pure bromide than to iodide. In contrast, the lattice parameter and absorption edge of $CH_3NH_3PbBr_{1.5}Cl_{1.5}$ lie halfway between pure bromide and chloride.

The different behavior displayed by different mixed-halide systems can be explained in part by crystallography. According to both Hume-Rothery[72] and Vegard[73,74] rules, tetragonal $CH_3NH_3PbI_3$ and cubic $CH_3NH_3PbBr_3$ may only partially alloy because they do not share the same crystal structure even though their lattice mismatch is small (6.4%) and their halogens have similar electronegativities (χ_P = 3.16 for I *vs.* 2.96 for Br) (Table 1). Cubic $CH_3NH_3PbBr_3$ and cubic $CH_3NH_3PbCl_3$ are able to form solid solutions because they adopt the same crystal structure, have a small lattice mismatch (4.5%) and their halogens have similar electronegativities (χ_P = 2.96 for Br *vs.* 2.66 for Cl) (Table 1). $CH_3NH_3PbI_3$ and $CH_3NH_3PbCl_3$ cannot be expected to form solid solutions to any significant extent because they form different crystal structures with a large lattice mismatch (11%) and their halogens have very different electronegativities (χ_P = 3.16 for I *vs.* 2.66 for Cl) (Table 1). Unsurprisingly, annealed films of *'$CH_3NH_3PbI_{3-a}Cl_a$'* do not seem to contain chloride within the detection limit of energy-dispersive X-ray spectroscopy (EDS), implying that any incorporation of chloride in the crystal lattice (x) must be extremely low.[38-44]

Table 1. Selected data for $CH_3NH_3PbX_3$ perovskites.

X	Lattice parameters (Å)	Δa (%)[a]	$\bar{\chi}_P^X$
I	6.3115(a), 6.3161(c)[75]	6.4	3.16
Br	5.9345(a)[76]	0	2.96
Cl	5.6694(a)[77]	-4.5	2.66

[a] $\Delta a = 100 \times [(a_X - a_{Br}) / a_{Br}]$

^{207}Pb ssNMR of organolead halides. To gain more physical insight into alloying and phase segregation in organolead mixed-halide perovskites, we employed ^{207}Pb ssNMR spectroscopy. As shown in Figure 4, the ^{207}Pb ssNMR spectra of the single-halide perovskites show one relatively broad peak. The isotropic chemical shift (δ_{iso}) moves progressively upfield (to lower ppm value) as the halogen electronegativity and perovskite band gap increase (Figure 5). This linear correlation is similar to that observed in the lead dihalides (PbX_2, X = I, Br, Cl; Figures S1 and S2).[58,60,63–66] In contrast, the ^{207}Pb ssNMR spectra of mixed-halide perovskites made by solution phase synthesis exhibit multiple peaks (Figure 4). For example, the ^{207}Pb ssNMR spectra of mixed-halide perovskites made by solution phase synthesis with a 1:1 synthetic loading show two peaks each for *'$CH_3NH_3PbI_{1.5}Br_{1.5}$'* and *'$CH_3NH_3PbI_{1.5}Cl_{1.5}$'*, and three peaks for *'$CH_3NH_3PbBr_{1.5}Cl_{1.5}$'*.

In order to determine whether the presence of extra ^{207}Pb peaks is the result of higher order NMR interactions or compositional sample variations, we collected ^{207}Pb ssNMR spectra with and without sample spinning and at different magnetic fields. For example, the ^{207}Pb ssNMR spectra of the *'$CH_3NH_3PbBr_{1.5}Cl_{1.5}$'* sample collected with a 10 kHz magnetic angle spinning (MAS) frequency or with a stationary (static) sample spinning are virtually indistinguishable; both show three similar peaks at 160, -117 and -379 ppm (Figure S3). The presence of very broad ^{207}Pb NMR linewidths in all samples, in addition to the lack of narrowing from MAS (see S.I.), is consistent with the ^{207}Pb ssNMR spectra of other lead-containing semiconductors.[65,78,79] The full width at half maximum (fwhm) of the ^{207}Pb resonances is dependent on composition, going from *ca*. 253 ppm to 33 ppm between pure iodide and pure chloride perovskite, respectively.

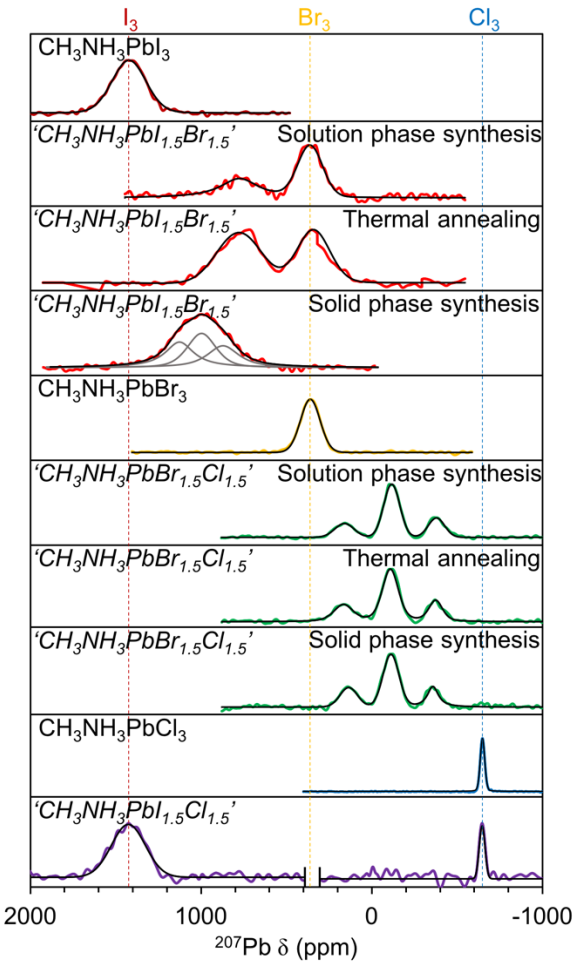

Figure 4. Static ^{207}Pb ssNMR spectra (22 °C) of representative organolead single- and mixed-halide perovskites prepared by solution phase synthesis, thermal annealing, and solid phase synthesis; black curves were fit to mixed Gaussian/Lorentzian peaks (see Methods). MAS lead to no substantial narrowing of the peaks (see S.I.). Italicized formulas in quotation marks are calculated from synthetic loading; formulas in regular script are compositional assignments made from all experimental data.

The ^{207}Pb ssNMR signal broadening in these systems is likely to be primarily due to homogeneous broadening. Additional control experiments using a lower magnetic field of 9.4 T (400 MHz) (as opposed to 16.4 T (600 MHz)) lead to similar ^{207}Pb ssNMR spectra. Superior resolution was observed at the higher field of 16.4 T (see S.I.), which indicates that the broadening of the ^{207}Pb ssNMR peaks is primarily homogeneous. This shows that chemical shift anisotropy (CSA) is unlikely to contribute to the observed broadening to a significant extent, because

broadening would also increase with applied field. Longitudinal (T_1) and transverse (T_2') ^{207}Pb relaxation time constants were also measured for the single-halides (Table S1). Static ^{207}Pb ssNMR saturation recovery experiments yielded relatively short ^{207}Pb T_1 relaxation times between 1.1 and 1.4 s for all of the single-halide perovskites. Application of MAS lead to a dramatic reduction in the ^{207}Pb T_1's for both $CH_3NH_3PbI_3$ ($T_1 \approx 83$ ms) and $CH_3NH_3PbBr_3$ ($T_1 \approx 104$ ms), consistent with a recently proposed MAS induced halogen polarization exchange longitudinal relaxation mechanism.[80] For $CH_3NH_3PbI_3$ and $CH_3NH_3PbBr_3$, T_2's were short (less than 90 μs) under both MAS and static sample conditions and were nearly equal to T_2*, which was calculated from the full width at half maximum of the ^{207}Pb ssNMR peaks. Relaxation measurements directly confirm that the broadening is primarily homogenous in nature. Both $CH_3NH_3PbI_3$ and $CH_3NH_3PbBr_3$ had much shorter transverse relaxation times than $CH_3NH_3PbCl_3$, which suggests that dipolar/scalar coupling to the halogen nuclei could be responsible for the short transverse relaxation time constants. In summary, these observations indicate that the multiple ^{207}Pb ssNMR peaks observed for the organolead mixed-halide perovskites arise from distinct chemical species or phases that are actually present in each sample, and that the broadening of the different ^{207}Pb peaks is primarily homogeneous in nature and does not arise from a distribution of isotropic chemical shifts or CSA.

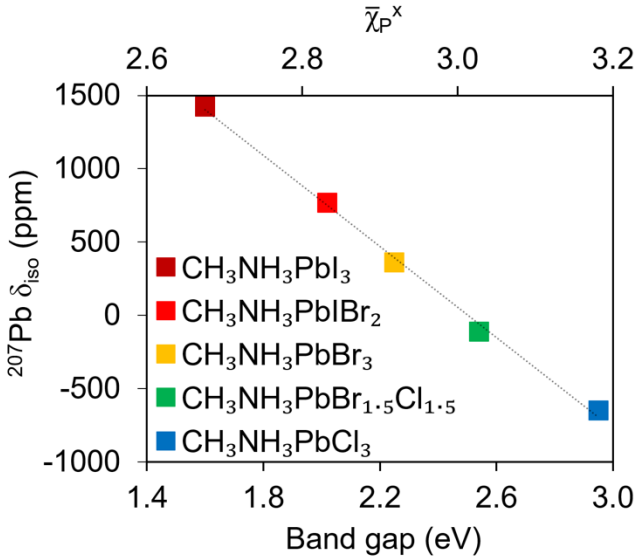

Figure 5. ^{207}Pb ssNMR isotropic chemical shifts (δ_{iso} at 22 °C) observed in single- and mixed-halide-organolead perovskites prepared by solution phase synthesis as a function of average halogen electronegativity and band gap. The chemical composition of mixed-halide perovskites was estimated from a calibration curve derived from ^{207}Pb δ_{iso} data of single-halide perovskites.

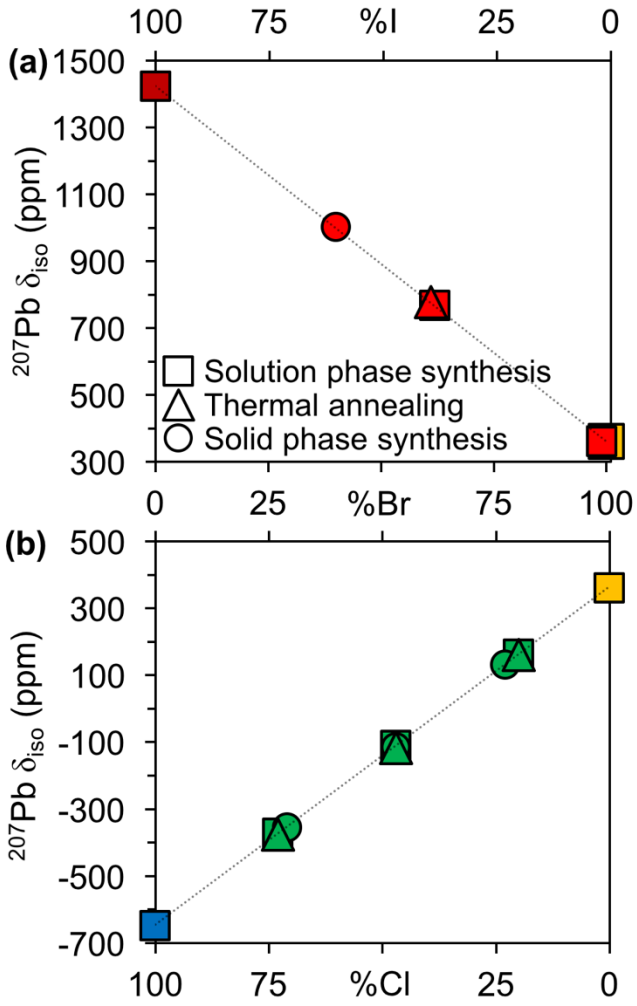

Figure 6. ^{207}Pb ssNMR isotropic chemical shifts (δ_{iso} at 22 °C) of single- and 1:1 mixed-halide-organolead perovskites prepared by solution phase synthesis, thermal annealing, and solid phase synthesis as a function of halide composition. The chemical composition of mixed-halide perovskites was estimated from a calibration curve derived from ^{207}Pb δ_{iso} data of single-halide perovskites.

Correlating structural and spectroscopic data. To explain our spectroscopic observations, we separately consider each of the aforementioned '1:1' mixed-halide perovskites. Because δ_{iso} varies linearly with average electronegativity and band gap (Figure 5), we used these values to estimate the chemical compositions of all observed ^{207}Pb resonances from a calibration curve determined from the single-halide perovskites (Figure 6). *'$CH_3NH_3PbI_{1.5}Br_{1.5}$'* prepared by solution phase synthesis has a single set of powder XRD peaks indicating a single crystalline phase is present (Figure 2a); however, this sample has two resolved ^{207}Pb ssNMR peaks located at 774

ppm and 361 ppm (Table 2 and Figure 4). The first NMR peak located at 774 ppm is in between the pure (single-halide) iodide and bromide perovskites, but closer to the latter (Figure 6a); based on its chemical shift, we attribute this resonance to the crystalline, bromide-rich perovskite $CH_3NH_3PbIBr_2$ (Table 2). This assignment is consistent with both the optical and XRD data for this sample (Figures 1b and 2a). The chemical shift of the second resonance at 361 ppm is identical to that of the pure bromide perovskite (Figures 4 and 6a). However, this phase is absent from XRD and steady state optical measurements, which leads us to propose two different, alternative assignments for it: (*i*) One possibility is the presence of amorphous $CH_3NH_3PbBr_3$ (Figure 7a); (*ii*) Another possibility is that the whole sample consists of core/shell nanocrystals made of $CH_3NH_3PbIBr_2$ cores surrounded by thin, semicrystalline $CH_3NH_3PbBr_3$ shells (Figure 7b). As in other similar nanostructures, thin $CH_3NH_3PbBr_3$ shells would be hard to distinguish by XRD because they would diffract weakly. In addition, in a core/shell configuration, the $CH_3NH_3PbBr_3$ lattice would likely expand to better epitaxially fit onto the iodide-containing $CH_3NH_3PbIBr_2$ core. A comparison of relative peak areas suggests that the ratio between the crystalline (C) $CH_3NH_3PbIBr_2$ and semicrystalline (A or /s) $CH_3NH_3PbBr_3$ phases present in this particular sample is 26% to 74% (Table 2).

A possible explanation for phase segregation during the solution phase synthesis of *'$CH_3NH_3PbI_{1.5}Br_{1.5}$'* is the loss of iodide precursors to the supernatant. ICP-MS and titration analyses of *'$CH_3NH_3PbI_{1.5}Br_{1.5}$'* samples made by this method suggest a somewhat variable and batch dependent bromide-rich composition with an I:Br between 28:72 and 19:81. ICP-MS analysis of two supernatants from two separate batches suggests that iodide is present at 2.7 wt% and 4.1 wt%, with no bromide detected in either sample. This is consistent with the presence of a recently calculated I-Br miscibility gap in this system below 70 °C.[46] Interestingly, ^{13}C cross-polarization MAS (CPMAS) ssNMR spectra of *'$CH_3NH_3PbI_{1.5}Br_{1.5}$'* samples made by solution phase synthesis show two well-resolved peaks. A ^{13}C detected proton T_1 measurement showed distinct proton T_1's for each of these peaks (see S.I.). This is consistent with macroscopic segregation of the two phases, since homogeneous mixing would lead to the observation of a single common T_1.

Table 2. ^{207}Pb ssNMR data and proposed compositional assignments for organolead halide perovskites.

Synthetic Loading[a]	δ_{iso} (ppm)	Compositional assignment(s)[b]	Phase[d] (%[c])
Solution phase synthesis			
'$CH_3NH_3PbI_3$'	1423	$CH_3NH_3PbI_3$	C (100)
'$CH_3NH_3PbI_{1.5}Br_{1.5}$'	774	$CH_3NH_3PbIBr_2$	C (26)
	361	$CH_3NH_3PbBr_3$	A or /s (74)[e]
'$CH_3NH_3PbBr_3$'	361	$CH_3NH_3PbBr_3$	C (100)
'$CH_3NH_3PbBr_{1.5}Cl_{1.5}$'	160	$CH_3NH_3PbBr_{2.25}Cl_{0.75}$	D (21)
	-117	$CH_3NH_3PbBr_{1.5}Cl_{1.5}$	C (56)
	-379	$CH_3NH_3PbBr_{0.75}Cl_{2.25}$	D (23)
'$CH_3NH_3PbCl_3$'	-648	$CH_3NH_3PbCl_3$	C (100)
'$CH_3NH_3PbI_{1.5}Cl_{1.5}$'	1427	$CH_3NH_3PbI_3$	C (n.d.)
	-647	$CH_3NH_3PbCl_3$	C (n.d.)
Thermal annealing[f]			
'$CH_3NH_3PbI_{1.5}Br_{1.5}$'	778	$CH_3NH_3PbIBr_2$	C (53)
	343	$CH_3NH_3PbBr_3$	A or /s (47)[e]
'$CH_3NH_3PbBr_{1.5}Cl_{1.5}$'	166	$CH_3NH_3PbBr_{2.25}Cl_{0.75}$	D (24)
	-109	$CH_3NH_3PbBr_{1.5}Cl_{1.5}$	C (55)
	-375	$CH_3NH_3PbBr_{0.75}Cl_{2.25}$	D (21)
Solid phase synthesis			
'$CH_3NH_3PbI_{1.5}Br_{1.5}$'	1126	$CH_3NH_3PbI_{2.1}Br_{0.9}$	D (30)
	997	$CH_3NH_3PbI_{1.8}Br_{1.2}$	C (40)
	872	$CH_3NH_3PbI_{1.5}Br_{1.5}$	D (30)
'$CH_3NH_3PbBr_{1.5}Cl_{1.5}$'	135	$CH_3NH_3PbBr_{2.25}Cl_{0.75}$	D (23)
	-112	$CH_3NH_3PbBr_{1.5}Cl_{1.5}$	C (62)
	-358	$CH_3NH_3PbBr_{0.75}Cl_{2.25}$	D (15)

[a]Hypothetical formulas calculated from synthetic loading alone. [b]Actual compositional assignments from all experimental data combined. [c]Crystalline (C), amorphous (A), core/shell (c/s), and dopant (D) phases. [d]NMR peak integrations (n.d. = not determined). [e]Not the same batch; subtle differences during solution phase synthesis result in slightly different % values. [f]To 200 °C (see Methods).

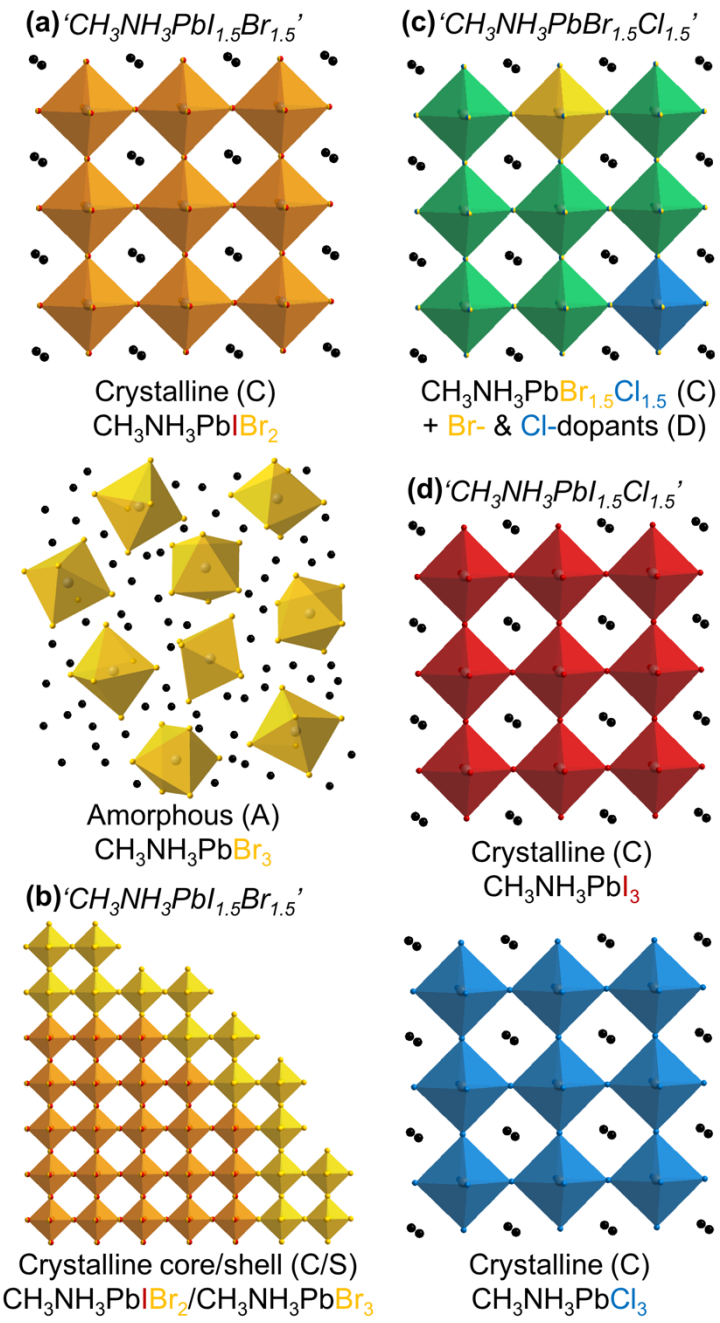

Figure 7. Cartoon illustrating possible compositional assignments for the mixed-halide perovskites *'$CH_3NH_3PbI_{1.5}Br_{1.5}$'* (a or b), *'$CH_3NH_3PbBr_{1.5}Cl_{1.5}$'* (c), and *'$CH_3NH_3PbI_{1.5}Cl_{1.5}$'* (d) made by solution phase synthesis and thermal annealing (see Methods). Colored octahedra represent $[PbX_6]^{4-}$ anions while black dots represent $CH_3NH_3^+$ cations. C = Crystalline, A = Amorphous, D = Dopants, c/s = core/shell. When *'$CH_3NH_3PbI_{1.5}Br_{1.5}$'* is made by solid phase synthesis, the crystalline phase is closer to stoichiometric and the semicrystalline bromide-rich (amorphous or shell) phase is not observed (see Table 2).

'$CH_3NH_3PbBr_{1.5}Cl_{1.5}$' made by solution phase synthesis also shows a single set of XRD peaks indicating the presence of a single, crystalline phase (Figure 2a). "Slow" XRD measurements between 29–40 degrees (2θ) showed no additional peaks (see S.I.). However, *'$CH_3NH_3PbBr_{1.5}Cl_{1.5}$'* shows three ^{207}Pb ssNMR peaks located at 160 ppm, -117 ppm, and -379 ppm in a *ca.* 1:2:1 ratio (Table 2 and Figure 4). The most intense, center resonance at -117 ppm is halfway between pure bromide and chloride perovskites (Figure 6b); based on its chemical shift, and in agreement with optical and XRD data, we attribute it to crystalline $CH_3NH_3PbBr_{1.5}Cl_{1.5}$ (Table 2). The other two side resonances are nearly equidistant from the center resonance; based on their relative chemical shifts, they could be assigned as $CH_3NH_3PbBr_{2.25}Cl_{0.75}$ (160 ppm), and $CH_3NH_3PbBr_{0.75}Cl_{2.25}$ (-379 ppm) (Table 2 and Figure 6b). These assignments correspond to individual lead coordination environments comprised of $[PbBr_5Cl]^{4-}$ or $[PbBr_4Cl_2]^{4-}$ octahedra and $[PbBrCl_5]^{4-}$ or $[PbBr_2Cl_4]^{4-}$ octahedra, respectively; because the ^{207}Pb ssNMR peaks are broad, we are unable to distinguish between each of these pairs of individual assignments. These nonstoichiometric bromide- and chloride-rich octahedra could be present as either amorphous, uncrystallized impurities or as dopant sites within the main $CH_3NH_3PbBr_{1.5}Cl_{1.5}$ crystalline phase; because of their very similar peak intensities relative to each other (160 ppm, 21%; -379 ppm, 23%), yet significantly smaller than that of the main crystalline phase (-117 ppm, 56%), we suspect that they exist as dopants (Figure 7c). Such isolated Br- and Cl-rich sites would not only be difficult to resolve by XRD, but variations in Pb-X bond lengths caused by lattice compression (for example, in $[PbBr_5Cl]^{4-}$) or elongation (for example, in $[PbBrCl_5]^{4-}$) could also shift the ^{207}Pb resonances farther upfield and downfield, respectively, from where they could be expected based on composition alone.[61,63,81] A possible explanation for these observations is spinodal decomposition of the stoichiometric Br-Cl perovskite, a well-known phenomenon where the main crystalline phase coexists in equilibrium with a definite amount of non-stoichiometric domains.[82-85]

Finally, *'$CH_3NH_3PbI_{1.5}Cl_{1.5}$'* displays two distinct, independent sets of XRD peaks along with two major ^{207}Pb ssNMR peaks, the latter located at 1427 ppm and -647 ppm (Figures 2a and 4); these data are consistent with phase segregated, crystalline $CH_3NH_3PbI_3$ and $CH_3NH_3PbCl_3$, respectively, as expected from simple crystallographic considerations (Table 2 and Figure 7d).

Thermal annealing experiments. A possible explanation for the presence of dopants and amorphous phases in organolead halide perovskites relates to their ability to crystallize under

specific synthetic conditions. The materials initially mentioned above were synthesized at room temperature by precipitation from solution (Scheme 1a). To probe this issue, we subjected freshly

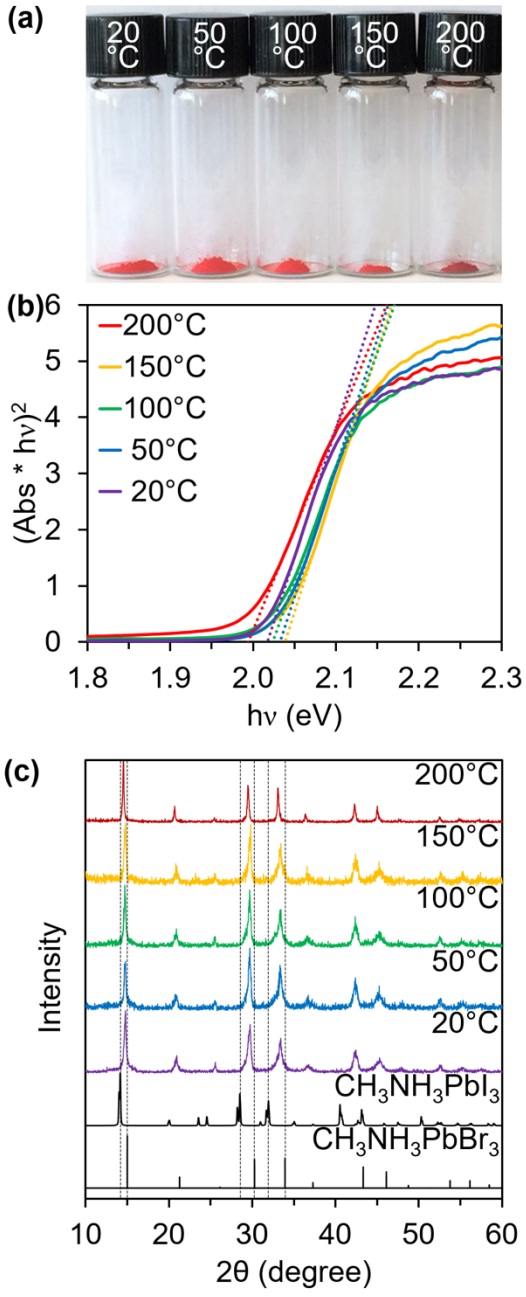

Figure 8. Visual image (a), tauc plot (b), and powder XRD patterns (c) for *'$CH_3NH_3PbI_{1.5}Br_{1.5}$'* made by solution phase synthesis as well as after thermal annealing at different temperatures (see Methods). Annealing at higher temperatures (≥ 250 °C) resulted in partial sample decomposition (see S.I.).

made mixed-halide perovskites to thermal annealing (see Methods for details). Neither *'$CH_3NH_3PbI_{1.5}Br_{1.5}$'* or *'$CH_3NH_3PbBr_{1.5}Cl_{1.5}$'* shows a significant change in color or crystal structure between 20 °C and 200 °C, above which both materials start showing signs of thermal decomposition (T_{dec} onset ≥ 250 °C)[45,86-89] (Figures 8, S7 and S8). In the case of *'$CH_3NH_3PbI_{1.5}Br_{1.5}$'*, the individual powder XRD peaks become sharper upon annealing (Figure 8), indicating an increase in single crystalline domain (Scherrer) size from 36±12 nm at 20 °C to 68±10 nm at 200 °C.

Critically, ^{207}Pb ssNMR reveals that the composition of the different phases present in organolead mixed-halide perovskites made by solution phase synthesis remains roughly the same after thermal annealing up to 200 °C. The *'$CH_3NH_3PbI_{1.5}Br_{1.5}$'* sample retains two resonances at 778 ppm and 343 ppm (Table 2 and Figure 4), strongly indicating that both crystalline $CH_3NH_3PbIBr_2$ and semicrystalline $CH_3NH_3PbBr_3$, respectively, survive and are still present after annealing (Table 2 and Figure 6a). Increased iodide incorporation during the initial solution phase synthesis of the *'$CH_3NH_3PbI_{1.5}Br_{1.5}$'* sample that was subjected to thermal annealing may explain the change in relative intensities between the 778 ppm and 343 ppm peaks. This idea is supported by the variable iodide wt% values measured by ICP-MS for different supernatants. Likewise, the *'$CH_3NH_3PbBr_{1.5}Cl_{1.5}$'* sample retains three resonances at 166 ppm, -109 ppm and -375 ppm with a 1:2:1 relative integration, which is almost identical to the sample before annealing (Figure 4 and Figure 6b). These data strongly support the idea that the nonstoichiometric $CH_3NH_3PbBr_{2.25}Cl_{0.75}$ (166 ppm) and $CH_3NH_3PbBr_{0.75}Cl_{2.25}$ (-375 ppm) dopants likely form by spinodal decomposition and are persistent alongside the main stoichiometric phase $CH_3NH_3PbBr_{1.5}Cl_{1.5}$ (-109 ppm) after annealing.

Solid phase synthesis. Having observed that semicrystalline, phase segregated phases and dopants can coexist and survive after thermal annealing, we questioned whether the persistence of such domains could be related to the ability of halide ions to diffuse from one solid phase to another. To probe this question, we sought to synthesize mixed-halide perovskites by a solid state synthesis that involves mixing pre-made, solid, single-halide perovskites and subjecting them to heat (Scheme 1b, see also Methods).

As shown in Figure 9a, an equimolar (1:1) solid mixture of $CH_3NH_3PbI_3$ and $CH_3NH_3PbBr_3$ changes color from brown-orange at 20 °C to black after heating to 200 °C. The absorption edges of the two starting materials, initially present at 20 °C, begin to move closer

together and coalesce upon heating; a single absorption edge located roughly halfway between the two parent, single-halide perovskites is observed after heating to 200 °C (Figure 9b and 10a). Similarly, the two initial sets of XRD peaks corresponding to the two parent, single-halide perovskites move closer together and coalesce into a single set of XRD peaks after heating from 20 °C to 200 °C (Figures 9c and 10a). Together, these data are consistent with the formation of *'$CH_3NH_3PbI_{1.5}Br_{1.5}$'* in the solid state.

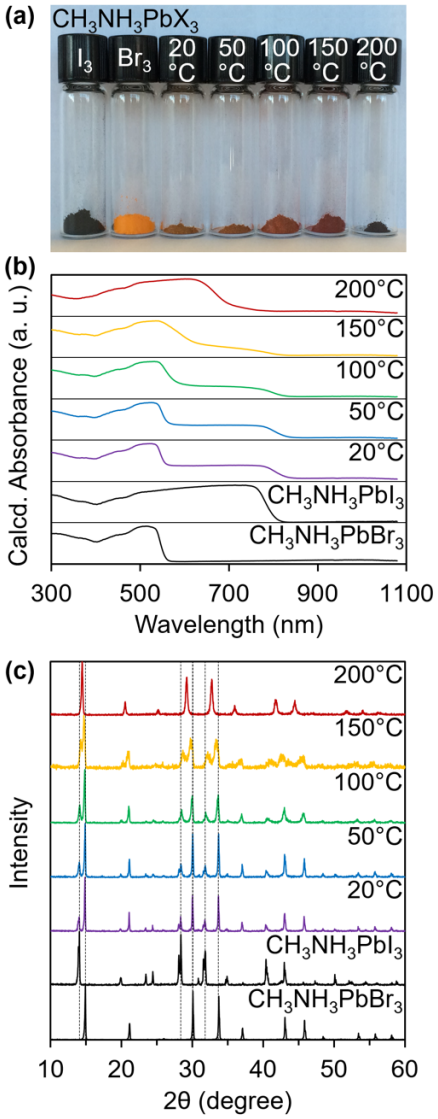

Figure 9. Visual image (a), diffuse reflectance (b), and powder XRD patterns (c) for *'$CH_3NH_3PbI_{1.5}Br_{1.5}$'* made by solid phase synthesis starting from an equimolar mixture of $CH_3NH_3PbI_3$ and $CH_3NH_3PbBr_3$ (see Methods). Heating at higher temperatures (≥ 250 °C) resulted in partial sample decomposition (see S.I.).

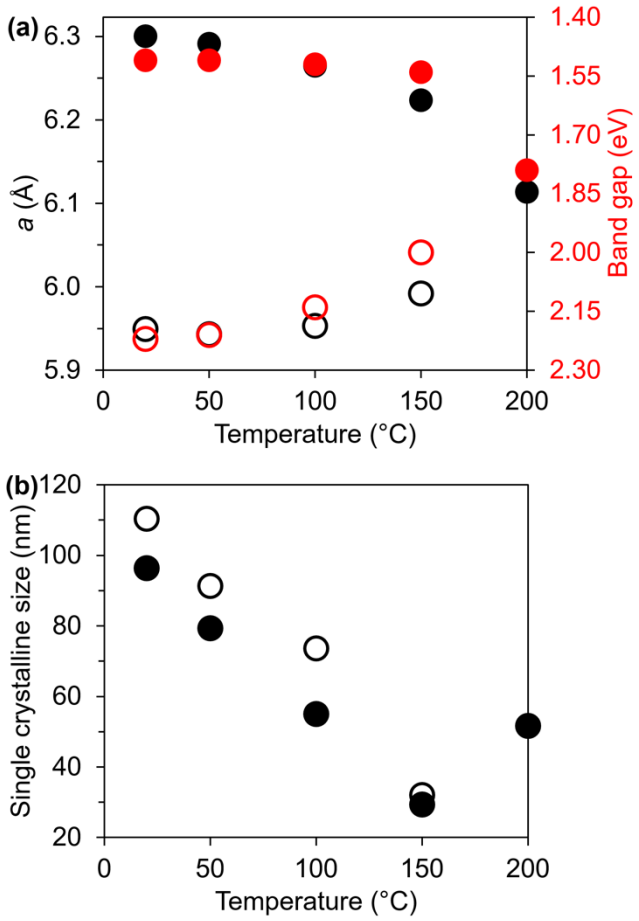

Figure 10. Effect of annealing temperature on the lattice parameter and band gap (a) and single crystalline (Scherrer) domain size (b) measured by XRD during the solid phase synthesis of *'$CH_3NH_3PbI_{1.5}Br_{1.5}$'* starting from a near equimolar mixture of $CH_3NH_3PbI_3$ (solid circles) and $CH_3NH_3PbBr_3$ (open circles) (see Methods).

A closer examination of XRD data during the solid phase synthesis of *'$CH_3NH_3PbI_{1.5}Br_{1.5}$'* reveals that heating from 20 °C to 150 °C causes an initial decrease in the average single crystalline domain (Scherrer) sizes of the iodide-rich phase from 96±19 nm to 29±9 nm and of the bromide-rich phase from 110±13 nm to 32±10 nm (Figure 10b, solid and open circles, respectively). At this point, there is an inflection point after the two sets of peaks merge; further heating from 150 °C to 200 °C causes a slight increase in Scherrer size of the mixed-halide phase to 52±9 nm (Figure 10b). We attribute these two distinct particle size regimes to interfacial nucleation (*via* halide diffusion/exchange) and growth (*via* coalescence) of the new mixed-halide phase.[90] A very similar behavior is observed by optical spectroscopy and powder XRD during the solid state synthesis of

'$CH_3NH_3PbBr_{1.5}Cl_{1.5}$' starting from an equimolar mixture of $CH_3NH_3PbBr_3$ and $CH_3NH_3PbCl_3$ solid. In this case, the inflection point between decreasing (nucleation) and increasing (growth) single average crystalline domain sizes is slightly lower than in the previous case, at *ca.* 100-150 °C (see S.I.). In both cases, simultaneous differential thermal–thermogravimetric analyses (DTA-TGA) showed that these solid phase reactions are accompanied by broad or 'shallow' endothermic transitions with no measurable mass loss (see S.I.). A comparison of XRD and scanning electron microscopy (SEM) data showed that the mixed-halide perovskites produced in this way consist of heavily twinned particles of comparable size and morphology to those of the parent, single-halide perovskites (Figure 3).

Critically, the ^{207}Pb ssNMR spectrum of *'$CH_3NH_3PbI_{1.5}Br_{1.5}$'* prepared by solid phase synthesis shows not two, but one single broad resonance at 997 ppm (Table 2 and Figure 4). Interestingly, this peak is significantly broader (fwhm = 410 ppm) than those of the parent $CH_3NH_3PbI_3$ and $CH_3NH_3PbBr_3$ perovskites (fwhm = 240 ppm and 35 ppm, respectively) (see Figure 4 and S.I.); this suggests that this peak is made of multiple overlapping resonances likely corresponding to a range of different local lead environments within a single phase. We hypothesize that these sites are non-stoichiometric I- and Br-rich dopants similar to those found in *'$CH_3NH_3PbBr_{1.5}Cl_{1.5}$'* (see above). Deconvolution of the broad resonance at 997 ppm into three peaks suggests that the *'$CH_3NH_3PbI_{1.5}Br_{1.5}$'* sample produced by solid phase synthesis is actually composed of $CH_3NH_3PbI_{2.1}Br_{0.9}$ (1126 ppm, 30%), $CH_3NH_3PbI_{1.8}Br_{1.2}$ (997 ppm, 40%), and $CH_3NH_3PbI_{1.5}Br_{1.5}$ (872 ppm, 30%) (Table 2 and Figure 4; see also S.I.). Experimental uncertainties associated with weighing equimolar amounts of starting materials may account for the $CH_3NH_3PbI_{1.8}Br_{1.2}$ crystalline product being slightly off the 1:1 halide ratio expected from loading alone.

Thus, in contrast to solution phase synthesis, no amorphous $CH_3NH_3PbBr_3$ is observed in *'$CH_3NH_3PbI_{1.5}Br_{1.5}$'* made by solid phase synthesis. This suggests that the specific synthetic procedure has a large impact on the composition and purity of the resulting mixed iodo-bromide organolead perovskites. In contrast to solution phase synthesis, which is carried out at 20 °C, our solid phase synthesis is carried at 200 °C, well above the maximum point of the miscibility dome proposed in the recently calculated I-Br phase diagram.[46] In addition, our solid phase synthesis requires no solvent(s) so that no single precursor or major component is lost during sample isolation and purification.

In contrast to *'$CH_3NH_3PbI_{1.5}Br_{1.5}$'*, the ^{207}Pb ssNMR spectrum of *'$CH_3NH_3PbBr_{1.5}Cl_{1.5}$'* prepared by solid phase synthesis still shows three ^{207}Pb ssNMR peaks that are very similar to those observed when the sample is prepared by either solution phase synthesis or thermal annealing methods (Figure 4). Based on the specific chemical shifts, we assign these resonances as $CH_3NH_3PbBr_{2.25}Cl_{0.75}$ (135 ppm, 23%), $CH_3NH_3PbBr_{1.5}Cl_{1.5}$ (-112 ppm, 62%), and $CH_3NH_3PbBr_{0.75}Cl_{2.25}$ (-358 ppm, 15%) (Table 2). Because three similar resonances are present in the ^{207}Pb ssNMR spectra of all the *'$CH_3NH_3PbBr_{1.5}Cl_{1.5}$'* samples studied, we conclude that the non-stoichiometric dopants form spontaneously (Figure 7c). These dopant sites or impurities are always naturally present and are persistent regardless of which specific synthetic method is used.

Conclusions

In summary, we used a combination of optical absorption spectroscopy, powder XRD and, for the first time, ^{207}Pb ssNMR spectroscopy to investigate phase segregation and alloying in organolead mixed-halide perovskites. While crystallography alone accounts for phase segregation between $CH_3NH_3PbI_3$ and $CH_3NH_3PbCl_3$, it does not explain the true microstructure and extent of alloying between $CH_3NH_3PbI_3$ and $CH_3NH_3PbBr_3$, or between $CH_3NH_3PbBr_3$ and $CH_3NH_3PbCl_3$.

Compositional assignment of multiple resonances observed in the ^{207}Pb ssNMR spectra of mixed-halide perovskites unveiled the presence of nonstoichiometric impurities or "dopants", as well as of semicrystalline (amorphous or nanostructured core/shell) phases, which accompany the main stoichiometric crystalline phase. Critically, dopants are prevalent and persistent regardless of whether solution phase synthesis, thermal annealing or solid phase synthesis is used to prepare these samples. In contrast, semicrystalline phases can form when samples are made by room temperature solution phase synthesis or their thermal annealing, but not by high temperature solid phase synthesis.

Our thermal annealing experiments showed that the presence of dopants and semicrystalline phases is not related to the ability of organolead mixed-halide perovskites to crystallize under specific synthetic conditions. Further, solid phase synthesis experiments showed that ion diffusion is not a barrier to alloying in organolead halide perovskites. The formation of nonstoichiometric dopants is consistent with partial phase segregation caused by spinodal decomposition, which results in small composition fluctuations throughout the entire lattice that differ from the desired stoichiometric phase. In other words, these materials are composed of a

main stoichiometric, alloyed phase that exists in equilibrium with two nonstoichiometric, halide-rich phases at room temperature.

Combined with other more commonly used optical absorption spectroscopy and X-ray diffraction methods, ^{207}Pb ssNMR offers unique opportunities to understand how various synthetic procedures affect the true composition, speciation, stability (against moisture, heat, light), and optoelectronic properties of these materials. Further enhancements in the efficiency and performance of perovskite-based photovoltaics and other energy conversion devices may thus be achieved through careful synthetic manipulation of such impurity phases and nanodomains.

Methods

Materials. Lead(II) iodide (99%) and lead(II) bromide (98+%) were purchased from Acros; lead(II) chloride (99.999%) and methylamine solution (33 wt% in ethanol) from Sigma; hydroiodic acid (ACS, 55-58%), hydrobromic acid (ACS, 47.0-49.0%), hydrochloric acid (ACS, 37.2%), N,N-dimethylformamide (99.9%), and toluene (99.9%) from Fisher; acetonitrile (HPLC Grade, 99.8%) from EMD Millipore. All chemicals were used as received.

Synthesis. Methylammonium halides were prepared by a modified literature procedure.[91] Briefly, Hydroiodic acid (10 mL, 0.075 mol) or hydrobromic acid (8.6 mL, 0.075 mol) or hydrochloric acid (6.2 mL, 0.075 mol) was added to a solution of excess methylamine (24 mL, 0.192 mol) in ethanol (100 mL) at 0 °C, and the mixture stirred for 2 h. The mixture was concentrated and dried under vacuum at 60 °C for 12 h, and recrystallized from ethanol. *Solution phase synthesis.* $CH_3NH_3PbI_3$ was synthesized by dissolving PbI_2 (0.08 mmol) and CH_3NH_3I (0.24 mmol) in acetonitrile (20 mL), followed by precipitation *via* the addition of excess toluene. $CH_3NH_3PbBr_3$ and $CH_3NH_3PbCl_3$ were synthesized by dissolving $PbBr_2$ (0.2 mmol) and CH_3NH_3Br (0.2 mmol) or $PbCl_2$ (0.2 mmol) and CH_3NH_3Cl (0.2 mmol) in DMF (5 mL) followed by precipitation *via* the addition of excess toluene. *'$CH_3NH_3PbBr_{1.5}Cl_{1.5}$'* was synthesized using the same procedure as $CH_3NH_3PbBr_3$ and $CH_3NH_3PbCl_3$, using 0.1 mmol of each of the four solid precursors. *'$CH_3NH_3PbI_{1.5}Br_{1.5}$'* was synthesized by dissolving PbI_2 (0.072 mmol), CH_3NH_3I (0.216 mmol), $PbBr_2$ (0.072 mmol), and CH_3NH_3Br (0.216 mmol) in a mixture of acetonitrile (20 mL) and DMF (200 μL), followed by precipitation *via* the addition of excess toluene. *'$CH_3NH_3PbI_{1.5}Cl_{1.5}$'* was synthesized by dissolving PbI_2 (0.108 mmol), CH_3NH_3I (0.108 mmol), $PbCl_2$ (0.108 mmol), and CH_3NH_3Cl (0.108 mmol) in DMF (3 mL). The mixture was concentrated

and dried under vacuum, and the resulting solid could be annealed at 100°C for 1 h. *Thermal annealing*. Mixed-halide perovskites prepared by solution phase synthesis were subjected to annealing between 50-250 °C in 50 °C increments for 1 h each. *Solid phase synthesis*. A stoichiometrically desired mixture of the parent, single-halide perovskites was subjected to heating between 50°-200°C with 50°C increments for 1 hour each.

Optical characterization. *Diffuse reflectance* spectra of solid films were measured with a SL1 Tungsten Halogen lamp (vis-IR), a SL3 Deuterium Lamp (UV), and a BLACK-Comet C-SR-100 spectrometer. Samples were prepared by drop-casting toluene solutions onto glass slides. *Band gap values* were estimated by extrapolating the linear slope of tauc plots for direct band gap semiconductors ((absorbance $\times$ excitation energy in eV)^2 over excitation energy in eV).[92]

Structural characterization. *Powder X-ray diffraction* (XRD) was measured using Cu Kα radiation on a Rigaku Ultima IV (40 kV, 44 mA) using a "background-less" quartz sample holder. Scherrer analysis was performed using a κ value of 0.9. *Simultaneous differential thermal analysis – thermogravimetric analysis* (DTA-TGA) measurements were collected using a TA Instruments SDT 2960. After purging with N_2 gas, 15 mg per sample was subjected to two heating-cooling cycles at 20°C/min up to 200 °C, followed by cooling to 60 °C with a fan. *Scanning electron microscopy* (SEM) was performed with an FEI Quanta 250 field emission SEM at 10-11.5 kV. Samples were prepared by deposition onto an SEM slide with carbon tape, followed by coating with 5 nm of iridium.

Elemental analysis. ICP-MS data of were collected on a Thermo Scientific Element 1 ICP-MS instrument Elemental Scientific, Inc. PFA-100 low-flow nebulizer. 10-15 mg sample was dissolved in 70% nitric acid and then diluted to approximately 5 ppm with a 1% nitric acid in deionized water solution. Titration data were collected by Galbraith Laboratories, Inc.

^{207}Pb ssNMR. ^{207}Pb solid state (ss) NMR spectra were measured on a Bruker widebore 14.1 T (600 MHz) NMR spectrometer equipped with an AVANCE-II console. All spectra were acquired using a 4 mm magic-angle spinning (MAS) probe in double resonance mode. Samples were packed into 4 mm Kel-F rotor inserts, which were then inserted into a 4 mm zirconia rotor. The rotor inserts were used to prevent contamination and for center packing, ensuring very little sample would be outside of the radiofrequency coil. The ^{207}Pb resonant frequency was 125.55 MHz, with the carrier frequency adjusted depending on the varying ^{207}Pb chemical shifts of each sample. $Pb(NO_3)_2$ (δ = -3490 ppm, 22 °C) was used as an external calibration standard. The

DEPTH pulse sequence[93] (Bruker's standard "zgbs" pulse sequence) was used to obtain both static and MAS ^{207}Pb spectra; this pulse sequence consists of an initial 90° pulse, followed by two 180° pulses spaced by a 2 μs delay (see S.I.). This pulse sequence eliminates very broad probe background ^{207}Pb NMR signals, which are likely due to lead in the probe's soldering and electronics. A 90° pulse length of 3.5 μs was used, with pulse power levels calibrated on $Pb(NO_3)_2$. Spectra were acquired with a 2.1 ms acquisition time and a 10 s recycle delay after each scan. Measurements of ^{207}Pb longitudinal relaxation times (T_1) for the pure halide phases under static conditions showed that the ^{207}Pb T_1 was less than 1.4 s in all samples (see Table S1). Therefore, the recycle delay of 10 s should provide quantitative signal intensities. This is consistent with the short ^{207}Pb T_1's reported in other lead-containing semiconductors.[65,78,79] Static and 10 kHz spectra were collected over a period of 1-6 days per sample. The number of scans used for each spectrum is listed in the Supporting Information, and generally varied between 1.5-40k. To confirm that the observed ^{207}Pb NMR spectral broadening was primarily homogeneous, selected spectra were also acquired at a lower magnetic field of 9.4 T under both static and MAS conditions. The 9.4 T experiments were performed on a Bruker widebore 400 MHz solid state NMR spectrometer equipped with an AVANCE III HD console. A 4 mm HXY triple resonance probe configured in a double resonance ^{1}H-^{207}Pb mode was used for experiments on the mixed-halide perovskites *'$CH_3NH_3PbI_{1.5}Br_{1.5}$'* and *'$CH_3NH_3PbBr_{1.5}Cl_{1.5}$'*. 4.95 μs ^{207}Pb 90° pulse widths were used. A 1.3 mm double resonance broadband probe was used for acquisition of ^{207}Pb ssNMR spectra of the pure halide perovskites at 9.4 T. MAS ^{207}Pb ssNMR spectra were acquired with an MAS frequency of 50 kHz and a rotor synchronized spin echo that had a 40 μs total duration composed of two rotor periods. 1.41 μs 90° and 2.81 μs 180° pulses were used. ^{13}C CPMAS ssNMR experiments were performed on *'$CH_3NH_3PbI_{1.5}Br_{1.5}$'* (see S.I.) with a 2.5 mm triple resonance HXY probe. ^{13}C detected proton $\underline{T}_1$ measurements were performed by applying a train of saturating π/2 pulses on ^{1}H, followed by a variable delay, then CP transfer to ^{13}C for detection. All ^{207}Pb NMR spectra were fit to simple mixed Gaussian/Lorentzian peaks using the solid lineshape analysis (SOLA) module v2.2.4 included in the Bruker TopSpin v3.0 software (see S.I.).

Acknowledgement

This research is supported by the U.S. Department of Energy, Office of Basic Energy Sciences, Division of Chemical Sciences, Geosciences, and Biosciences through the Ames

Laboratory. The Ames Laboratory is operated for the U.S. Department of Energy by Iowa State University under Contract No. DE-AC02-07CH11358. We thank K.-J. Galayda and R. S. Houk at Ames Laboratory for ICP-MS assistance. A. J. R. thanks the Ames Laboratory Royalty Account and Iowa State University for funding.

References

(1) Saliba, M.; Matsui, T.; Seo, J.-Y.; Domanski, K.; Correa-Baena, J.-P.; Nazeeruddin, M. K.; Zakeeruddin, S. M.; Tress, W.; Abate, A.; Hagfeldt, A.; Grätzel, M. Cesium-Containing Triple Cation Perovskite Solar Cells: Improved Stability, Reproducibility and High Efficiency. *Energy Environ. Sci.* **2016**, DOI: 10.1039/c5ee03874j.

(2) National Renewable Energy Laboratory. Best Research-Cell Efficiencies Chart. (Accessed on July 20, 2016). http://www.nrel.gov/ncpv/images/efficiency_chart.jpg.

(3) Marinova, N.; Tress, W.; Humphry-Baker, R.; Dar, M. I.; Bojinov, V.; Zakeeruddin, S. M.; Nazeeruddin, M. K.; Grätzel, M. Light Harvesting and Charge Recombination in $CH_3NH_3PbI_3$ Perovskite Solar Cells Studied by Hole Transport Layer Thickness Variation. *ACS Nano* **2015**, *9*, 4, 4200–4209.

(4) Kepenekian, M.; Robles, R.; Katan, C.; Sapori, D.; Pedesseau, L.; Even, J. Rashba and Dresselhaus Effects in Hybrid Organic-Inorganic Perovskites: From Basics to Devices. *ACS Nano* **2015**, *9*, 12, 11557–11567.

(5) Stranks, S. D.; Snaith, H. J. Metal-Halide Perovskites for Photovoltaic and Light-Emitting Devices. *Nature Nanotech.* **2015**, *10*, 391–402.

(6) Sum, T. C.; Mathews, N.; Xing, G.; Lim, S. S.; Chong, W. K.; Giovanni, D.; Dewi, H. A. Spectral Features and Charge Dynamics of Lead Halide Perovskites: Origins and Interpretations. *Acc. Chem. Res.* **2016**, *49*, 294–302.

(7) Hsiao, Y.-C.; Wu, T.; Li, M.; Liu, Q.; Qin, W.; Hu, B. Fundamental Physics Behind High-Efficiency Organo-Metal Halide Perovskite Solar Cells. *J. Mater. Chem. A* **2015**, *3*, 15372–15385.

(8) Sum, T. C.; Mathews, N. Advancements in Perovskite Solar Cells: Photophysics Behind the Photovoltaics. *Energy Environ. Sci.* **2014**, *7*, 2518–2534.

(9) Yin, W.-J.; Yang, J.-H.; Kang, J.; Yan, Y.; Wei, S.-H. Halide Perovskite Materials for Solar Cells: A Theoretical Review. *J. Mater. Chem. A* **2015**, *3*, 8926–8942.

(10) Green, M. A.; Ho-Baillie, A.; Snaith, H. J. The Emergence of Perovskite Solar Cells. *Nature Photon.* **2014**, *8*, 506–514.

(11) Gao, P.; Grätzel, M.; Nazeeruddin, M. Organohalide Lead Perovskites for Photovoltaic Applications. *Energy Environ. Sci.* **2014**, *7*, 2448–2463.

(12) Kazim, S.; Nazeeruddin, S. K.; Grätzel, M.; Ahmad, S. Perovskite as Light Harvester: A Game Changer in Photovoltaics. *Angew. Chem. Int. Ed.* **2014**, *53*, 2812–2824.

(13) Park, N. G. Organometal Perovskite Light Absorbers Toward a 20% Efficiency Low-Cost Solid-State Mesoscopic Solar Cell. *J. Phys. Chem. Lett.* **2013**, *4*, 2423–2429.

(14) Song, T. B.; Chen, Q.; Zhou, H.; Jiang, C.; Wang, H. H.; Yang, Y.; Liu, Y.; You, J.; Yang, Y. Perovskite Solar Cells: Film Formation and Properties. *J. Mater. Chem. A* **2015**, *3*, 9023–9050.

(15) Snaith, H. J. Perovskites: The Emergence of a New Era for Low-Cost, High-Efficiency Solar Cells. *J. Phys. Chem. Lett.* **2013**, *4*, 3623–3630.

(16) Zhu, F.; Men, L; Guo, Y.; Zhu, Q.; Bhattacharjee, U.; Goodwin, P. M.; Petrich, J. W.; Smith, E. A.; Vela, J. Shape Evolution and Single Particle Luminescence of Organometal Halide Perovskite Nanocrystals. *ACS Nano* **2015**, *9*, 2948–2959.

(17) Bade, S. G. R.; Li, J.; Ling, Y.; Tian, Y.; Dilbeck, T.; Besara, T.; Geske, T.; Gao, H.; Ma, B.; Hanson, K.; Siegrist, T.; Xu, C.; Yu, Z. Fully Printed Halide Perovskite Light-Emitting Diodes with Silver Nanowire Electrodes. *ACS Nano* **2016**, *10*, 1795–1801.

(18) Noh, J. H.; Im, S. H.; Heo, J. H.; Mandal, T. N.; Seok, S. I. Chemical Management for Colorful, Efficient, and Stable Inorganic-Organic Hybrid Nanostructured Solar Cells. *Nano Lett.* **2013**, *13*, 1764–1769.

(19) Sadhanala, A.; Deschler, F.; Thomas, T. H.; Dutton, S. E.; Goedel, K. C.; Hanusch, F. C.; Lai, M. L.; Steiner, U.; Bein, T.; Docampo, P.; Cahen, D.; Friend, R. H. Preparation of Single-Phase Films of $CH_3NH_3Pb(I_{1-x}Br_x)_3$ with Sharp Optical Band Edges. *J. Phys. Chem. Lett.* **2014**, *5*, 2501–2505.

(20) Davies, M. L.; Carnie, M.; Holliman, P. J.; Connell, A.; Douglas, P.; Watson, T.; Charbonneau, C.; Troughton, J.; Worsley, D. Compositions, Colours and Efficiencies of Organic-Inorganic Lead Iodide/Bromide Perovskites for Solar Cells. *Mater. Res. Innov.* **2014**, *18*, *7*, 482–485.

(21) Kitazawa, N.; Watanabe, Y.; Nakamura, Y. Optical Properties of $CH_3NH_3PbX_3$ (X = halogen) and their Mixed-Halide Crystals. *J. Mater. Sci.* **2002**, *37*, 3585–3587.

(22) Zhang, M.; Yu, H.; Lyu, M.; Wang, Q.; Yun, J. H.; Wang, L. Composition-Dependent Photoluminescence Intensity and Prolonged Recombination Lifetime of Perovskite $CH_3NH_3PbBr_{3-x}Cl_x$ Films. *Chem. Commun.* **2014**, *50*, 11727–11730.

(23) Protesescu, L.; Yakunin, S.; Bodnarchuk, M. I.; Krieg, F.; Caputo, R.; Hendon, C. H.; Yang, R. X.; Walsh, A.; Kovalenko, M. V. Nanocrystals of Cesium Lead Halide Perovskites ($CsPbX_3$, X = Cl, Br, and I): Novel Optoelectronic Materials Showing Bright Emission with Wide Color Gamut. *Nano Lett.* **2015**, *15*, 3692–3696.

(24) Sutter-Fella, C. M.; Li, Y.; Amani, M.; Ager, J. W. III; Toma, F. M.; Yablonovitch, E.; Sharp, I. D.; Javey, A. High Photoluminescence Quantum Yield in Band Gap Tunable Bromide Containing Mixed Halide Perovskites. *Nano Lett.* **2016**, *16*, 800–806.

(25) Gil-Escrig, L.; Miquel-Sempere, A.; Sessolo, M.; Bolink, H. J. Mixed Iodide-Bromide Methylammonium Lead Perovskite-Based Diodes for Light Emission and Photovoltaics. *J. Phys. Chem. Lett.* **2015**, *6*, 3743–3748.

(26) Zhu, W.; Bao, C.; Li, F.; Zhou, X.; Yang, J.; Yu, T.; Zou, Z. An Efficient Planar-Heterojunction Solar Cell Based on Wide-Bandgap $CH_3NH_3PbI_{2.1}Br_{0.9}$ Perovskite Film for Tandem Cell Applications. *Chem. Commun.* **2016**, *52*, 304–307.

(27) Zhou, Y.; Yang, M.; Game, O. S.; Wu, W.; Kwun, J.; Strauss, M. A.; Yan, Y.; Huang, J.; Padture, N. P. Manipulating Crystallization of Organolead Mixed-Halide Thin Films in Antisolvent Baths for Wide-Bandgap Perovskite Solar Cells. *ACS Appl. Mater. Interfaces* **2016**, *8*, 2232–2237.

(28) Kulkarni, S. A.; Baikie, T.; Boix, P. P.; Yantara, N.; Mathews, N.; Mhaisalkar, S. Band-Gap Tuning of Lead Halide Perovskites Using a Sequentional Deposition Process. *J. Mater. Chem. A* **2014**, *2*, 9221–9225.

(29) Hoke, E. T.; Slotcavage, D. J.; Dohner, E. R.; Bowring, A. R.; Karunadasa, H. I.; McGehee, M. D. Reversible Photo-Induced Trap Formation in Mixed-Halide Perovskites for Photovoltaics. *Chem. Sci.* **2015**, *6*, 613–617.

(30) Fedeli, P.; Gazza, F.; Calestani, D.; Ferro, P.; Besagni, T.; Zappettini, A.; Calestani, G.; Marchi, E.; Ceroni, P.; Mosca, R. Influence of the Synthetic Procedures on the Structural and Optical Properties of Mixed-Halide (Br, I) Perovskite Films. *J. Phys. Chem. C* **2015**, *119*, 21304–21313.

(31) Sadhanala, A.; Ahmad, S.; Zhao, B.; Giesbrecht, N.; Pearce, P. M.; Deschler, F.; Hoye, R. L. Z.; Gödel, K. C.; Bein, T.; Docampo, P.; Dutton, S. E.; De Volder, M. F. L.; Friend, R. H. Blue-Green Color Tunable Solution Processable Organolead Chloride-Bromide Mixed Halide Perovskites for Optoelectronic Applications. *Nano Lett.* **2015**, *15*, 6095–6101.

(32) Wei, M.; Chung, Y.-H.; Ziao, Y.; Chen, Z. Color Tunable Halide Perovskite $CH_3NH_3PbBr_{3-x}Cl_x$ Emission Via Annealing. *Org. Electron.* **2015**, *26*, 260–264.

(33) Zhang, T.; Yang, M.; Benson, E. E.; Li, Z.; van de Lagemaat, J.; Luther, J. M.; Yan, Y.; Zhu, K.; Zhao, Y. A Facile Solvothermal Growth of Single Crystal Mixed Halide Perovskite $CH_3NH_3Pb(Br_{1-x}Cl_x)_3$. *Chem. Commun.* **2015**, *51*, 7820–7823.

(34) Suarez, B.; Gonzalez-Pedro, V.; Ripolles, T. S.; Sanchez, R. S.; Otero, L.; Mora-Sero, I. Recombination Study of Combined Halides (Cl, Br, I) Perovskite Solar Cells. *J. Phys. Chem. Lett.* **2014**, *5*, 1628–1635.

(35) Yin, W. J.; Yan, Y.; Wei, S. H. Anomalous Alloy Properties in Mixed Halide Perovskites. *J. Phys. Chem. Lett.* **2014**, *5*, 3625–3631.

(36) Kim, J.; Lee, S.-H.; Chung, C.-H.; Hong, K.-H. Systematic Analysis of the Unique Band Gap Modulation of Mixed Halide Perovskites. *Phys. Chem. Chem. Phys.* **2016**, *18*, 4423–4428.

(37) Madjet, M. E.-A.; Akimov, A. V.; El-Mellouhi, F.; Berdiyorov, G. R.; Ashhab, S.; Tabet, N.; Kais, S. Enhancing the Carrier Thermalization Time in Organometallic Perovskites by Halide Mixing. *Phys. Chem. Chem. Phys.* **2016**, *18*, 5219–5231.

(38) Chae, J.; Dong, Q.; Huang, J.; Centrone, A. Chloride Incorporation Process in $CH_3NH_3PbI_{3-x}Cl_x$ Perovskites Via Nanoscale Bandgap Maps. *Nano Lett.* **2015**, *15*, 8114–8121.

(39) Xie, F. X.; Zhang, D.; Su, H.; Ren, X.; Wong, K. S.; Grätzel, M.; Choy, W. C. H. Vacuum-Assisted Thermal Annealing of $CH_3NH_3PbI_3$ for Highly Stable and Efficient Perovskite Solar Cells. *ACS Nano* **2015**, *9*, 1, 639–646.

(40) Williams, S. T.; Zuo, F.; Chueh, C. C.; Liao, C. Y.; Liang, P. W.; Jen, A. K. Y. Role of Chloride in the Morphological Evolution of Organo-Lead Halide Perovskite Thin Films. *ACS Nano* **2014**, *8*, 10, 10640–10654.

(41) Tidhar, Y.; Edri, E.; Weissman, H.; Zohar, D.; Hodes, G.; Cahen, D.; Rybtchinski, B.; Kirmayer, S. Crystallization of Methyl Ammonium Lead Halide Perovskites: Implications for Photovoltaic Applications. *J. Am. Chem. Soc.* **2014**, *136*, 13249–13256.

(42) Edri, E.; Kirmayer, S.; Mukhopadhyay, S.; Gartsman, K.; Hodes, G.; Cahen, D. Elucidating the Charge Carrier Separation and Working Mechanism of $CH_3NH_3PbI_{3-x}Cl_x$ Perovskite Solar Cells. *Nat. Commun.* **2014**, *5*, 1–8, DOI: 10.1038/ncomms4461.

(43) Zhao, Y.; Zhu, K.; CH_3NH_3Cl-Assisted One-Step Solution Growth of $CH_3NH_3PbI_3$: Stucture, Charge-Carrier Dynamics, and Photovoltaic Properties of Perovskite Solar Cells. *J. Phys. Chem. C* **2014**, *118*, 9412–9418.

(44) Colella, S.; Mosconi, E.; Fedeli, P.; Listorti, A.; Gazza, F.; Orlandi, F.; Ferro, P.; Besagni, T.; Rizzo, A.; Calestani, G.; Gigli, G.; De Angelis, F.; Mosca, R. $MAPbI_{3-x}Cl_x$ Mixed Halide Perovskite for Hybrid Solar Cells: The Role of Chloride as Dopant on the Transport and Structural Properties. *Chem. Mater.* **2013**, *25*, 4613–4618.

(45) Yang, B.; Keum, J.; Ovchinnikova, O. S.; Belianinov, A.; Chen, S.; Du, M.-H.; Ivanov, I. N.; Rouleau, C. M.; Geohegan, D. B.; Xiao, K. Deciphering Halogen Competition in Organometallic Halide Perovskite Growth. *J. Am. Chem. Soc.* **2016**, *138*, 5028–5035.

(46) Brivio, F.; Caetano, C.; Walsh, A. Thermodynamic Origin of Photoinstability in the $CH_3NH_3Pb(I_{1-x}Br_x)_3$ Hybrid Halide Perovskite Alloy. *J. Phys. Chem. Lett.* **2016**, *7*, 1083–1087.

(47) Hoke, E. T.; Slotcavage, D. J.; Dohner, E. R.; Bowring, A. R.; Karunadasa, H. I.; McGehee, M. D. Reversible Photo-Induced Trap Formation in Mixed-Halide Perovskites for Photovoltaics. *Chem. Sci.* **2015**, *6*, 613–617.

(48) Niemann, R. G.; Kontos, A. G.; Palles, D.; Kamitsos, E. I.; Kaltzoglou, A.; Brivio, F.; Falaras, P.; Cameron, P. J. Halogen Effects on Ordering and Bonding of $CH_3NH_3^+$ in $CH_3NH_3PbX_3$ (X = Cl, Br, I) Hybrid Perovskites: A Vibrational Spectroscopic Study. *J. Phys. Chem. C* **2016**, *120*, 2509–2519.

(49) Guerrero, A.; You, J.; Aranda, C.; Kang, Y. S.; Garcia-Belmonte, G.; Zhou, H.; Bisquert, J.; Yang, Y. Interfacial Degradation of Planar Lead Halide Perovskite Solar Cells. *ACS Nano* **2016**, *10*, 218–224.

(50) Jang, D. M.; Park, K.; Kim, D. H.; Park, J.; Shojaei, F.; Kang, H. S.; Ahn, J.-P.; Lee, J. W.; Song, J. K. Reversible Halide Exchange Reaction of Organometal Trihalide Perovskite Colloidal Nanocrystals for Full-Range Band Gap Tuning. *Nano Lett.* **2015***, 15*, 5191–5199.

(51) Pellet, N.; Teuscher, J.; Maier, J.; Grätzel, M. Transforming Hybrid Organic Inorganic Perovskites by Rapid Halide Exchange. Chem. Mater. **2015**, *27*, 2181–2188.

(52) Wong, A. B.; Lai, M.; Eaton, S. W.; Yu, Y.; Lin, E.; Dou, L.; Fu, A.; Yang, P. Growth and Anion Exchange Conversion of $CH_3NH_3PbX_3$ Nanorod Arrays for Light-Emitting Diodes. *Nano Lett.* **2015**, *15*, 5519–5524.

(53) Akkerman, Q. A.; D'Innocenzo, V.; Accornero, S.; Scarpellini, A.; Petrozza, A.; Prato, M.; Manna, L. Tuning the Optical Properties of Cesium Lead Halide Perovskite Nanocrystals by Anion Exchange Reactions. *J. Am. Chem. Soc.* **2015**, *137*, 10276–10281.

(54) Zhu, W.; Bao, C.; Li, F.; Yu, T.; Gao, H.; Yi, Y.; Yang, J.; Fu, G.; Zhou, X.; Zou, Z. A Halide Exchange Engineering for $CH_3NH_3PbI_{3-x}Br_x$ Perovskite Solar Cells with High Performance and Stability. *Nano Energy* **2016**, *19*, 17–26.

(55) Li, G.; Ho, J. Y.-L.; Wong, M.; Kwok, H. S. Reversible Anion Exchange Reaction in Solid Halide Perovskites and Its Implication in Photovoltaics. *J. Phys. Chem. C* **2015**, *119*, 26883–26888.

(56) Yuan, Y.; Huang, J. Ion Migration in Organometal Trihalide Perovskite and Its Impact on Photovoltaic Efficiency and Stability. *Acc. Chem. Res.* **2016**, *49*, 286–293.

(57) Eames, C.; Frost, J. M.; Barnes, P. R. F.; O'Regan, B. C.; Walsh, A.; Islam, M. S. Ionic Transport in Hybrid Lead Iodide Perovskite Solar Cells. *Nat. Commun.* **2015**, *6*, 7494, 1–8, DOI: 10.1038/ncomms8497.

(58) Dybowski, C.; Neue, G. Solid State ^{207}Pb NMR Spectroscopy. *Prog. NMR Spec.* **2002**, *41*, 153–170.

(59) Wrackmeyer, B. Application of ^{207}Pb NMR Parameters. *Ann. Rep. NMR Spec.* **2002**, *47*, 1–37.

(60) Dmitrenko, O.; Bai, S.; Beckmann, P. A.; Van Bramer, S.; Vega, A.; Dybowski, C. The Relationship between ^{207}Pb NMR Chemical Shift and Solid-State Structure in Pb(II) Compounds. *J. Phys. Chem. A* **2008**, *112*, 3046–3052.

(61) Fayon, F.; Farnan, I.; Bessada, C.; Coutures, J.; Massiot, D.; Coutures, J. P. Empirical Correlations Between ^{207}Pb NMR Chemical Shifts and Structure in Solids. *J. Am. Chem. Soc.* **1997**, *119*, 6837–6843.

(62) Dmitrenko, O.; Bai, S.; Dybowski, C. Prediction of ^{207}Pb NMR Parameters for the Solid Ionic Lead(II) Halides Using the Relativistic ZORA-DFT Formalism: Comparison with the Lead-Containing Molecular Systems. *Sol. St. NMR* **2008**, *34*, 186–190.

(63) Dybowski, C.; Smith, M. L.; Hepp, M. A.; Gaffney, E. J.; Neue, G.; Perry, D. L. ^{207}Pb NMR Chemical-Shift Tensors of the Lead (II) Halides and the Lead (II) Hydroxyhalides. *App. Spec.* **1998**, *52*, 426–429.

(64) Suits, B. H.; White, D. NMR Chemical Shifts and the Electronic Structure of Lead in Lead Halides. *J. Mag. Res.* **1989**, *82*, 441–453.

(65) Taylor, R. E.; Beckmann, P. A.; Bai, S.; Dybowski, C. ^{127}I and ^{207}Pb Solid-State NMR Spectroscopy and Nuclear Spin Relaxation in PbI_2: A Preliminary Study. *J. Phys. Chem. C* **2014**, *118*, 9143–9153.

(66) Glatfelter, A.; Stephenson, N.; Bai, S.; Dybowski, C.; Perry, D. L. Quantitative Determination of Lead in Mixtures of Lead(II) Halides Using Solid-State ^{207}Pb NMR Spectroscopy. *Analyst* **2006**, *131*, 1207–1209.

(67) Glatfelter, A.; Dybowski, C.; Kragten, D. D.; Bai, S.; Perry, D. L.; Lockard, J. Solid-State ^{207}Pb NMR Studies of Mixed Lead Halides, PbFX (X = Cl, Br, or I). *Spec. Acta Part A* **2007**, *66*, 1361–1363.

(68) Wasylishen, R. E.; Knop, O.; Macdonald, J. B. Cation Rotation in Methylammonium Lead Halides. *Solid State Commun.* **1985**, *56*, 581–582.

(69) Knop, O.; Wasylishen, R. E.; White, M. A.; Cameron, T. S.; Vanoort, M. J. M. Alkylammonium Lead Halides .2. $CH_3NH_3PbCl_3$, $CH_3NH_3PbBr_3$, $CH_3NH_3PbI_3$ Perovskites – Cuboctahedral Halide Cages with Isotropic Cation Reorientation. *Can. J. Chem.* **1990**, *68*, 412–422.

(70) Xu, Q.; Eguchi, T.; Nakayama, H.; Nakamura, N.; Kishita, M. Molecular Motions and Phase-Transitions in Solid $CH_3NH_3PbCl_3$, $CH_3NH_3PbBr_3$, $CH_3NH_3PbI_3$, as Studied by NMR and NQR. *Z. Naturforsch. A – J. Phys. Sci.* **1991**, *46*, 240–246.

(71) Baikie, T.; Barrow, N. S.; Fang, Y.; Keenan, P. J.; Slater, P. R.; Piltz, R. O.; Gutmann, M.; Mhaisalkar, S. G.; White, T. J. A Combined Single Crystal Neutron/X-Ray Diffraction and Solid-State Nuclear Magnetic Resonance Study of the Hybrid Perovskites $CH_3NH_3PbX_3$ (X = I, Br and Cl). *J. Mater. Chem. A* **2015**, *3*, 9298–9307.

(72) Hume-Rothery, W. Researches on the Nature, Properties, and Conditions of Formation of Intermetallic Compounds, with Special Reference to Certain Compounds of Tin.-I.-V. *J. Inst. Met.* **1926**, *35*, 295–348.

(73) Vegard, L. Die Konstitution der Mischkristalle und die Raumfüllung der Atome. *Zeit. Phys.* **1921**, *5*, 17–26.

(74) Denton, A. R.; Ashcroft, N. W. Vegard's Law. *Phys. Rev. A* **1991**, *43*, 6, 3161–3164.

(75) Stoumpos, C.C.; Malliakas, C.D.; Kanatzidis, M. G. Semiconducting Tin and Lead Iodide Perovskites with Organic Cations: Phase Transitions, High Mobilities, and Near-Infrared Photoluminescent Properties. *Inorg. Chem.* **2013**, *52*, 9019–9038.

(76) Su, J.; Chen, D.P.; Lin, C.T. Growth of Large $CH_3NH_3PbX_3$ (X = I, Br) Single Crystals in Solution. *J. Cryst. Growth* **2015**, *422*, 75–79.

(77) Chi, L.; Swainson, I; Cranswick, L.; Her, J.-H.; Stephens, P.; Knop, O. The Ordered Phase of Methylammonium Lead Chloride $CH_3ND_3PbCl_3$. *J. Solid State Chem.* **2005**, *178*, 1376–1385.

(78) Taylor, R. E.; Alkan, F.; Koumoulis, D.; Lake, M. P.; King, D.; Dybowski, C.; Bouchard, L.-S. A Combined NMR and DFT Study of Narrow Gap Semiconductors: The Case of PbTe. *J. Phys. Chem. C* **2013**, *117*, 17, 8959–8967.

(79) Koumoulis, D.; Taylor, R. E.; King, D. Jr.; Bouchard, L.-S. NMR Study of Native Defects in PbSe. *Phys. Rev. B* **2014**, *90*, 125201, 1–6.

(80) Shmyreva, A. A.; Safdari, M.; Furó, I.; Dvinskikh, S. V. NMR longitudinal Relaxation Enhancement in Metal Halides by Heteronuclear Polarization Exchange During Magic-Angle Spinning. *J. Chem. Phys.* **2016**, *144*, 224201, 1–5.

(81) Smith, J. V.; Blackwell, S. Nuclear Magnetic Resonance of Silica Polymorphs. *Nature* **1983**, *303*, 223–225.

(82) Findik, F. Improvements in Spinodal Alloys from Past to Present. *Mater. Des.* **2012**, *42*, 131–146.

(83) Binder, K.; Billotet, C.; Mirold, P. On the Theory of Spinodal Decomposition in Solid and Liquid Binary Mixtures. *Z. Phys. B* **1978**, *30*, 183–195.

(84) Binder, K. Spinodal Decomposition in Confined Geometry. *J. Non-Equilib. Thermodyn.* ***1998****, 23, 1–44.*

(85) Androulakis, J.; Lin, C.-H.; Kong, H.-J.; Uher, C.; Wu, C.-I.; Hogan, T.; Cook, B. A.; Caillat, T.; Paraskevopoulos, K. M.; Kanatzidis, M. G. Spinodal Decomposition and Nucleation and Growth as a Means to Bulk Nanostructured Thermoelectrics: Enhanced Performance in $Pb_{1-x}Sn_xTe$-PbS. *J. Am. Chem. Soc.* **2007**, *129*, 9780–9788.

(86) Dualeh, A.; Gao, P.; Seok, S. I.; Nazeeruddin, M. K.; Grätzel, M. Thermal Behavior of Methylammonium Lead-Trihalide Perovskite Photovoltaic Light Harvesters. *Chem. Mater.* **2014**, *26*, 6160–6164.

(87) Borchert, J.; Boht, H.; Fränzel, W.; Csuk, R.; Scheer, R. Structural Investigation of Co-Evaporated Methylammonium Lead Halide Perovskite Films During Growth and Thermal Decomposition Using Different PbX_2 (X = I, Cl) Precursors. *J. Mater. Chem. A* **2015**, *3*, 19842–19849.

(88) Williams, A. E.; Holliman, P. J.; Carnie, M. J.; Davies, M. L.; Worsley, D. A.; Watson, R. M. Perovskite Processing for Photovoltaics: A Spectrothermal Evaluation. *J. Mater. Chem. A* **2014**, *2*, 19338–19346.

(89) Tang, L.-D.; Mei, H.; Wang, B.; Peng, S. Study on Structure, Thermal Stabilization and Light Absorption of Lead-Bromide Perovskite Light Harvesters. *J. Mater. Sci: Mater. Electron.* **2015**, *26*, 8726–8731.

(90) Reichert, M. D.; Lin, C.-C.; Vela, J. How Robust Are Semiconductor Nanorods? Investigating the Stability and Chemical Decomposition Pathways of Photoactive Nanocrystals. *Chem. Mater.* **2014**, *26*, 3900–3908.

(91) Lee, M. M.; Teuscher, J.; Miyasaka, T.; Murakami, T. N.; Snaith, H. J. Efficient Hybrid Solar Cells Based on Meso-Superstructured Organometal Halide Perovskites. *Science* **2012**, 338, 643–647.

(92) Tauc, J.; Grigorovici, R.; Vancu, A. Optical Properties and Electronic Structure of Amorphous Germanium. *Phys. Stat. Sol.* **1966**, *15*, 627–637.

(93) Cory, D. G.; Ritchey, W. M. Suppression of Signals from the Probe in Bloch Decay Spectra. *J. Mag. Res.* **1969**, *80*, 1, 128–132.

Appendix of supporting information

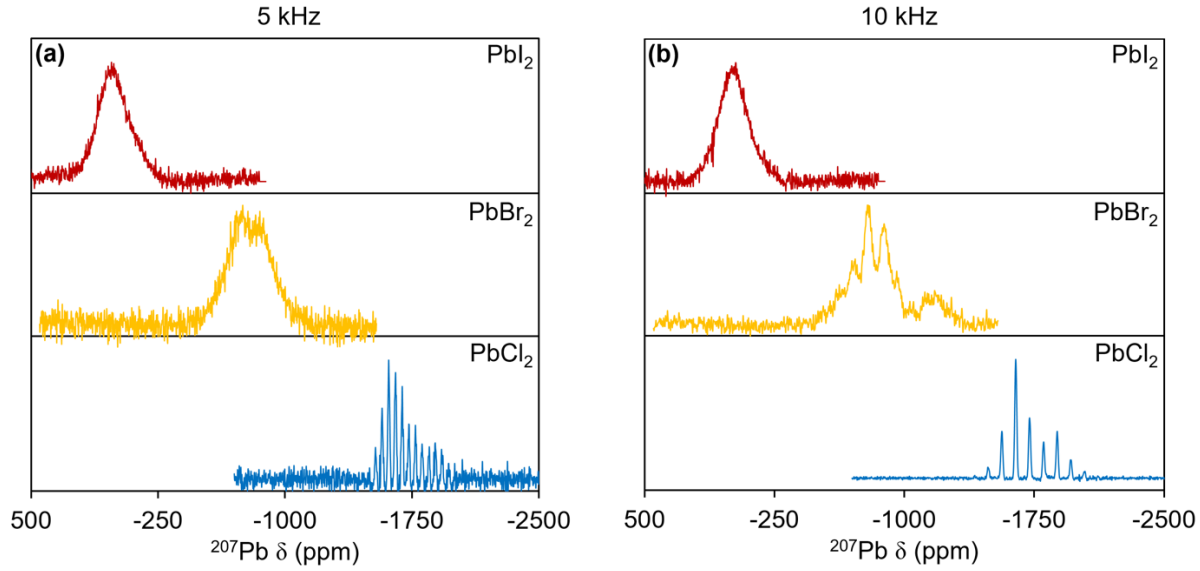

Figure S1. ^{207}Pb ssNMR spectra of PbX_2 (X = I, Br, Cl) under 5 kHz (a) and 10 kHz (b) spinning conditions at 22 °C.[S1-S6]

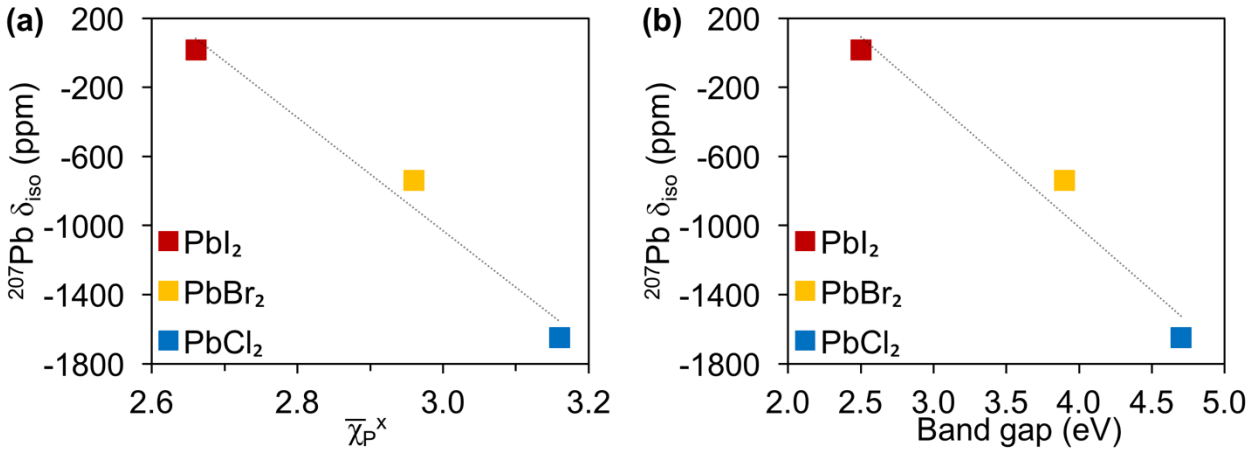

Figure S2. ^{207}Pb δ_{iso} as a function of average halogen Pauling electronegativity (a) and band gap (b) for PbX_2 (X = I, Br, Cl).[S1-S6]

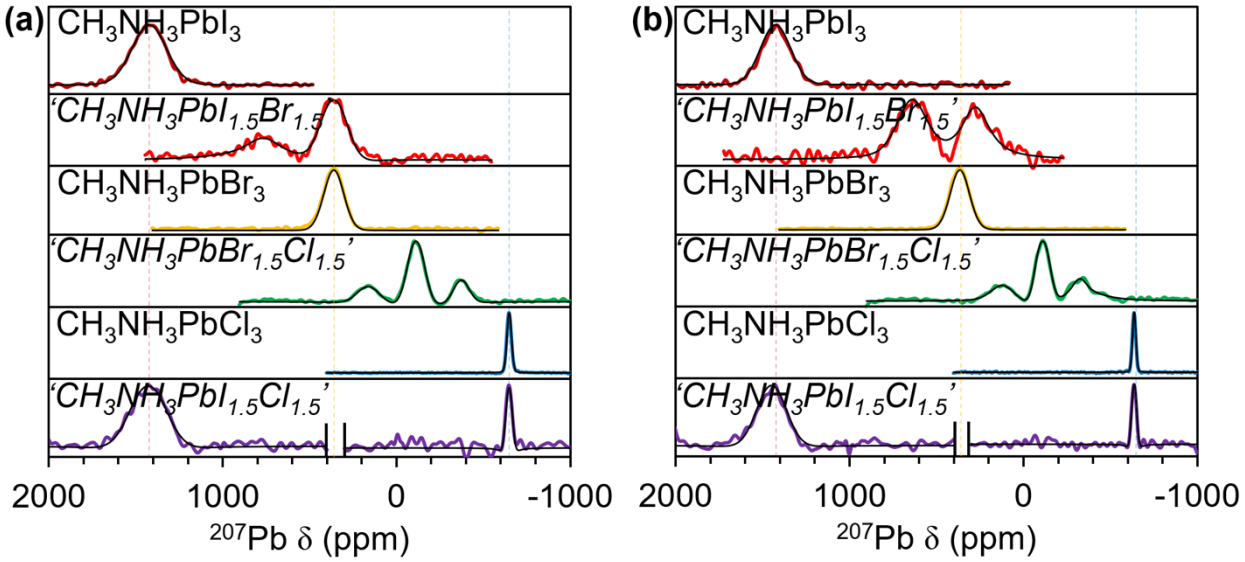

Figure S3. ^{207}Pb ssNMR spectra of single- and mixed-halide organolead perovskites prepared by solution phase synthesis under static (a) and 10 kHz (b) spinning conditions at 22 °C. Solid black lines were fit using Bruker's Topspin 3.0 software. Italicized formulas in quotation marks were calculated from synthetic loading while formulas in regular script are compositional assignments made from all experimental data.

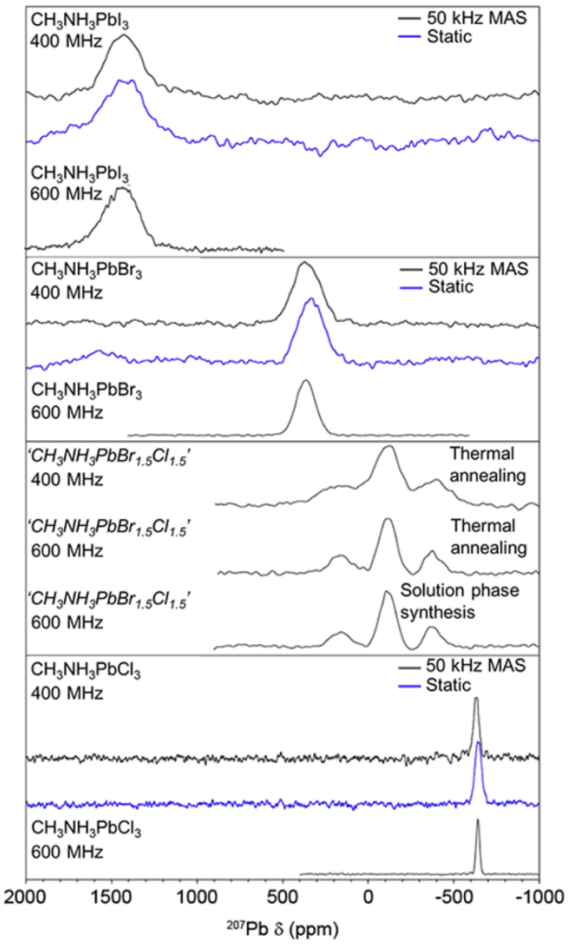

Figure S4. Comparison of ^{207}Pb ssNMR spectra collected at different magnetic field strengths (9.4 T, 400 MHz or 16.4 T, 600 MHz) and rotor sample rotation rates (static samples or samples undergoing MAS with a frequency of 50 kHz)., Static ^{207}Pb ssNMR spectra obtained at 9.4 T and 16.4 T are compared for $CH_3NH_3PbX_3$ (X = I, Br, Cl) and thermal annealing *'$CH_3NH_3PbBr_{1.5}Cl_{1.5}$'* samples. A 600 MHz ssNMR spectrum for *'$CH_3NH_3PbBr_{1.5}Cl_{1.5}$'* prepared by solution phase synthesis is included for comparison. Static and 50 kHz MAS ^{207}Pb ssNMR spectra obtained at 9.4 T are compared for the pure halides. In all cases, there is an improvement in resolution at higher field (i.e., the peak widths in ppm are reduced at higher field), consistent with homogeneous broadening. There are negligible differences in peak width between the static and MAS NMR spectra in all cases. There are slight differences in ^{207}Pb isotropic chemical shift in the static and MAS ssNMR spectra due to differences in sample temperature caused by frictional heating under MAS. Peak widths and ^{207}Pb relaxation time constants are summarized in Table S1.

Table S1. ^{207}Pb transverse and longitudinal relaxation time constants for $CH_3NH_3PbX_3$ (X = I, Br, Cl) at room temperature and a static magnetic field of 9.4 T (400 MHz).[a]

	MAS at 50 kHz				*Static*			
Compound	T_1 (ms)[b]	T_2' (µs)[c]	fwhm (kHz)[d]	T_2* (µs)[e]	T_1 (ms)	T_2' (µs)	fwhm (kHz)	T_2* (µs)
$CH_3NH_3PbI_3$	83	19	21.1 (0.6)	15	1069	26	25.9 (0.70)	12
$CH_3NH_3PbBr_3$	104	87	15.9 (0.91)	20	1538	63	14.4 (1.0)	21
$CH_3NH_3PbCl_3$	1657	552	3.0 (0.37)	107	1385	321	3.7 (0.75)	86

[a]The corresponding ^{207}Pb SSNMR spectra are shown in Figure S4. [b]Longitudinal relaxation time constant measured with a saturation recovery experiment. [c]Refocused transverse relaxation time constant measured with a spin echo experiment (rotor was synchronized in the case of MAS). [d]Full width at half maximum (fwhm), measured by fitting the peak width of the ^{207}Pb ssNMR spectrum to a mixed Gaussian/Lorentzian function. The Gaussian fraction is given in parentheses. [e]Apparent transverse relaxation time constant where $T_2^* = 1/(\pi \times \text{fwhm})$.

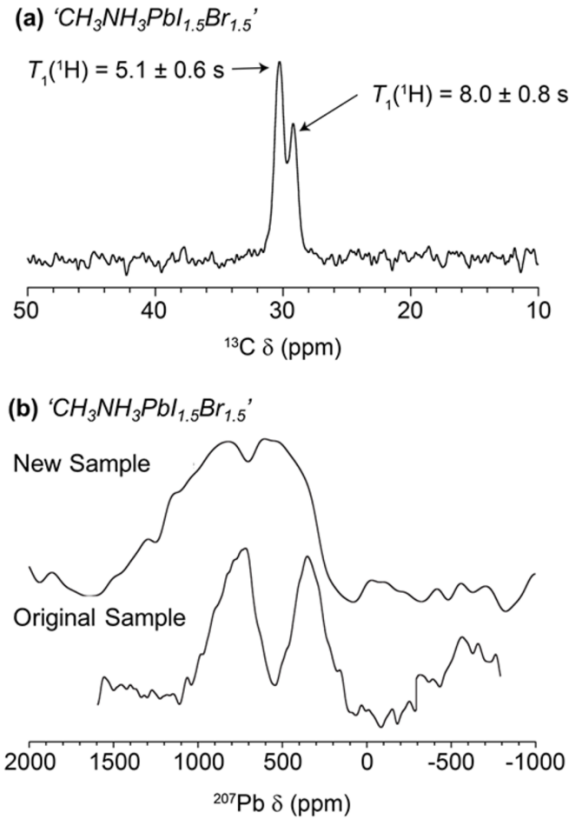

Figure S5: ^{13}C of a new sample of *"$CH_3NH_3PbI_{1.5}Br_{1.5}$"* and comparison of ^{207}Pb ssNMR spectra of this sample to another representative sample of *"$CH_3NH_3PbI_{1.5}Br_{1.5}$."* (a) ^{13}C CPMAS ssNMR spectrum of the new sample of *"$CH_3NH_3PbI_{1.5}Br_{1.5}$"* obtained using a 2.5 mm rotor under 18 kHz MAS with 512 scans and a 30 second recycle delay. A ^{13}C detected ^{1}H saturation recovery experiment was performed to measure the proton T_1's associated with the two observed ^{13}C peaks. The observation of distinct proton T_1's suggests that there are multiple segregated domains within the sample. The saturation recovery curves where fit to the equation $S(t)=S(0)[1-\exp(-t/T_1)]$ to

obtain the T_1 values. (b) Static ^{207}Pb ssNMR spectra of two different samples of *"$CH_3NH_3PbBr_{1.5}I_{1.5}$"*. The spectrum of the original sample was obtained using a 4 mm rotor and the DEPTH pulse sequence. Due to a lower ^{207}Pb rf field (4.95 μs 90 and 9.90 μs 180 pulses) the spectrum of the original sample was obtained by co-adding ^{207}Pb ssNMR spectra acquired with transmitter offsets of 400 ppm (4640 scans) and 900 ppm (5888 scans) ppm. The spectrum with an offset of 400 ppm was scaled by 1.269 before co-addition of the different pieces to account for differences in the number of scans. The spectrum of the second sample was obtained with a single transmitter offset. A 2.5 mm rotor and a spin echo pulse sequence with a total echo delay of 33.3 μs, 16384 scans and 3.05 μs 90° and 6.10 μs 180° pulses was used. In both cases a 10 s recycle delay was used.

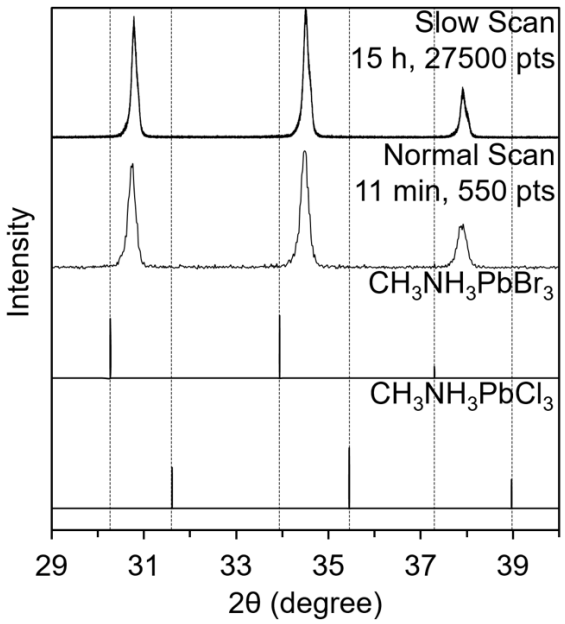

Figure S6. Powder XRD measurements collected on *'$CH_3NH_3PbBr_{1.5}Cl_{1.5}$'* made by solution phase synthesis between 2θ = 29-40 degrees as a function of scan rate (0.0126 degrees/min, 0.0005 degrees/step, 27500 points over 15 h (top) *vs.* 1 degree/min, 0.02 degrees/step, 550 points over 11 min (second from top). The standard bulk powder XRD patterns reported for cubic $CH_3NH_3PbBr_3$ (third from top) and cubic $CH_3NH_3PbCl_3$ are shown for comparison (bottom).

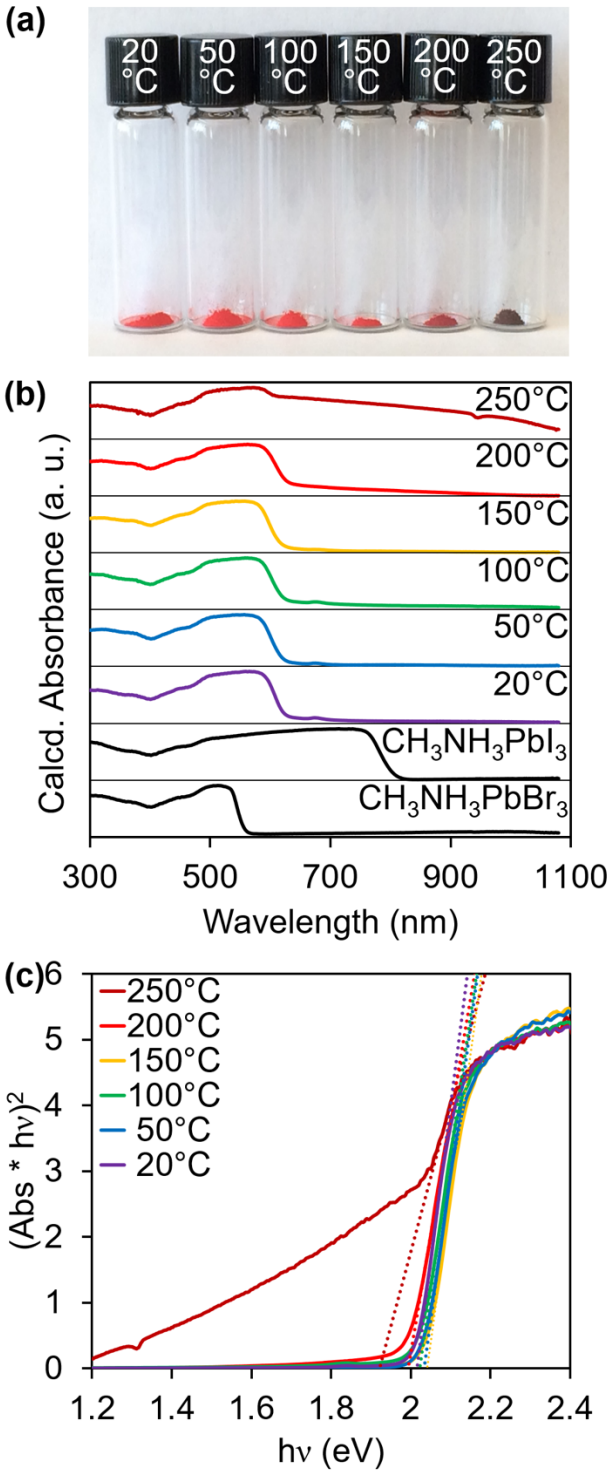

(d)

Temp (°C)	Band Gap (eV)	Band Gap (nm)
250	1.92	645
200	1.99	622
150	2.04	608
100	2.02	613
50	2.03	610
20	2.02	615

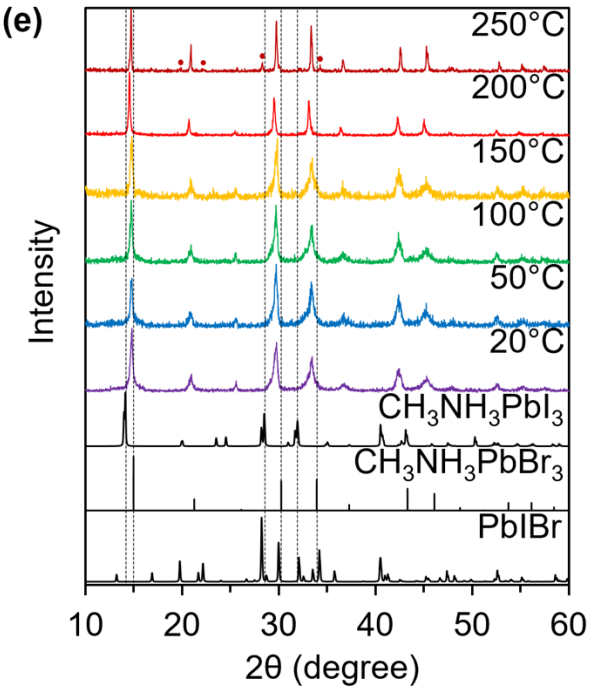

Figure S7. Visual image (a), diffuse reflectance (b), tauc plot (c), band gap (d), and powder XRD data (e) for *'$CH_3NH_3PbI_{1.5}Br_{1.5}$'* made by thermal annealing to different temperatures (see Methods). Annealing to 250 °C results in partial decomposition to PbIBr.

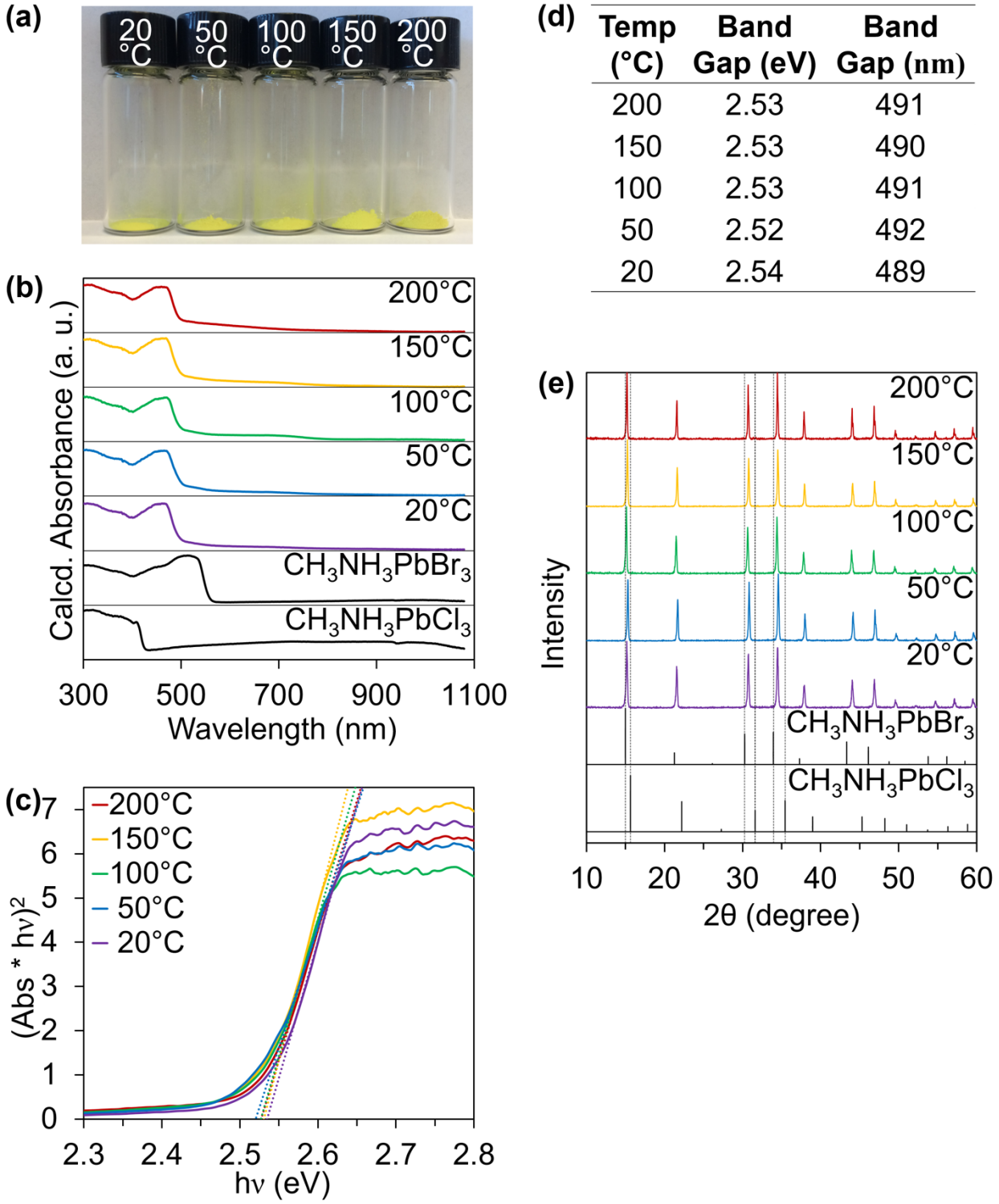

Temp (°C)	Band Gap (eV)	Band Gap (nm)
200	2.53	491
150	2.53	490
100	2.53	491
50	2.52	492
20	2.54	489

Figure S8. Visual image (a), diffuse reflectance (b), tauc plot (c), band gap (d), and powder XRD data (e) for *'$CH_3NH_3PbBr_{1.5}Cl_{1.5}$'* made by thermal annealing at different temperatures (see Methods).

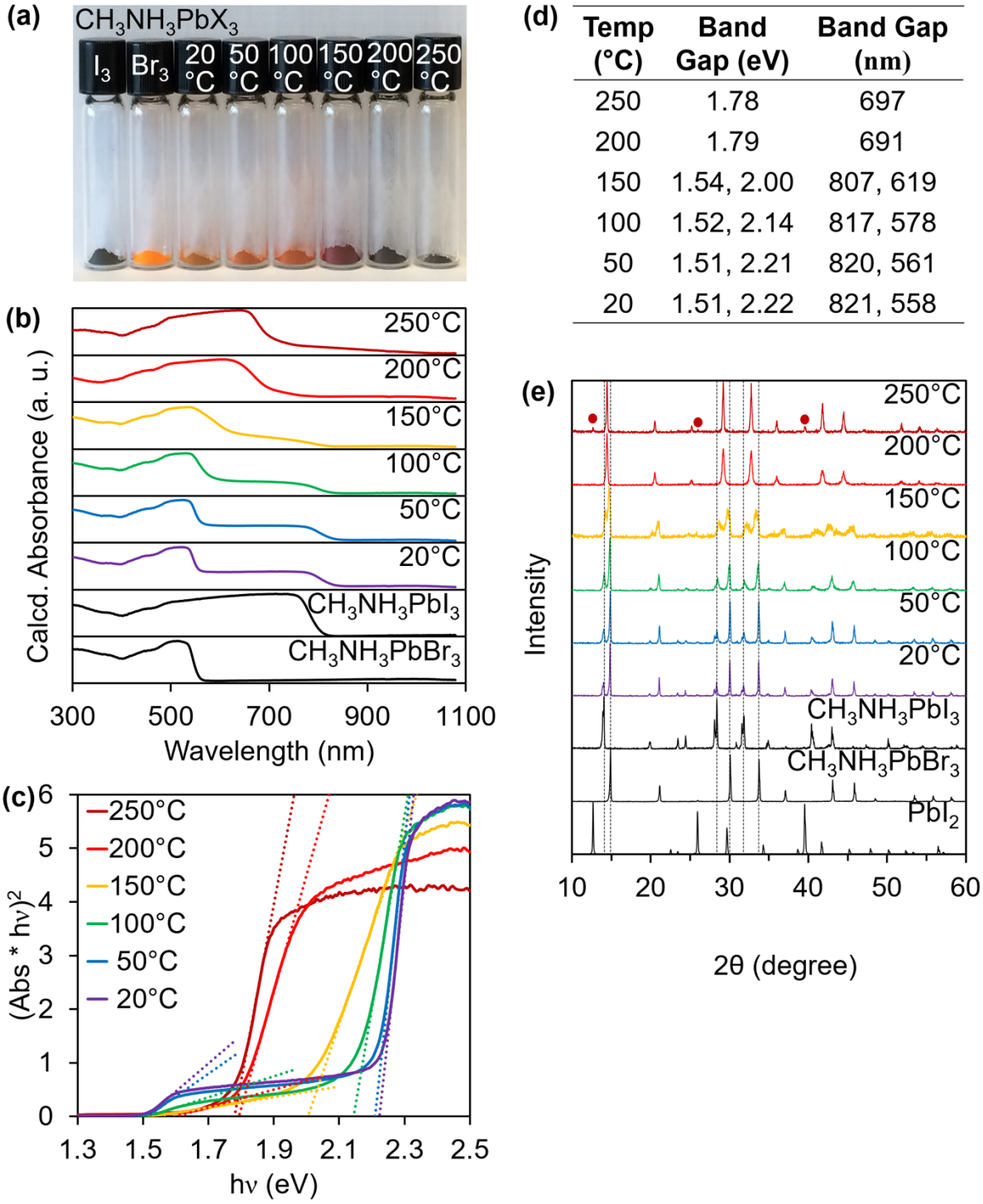

Temp (°C)	Band Gap (eV)	Band Gap (nm)
250	1.78	697
200	1.79	691
150	1.54, 2.00	807, 619
100	1.52, 2.14	817, 578
50	1.51, 2.21	820, 561
20	1.51, 2.22	821, 558

Figure S9. Visual image (a), diffuse reflectance (b), tauc plot (c), band gap (d), and powder XRD data (e) for *'$CH_3NH_3PbI_{1.5}Br_{1.5}$'* made by solid phase synthesis starting from an equimolar mixture of $CH_3NH_3PbI_3$ and $CH_3NH_3PbBr_3$ (see Methods). Annealing to 250 °C results in partial decomposition to PbI_2.

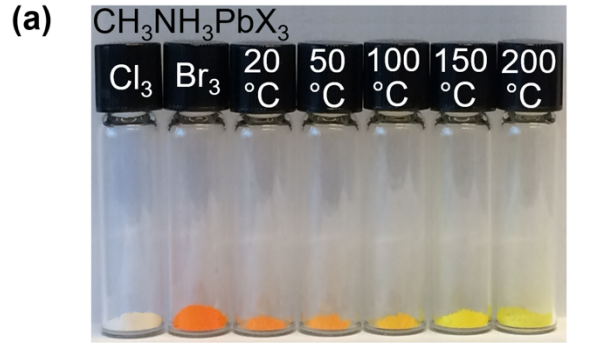

Temp (°C)	Band Gap (eV)	Band Gap (nm)
200	2.49	498
150	2.48	500
100	2.31	537
50	2.26	548
20	2.25	551

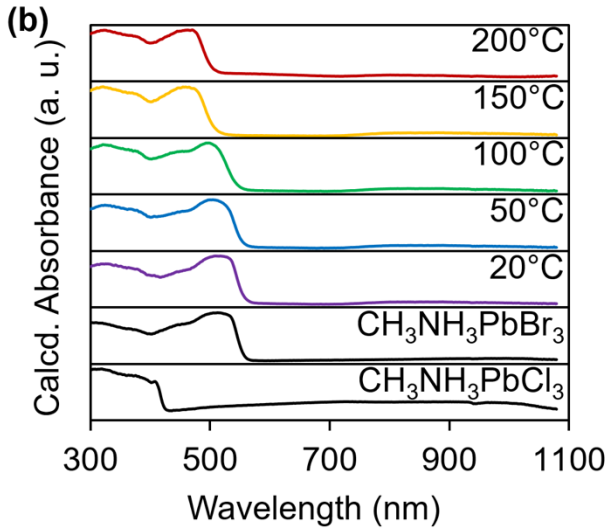

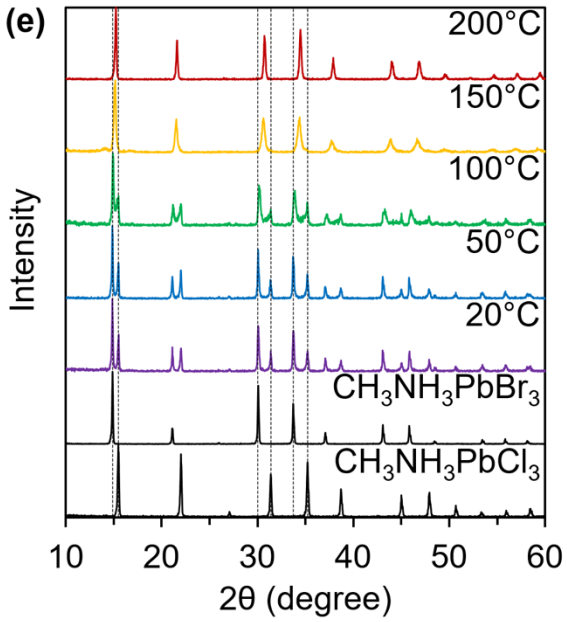

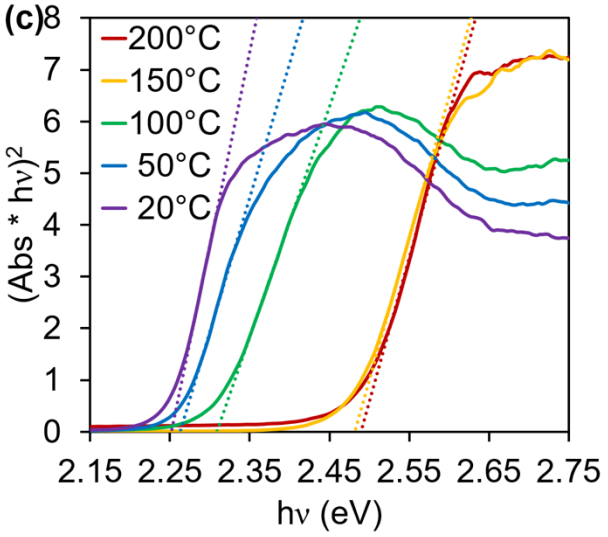

Figure S10. Visual image (a), diffuse reflectance (b), tauc plot (c), band gap (d), and powder XRD data (e) for *'$CH_3NH_3PbBr_{1.5}Cl_{1.5}$'* made by solid phase synthesis starting from an equimolar mixture of $CH_3NH_3PbBr_3$ and $CH_3NH_3PbCl_3$ (see Methods). The absorption edge of $CH_3NH_3PbCl_3$ is hard to see because of lower instrument spectral sensitivity at shorter wavelengths (see Figure S11 below).

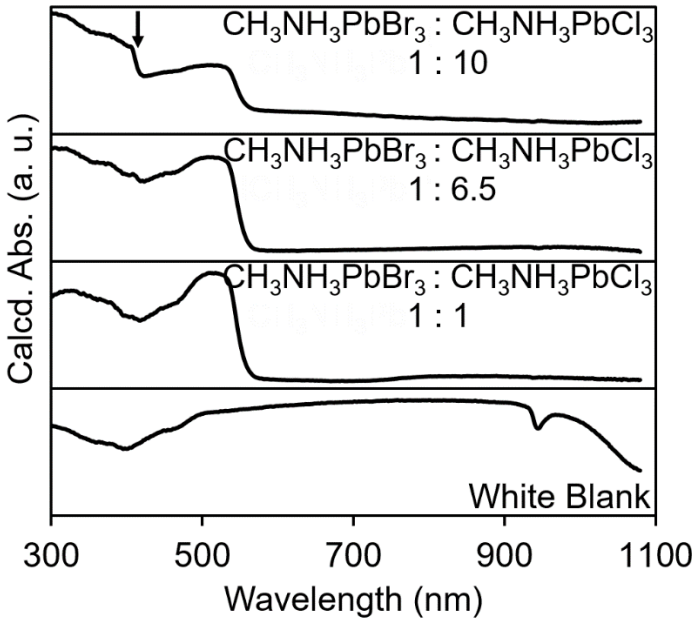

Figure S11. The absorption edge of excess $CH_3NH_3PbCl_3$ (arrow on top spectrum) is clearly observed in a 10:1 mixture of $CH_3NH_3PbCl_3$ and $CH_3NH_3PbBr_3$.

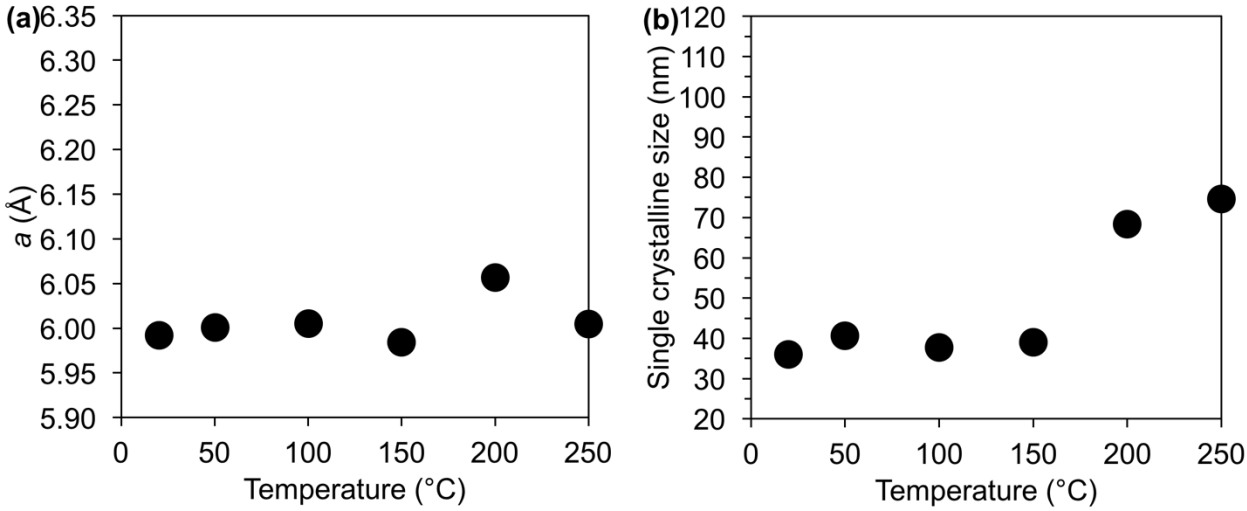

Figure S12. Lattice parameter (a) and single crystalline size (b) for *'$CH_3NH_3PbI_{1.5}Br_{1.5}$'* made by thermal annealing as a function of temperature (see Methods). An increase in single crystalline size due to particle coalescence occurs above 150 °C.

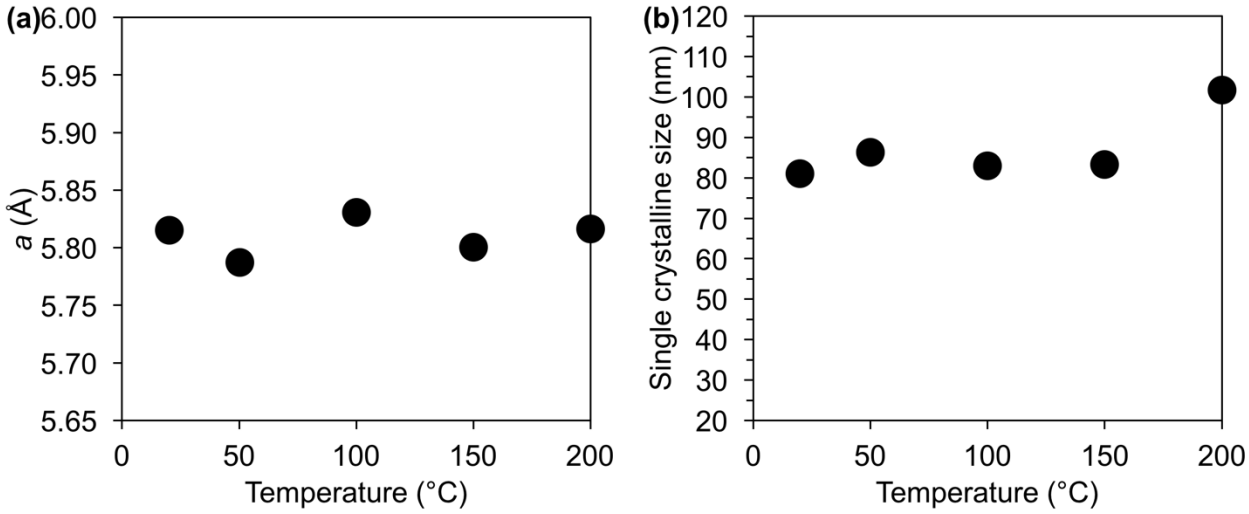

Figure S13. Lattice parameter (a) and single crystalline size (b) for *'$CH_3NH_3PbBr_{1.5}Cl_{1.5}$'* made by thermal annealing as a function of temperature (see Methods). An increase in single crystalline size due to particle coalescence starts occurring above 100-150 °C.

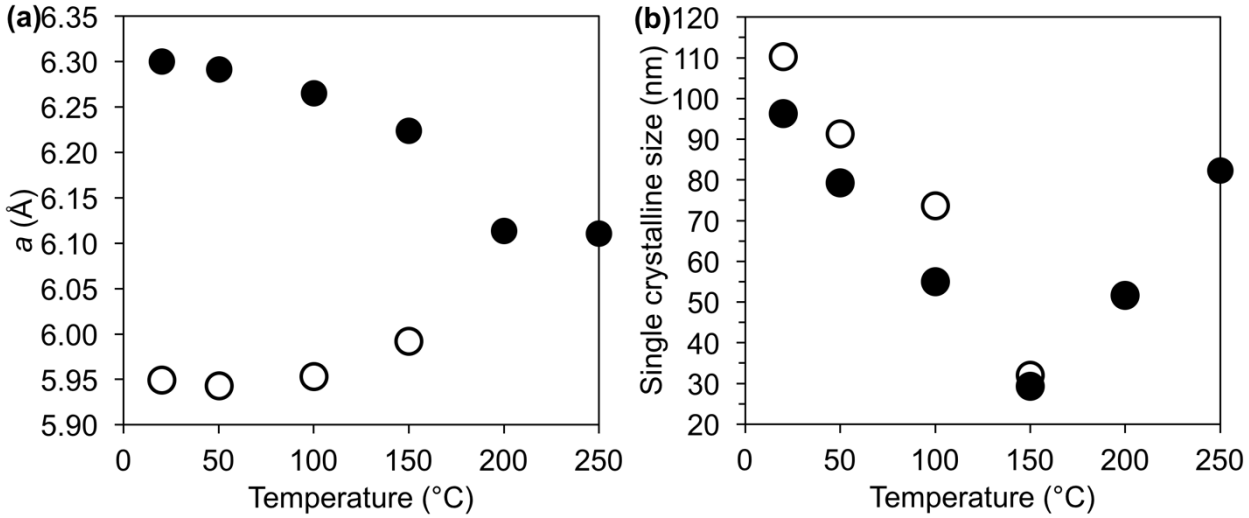

Figure S14. Lattice parameter (a) and single crystalline size (b) for *'$CH_3NH_3PbI_{1.5}Br_{1.5}$'* made by solid phase synthesis starting from an equimolar mixture of $CH_3NH_3PbI_3$ (solid circles) and $CH_3NH_3PbBr_3$ (hollow circles) as a function of temperature (see Methods). The two sets of XRD peaks merge into one near 200 °C (a). Following an initial steady decrease in single crystalline size due to nucleation of the new mixed-halide phase, particle coalescence leads to larger single crystalline sizes above 150 °C (b).

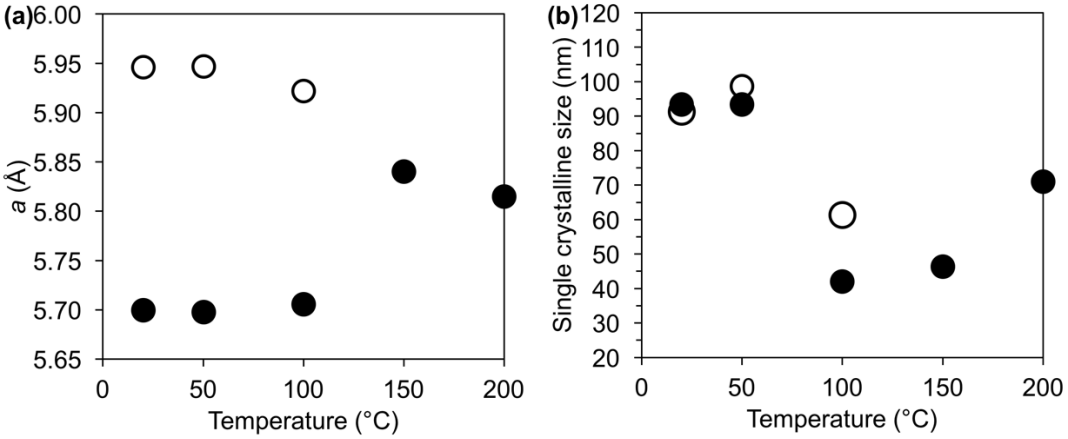

Figure S15. Lattice parameter (a) and single crystalline size (b) for *'$CH_3NH_3PbBr_{1.5}Cl_{1.5}$'* made by solid phase synthesis starting from an equimolar mixture of $CH_3NH_3PbBr_3$ (hollow circles) and $CH_3NH_3PbCl_3$ (solid circles) as a function of temperature (see Methods). The two sets of XRD peaks become one near 150 °C (a). After a sudden decrease in single crystalline size due to nucleation of the new mixed-halide phase at 50-100 °C, particle coalescence leads to larger single crystalline sizes above 100-150 °C (b).

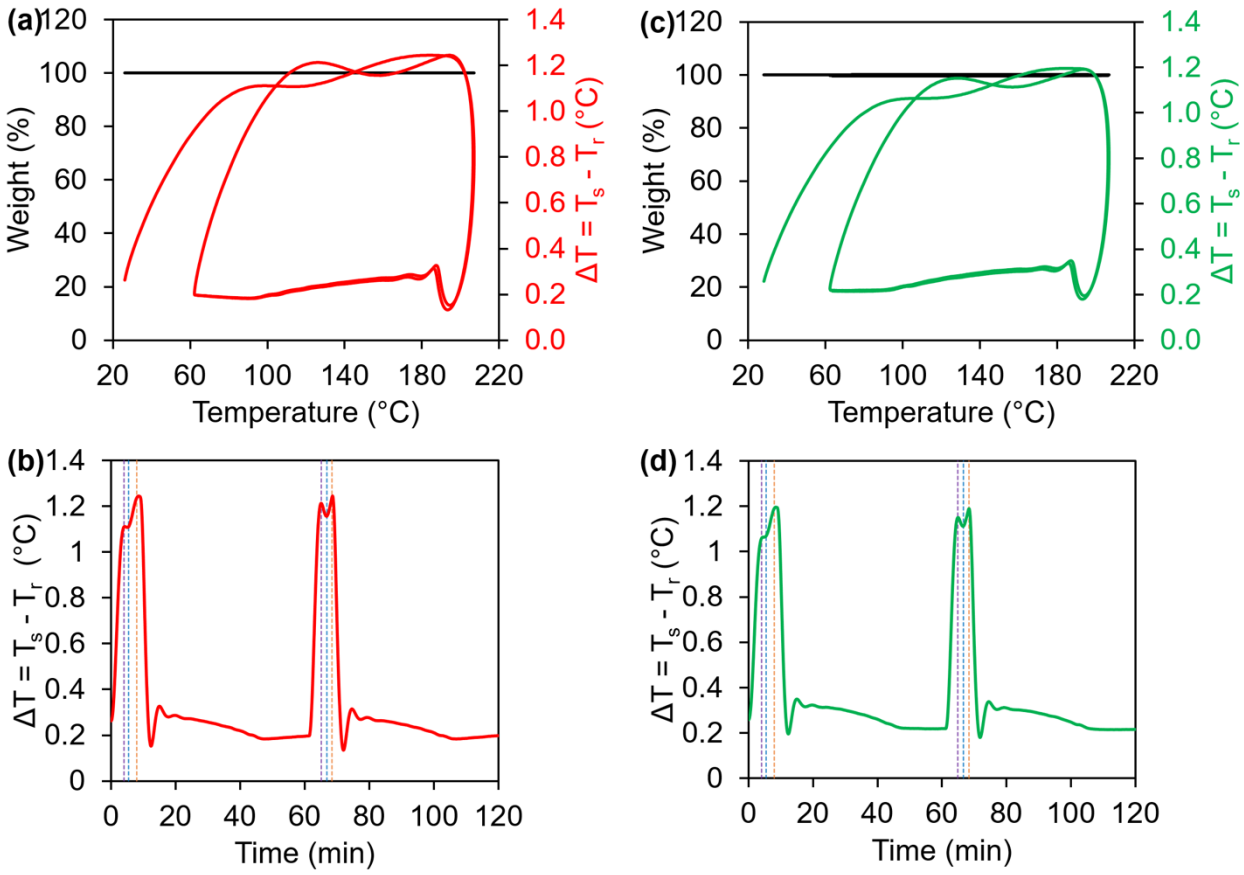

'CH3NH3I1.5Br1.5'	Onset		Peak		Finish	
	t (min)	T (°C)	t (min)	T (°C)	t (min)	T (°C)
Cycle 1	4.0	94	5.4	121	8.0	173
Cycle 2	65.1	127	66.9	161	68.5	192

'CH3NH3Br1.5Cl1.5'	Onset		Peak		Finish	
	t (min)	T (°C)	t (min)	T (°C)	t (min)	T (°C)
Cycle 1	4.1	97	5.5	124	8.0	174
Cycle 2	64.9	125	66.6	157	68.4	192

Figure S16. Simultaneous differential thermal analysis–thermogravimetric analysis (DTA–TGA) measurements (a, c), and DTA *vs.* time plots (b, d) for the solid phase synthesis of *'$CH_3NH_3PbI_{1.5}Br_{1.5}$'* (a, b) and *'$CH_3NH_3PbBr_{1.5}Cl_{1.5}$'* (c, d) from an equimolar mixture of the parent halides (20 °C/min ramp rate, see Methods).

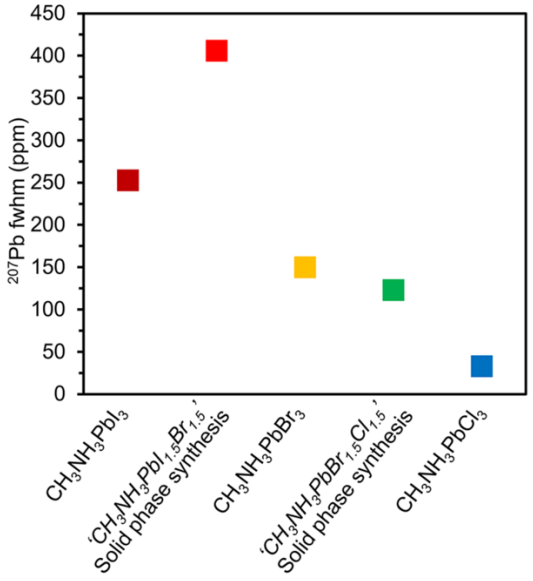

Figure S17. Full width at half maximum (fwhm) of the ^{207}Pb ssNMR peaks as a function of perovskite composition. The only ^{207}Pb resonance observed for *'$CH_3NH_3PbI_{1.5}Br_{1.5}$'* made by solid phase synthesis is clearly too broad (has a very large fwhm) compared to the ^{207}Pb resonances observed for all other perovskite samples, indicating that it is a composite of multiple unresolved peaks corresponding to different lead environments.

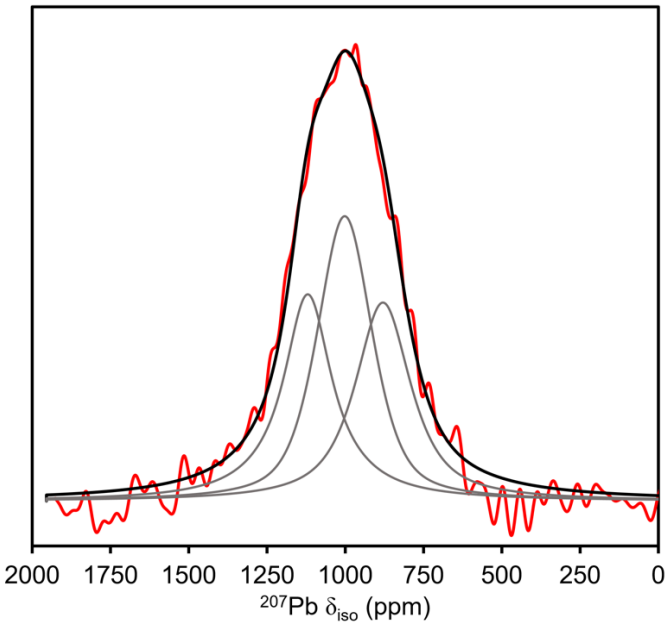

Figure S18. Deconvolution of the broad ^{207}Pb ssNMR peak observed for *'$CH_3NH_3PbI_{1.5}Br_{1.5}$'* made by solid state synthesis (see Methods).

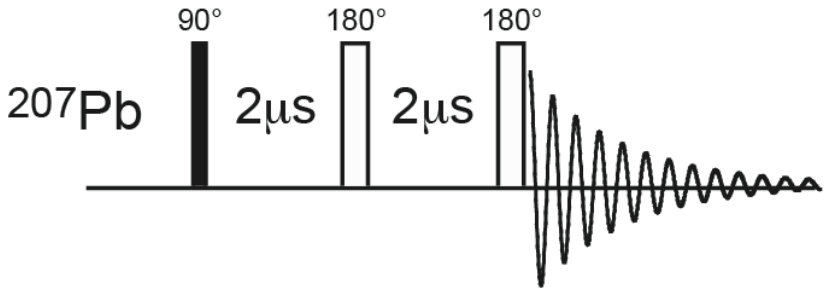

Figure S19. DEPTH pulse sequence consisting of an initial 90° pulse followed by two 180° pulses spaced by a 2 μs delay to eliminate ^{207}Pb probe background signals.

Table S2. ^{207}Pb ssNMR data for organolead halide perovskites.

Synthetic loading[a]	δ_{iso} (ppm)	Linewidth (Hz)[b]	xG/(1-x)L[b]	%overlap[b]	Compositional assignment(s)[c]	Phase[d] (%[e])
Solution phase synthesis						
'$CH_3NH_3PbI_3$'	1423	29425	0.9152	93.7	$CH_3NH_3PbI_3$	C (100)
'$CH_3NH_3PbI_{1.5}Br_{1.5}$'	774	34300	0.0000	88.9	$CH_3NH_3PbIBr_2$	C (26)
	361	21456	1.0000		$CH_3NH_3PbBr_3$	A (74)[f]
'$CH_3NH_3PbBr_3$'	361	16956	0.9867	93.3	$CH_3NH_3PbBr_3$	C (100)
'$CH_3NH_3PbBr_{1.5}Cl_{1.5}$'	160	16697	1.0000	93.7	$CH_3NH_3PbBr_{2.25}Cl_{0.75}$	D (1)
	-117	13922	1.0000		$CH_3NH_3PbBr_{1.5}Cl_{1.5}$	C (56)
	-379	14158	1.0000		$CH_3NH_3PbBr_{0.75}Cl_{2.25}$	D (23)
'$CH_3NH_3PbCl_3$'	-648	3902	0.8542	90.7	$CH_3NH_3PbCl_3$	C (100)
'$CH_3NH_3PbI_{1.5}Cl_{1.5}$'	1427	29384	1.0000	86.0	$CH_3NH_3PbI_3$	C (n.d.)
	-647	4924	1.0000	64.9	$CH_3NH_3PbCl_3$	C (n.d.)
Thermal annealing[g]						
'$CH_3NH_3PbI_{1.5}Br_{1.5}$'	778	25398	1.0000	90.4	$CH_3NH_3PbIBr_2$	C (53)
	343	19029	0.9152		$CH_3NH_3PbBr_3$	A or /s (47)[f]
'$CH_3NH_3PbBr_{1.5}Cl_{1.5}$'	166	17202	0.5569	91.8	$CH_3NH_3PbBr_{2.25}Cl_{0.75}$	D (24)
	-109	14157	0.6782		$CH_3NH_3PbBr_{1.5}Cl_{1.5}$	C (55)
	-375	12255	0.5589		$CH_3NH_3PbBr_{0.75}Cl_{2.25}$	D (21)
Solid phase synthesis						
'$CH_3NH_3PbI_{1.5}Br_{1.5}$'	1126	25235	0.0000	93.4	$CH_3NH_3PbI_{2.1}Br_{0.9}$	D (30)
	997	24904	0.5342		$CH_3NH_3PbI_{1.8}Br_{1.2}$	C (40)
	872	27199	0.2117		$CH_3NH_3PbI_{1.5}Br_{1.5}$	D (30)
'$CH_3NH_3PbBr_{1.5}Cl_{1.5}$'	135	15111	1.0000	89.8	$CH_3NH_3PbBr_{2.25}Cl_{0.75}$	D (23)
	-112	13829	1.0000		$CH_3NH_3PbBr_{1.5}Cl_{1.5}$	C (62)
	-358	9806	0.0349		$CH_3NH_3PbBr_{0.75}Cl_{2.25}$	D (15)

[a]Hypothetical formulas calculated from synthetic loading alone. [b]Fitting parameters obtained from Bruker Topspin 3.0. [c]Actual compositional assignments determined from all experimental data combined. [d] Crystalline (C), amorphous (A), core/shell (c/s), dopant (D). [e]NMR peak integrations (n.d. = not determined). [f]Not the same batch; subtle differences during solution phase synthesis result in slightly different % values. [g]To 200 °C (see Methods).

^{207}Pb ssNMR: The number of scans for each sample were: $CH_3NH_3PbI_3$ (14483 (static) and 16255 (10 kHz)), *'$CH_3NH_3PbI_{1.5}Br_{1.5}$'* (34222 (static) and 40511 (10 kHz)), $CH_3NH_3PbBr_3$ (2375 (static) and 6144 (10 kHz)), *'$CH_3NH_3PbBr_{1.5}Cl_{1.5}$'* (23411 (static) and 27156 (10 kHz)), and $CH_3NH_3PbCl_3$ (6137 (static) and 1572 (10 kHz)). The chemical shift dispersion for *'$CH_3NH_3PbI_{1.5}Cl_{1.5}$'* was large, so both the static and 10 kHz spectrum consisted of two separate, overlapping spectra. The signal to noise ratio of the region corresponding to $CH_3NH_3PbI_3$ was improved by doubling the number of scans relative to the number of scans used for the $CH_3NH_3PbCl_3$ region and then dividing by 2 (static: 18266 $CH_3NH_3PbI_3$ region and 9133 $CH_3NH_3PbCl_3$ region, 10kHz: 16942 $CH_3NH_3PbI_3$ region and 8471 $CH_3NH_3PbCl_3$ region). The number of scans for *'$CH_3NH_3PbBr_{1.5}Cl_{1.5}$'* prepared by thermal annealing was 15820. The same *'$CH_3NH_3PbBr_{1.5}Cl_{1.5}$'* sample that was used for the 14.1 T measurements was used for the 9.4 T measurements (5712 scans). The *'$CH_3NH_3PbI_{1.5}Br_{1.5}$'* sample prepared by thermal annealing was analyzed on the 400 MHz NMR by stepping the transmitter frequency across the spectral region to obtain 2 spectra that were combined into one spectrum (4640 scans 900 ppm, 5888 scans 400 ppm). The number of scans for mixed-halide perovskite samples prepared by solid phase synthesis were: *'$CH_3NH_3PbI_{1.5}Br_{1.5}$'* (17270) and *'$CH_3NH_3PbBr_{1.5}Cl_{1.5}$'* (7953). Number of scans, echo delays and recycle delays for the pure perovskite data obtained on the 9.4 T (400 MHz) shown in Figure S4 are as follows. 50 kHz (all had a 40 μsecond echo delay): $CH_3NH_3PbI_3$ (16384 scans & 0.1 second delay), $CH_3NH_3PbBr_3$ (8192 scans & 0.156 second delay), and $CH_3NH_3PbCl_3$ (4096 scans & 1 second delay). Static: $CH_3NH_3PbI_3$ (16384 scans, 33.3 μsecond echo delay & 1.39 second delay), $CH_3NH_3PbBr_3$ (8192 scans, 20 μsecond echo delay & 2 second delay), and $CH_3NH_3PbCl_3$ (512 scans, 33.3 μsecond echo delay & 2.158 second delay).

References

(S1) Suits, B. H.; White, D. NMR Chemical Shifts and the Electronic Structure of Lead in Lead Halides. *J. Mag. Res.* **1989**, *82*, 441–453.

(S2) Dybowski, C.; Neue, G. Solid State ^{207}Pb NMR Spectroscopy. *Prog. NMR Spec.* **2002**, *41*, 153–170.

(S3) Dybowski, C.; Smith, M. L.; Hepp, M. A.; Gaffney, E. J.; Neue, G.; Perry, D. L. ^{207}Pb NMR Chemical-Shift Tensors of the Lead (II) Halides and the Lead (II) Hydroxyhalides. *App. Spec.* **1998**, *52*, 426–429.

(S4) Glatfelter, A.; Stephenson, N.; Bai, S.; Dybowski, C.; Perry, D. L. Quantitative Determination of Lead in Mixtures of Lead(II) Halides Using Solid-State ^{207}Pb NMR Spectroscopy. *Analyst* **2006**, *131*, 1207–1209.

(S5) Dmitrenko, O.; Bai, S.; Beckmann, P. A.; Van Bramer, S.; Vega, A.; Dybowski, C. The Relationship between ^{207}Pb NMR Chemical Shift and Solid-State Structure in Pb(II) Compounds. *J. Phys. Chem. A* **2008**, *112*, 3046–3052.

(S6) Taylor, R. E.; Beckmann, P. A.; Bai, S.; Dybowski, C. ^{127}I and ^{207}Pb Solid-State NMR Spectroscopy and Nuclear Spin Relaxation in PbI_2: A Preliminary Study. *J. Phys. Chem. C* **2014**, *118*, 9143.

CHAPTER 3

LEAD-FREE SEMICONDUCTORS: SOFT CHEMISTRY, DIMENSIONALITY CONTROL, AND MANGANESE-DOPING OF GERMANIUM HALIDE PEROVSKITES

Reprinted with permission from *ChemNanoMat* **2019**, *5*, 334–339

Long Men, Bryan A. Rosales, Noreen E. Gentry, Sarah D. Cady, and Javier Vela

Abstract

Lead halide perovskites have drawn enormous interest due to their exceptional photovoltaic and optoelectronic properties. However, the toxic heavy metal lead is harmful to humans and the environment resulting in a need for strategies to replace this toxic element. Herein, we report a facile aqueous synthesis of $CsGeX_3$ (X = I, Br) perovskite nanocrystals with size control achieved by varying the cysteammonium halide ligand concentration. We observe a variety of morphologies including pyramidal, hexagonal, and spheroidal. $CsGeX_3$ nanocrystals undergo a lattice expansion due to partial replacement of Cs^+ with larger cysteNH_3^+ cations into the lattice. We successfully dope Mn^{2+} into the $CsGeX_3$ lattice for the first time with incorporation up to 29% in bulk and 16% in nano samples. XRD peak shifts and EPR hyperfine splitting strongly indicate that Mn^{2+} is doped into the lattice. Our results introduce a new member to the lead-free halide perovskite family and set the fundamental stage for their use in optoelectronic devices.

Introduction

Halide perovskites of the general formula ABX_3 (A = methylammonium ($CH_3NH_3^+$), formamidinium ($CH(NH_2)_2^+$), guanidinium ($C(NH_2)_3^+$), Cs^+, Rb^+, or K^+; B = Pb^{2+}, Sn^{2+}, Ge^{2+}; X = I^-, Br^-, or Cl^-) are a re-emerging class of semiconductors that are under intense research due to their excellent optoelectronic properties, which are easily tunable by varying their elemental composition and structure.[1] Lead-based halide perovskites, in particular, demonstrate exceptional photovoltaic properties, having achieved a certified 23.3% power conversion efficiency for thin

films[2] in less than a decade of research,[3] and holding the current quantum dot solar cell record of 15.07%.[4] Lead halide perovskites are composed of Earth abundant elements and are easily processed from solution, leading to compatibility with roll-to-roll and other high-volume manufacturing techniques.[5] Nanocrystalline versions of these materials also exhibit long carrier lifetimes, tunable emission energies over the entire visible spectrum, and high quantum yields. This has led to further research into their photoluminescence properties,[6-10] as well as their use in light-emitting devices[11] and low-threshold lasers.[12-15]

Despite these wonderful properties, lead is a toxic heavy metal that is detrimental to the nervous and reproductive systems of humans and also raises concerns over environmental compatibility.[16-19] Intense research is ongoing to replace lead with other non-toxic, Earth-abundant elements.[20-28] Despite some of its compounds exhibiting residual toxicity, germanium is a comparatively benign replacement for lead in halide perovskites.[29-31] Germanium halide perovskites exhibit a corner-sharing $[GeI_6]^{4-}$ octahedral network similar to that observed in the lead halide perovskites. While $CsGeCl_3$ retains the classical cubic perovskite unit cell, both $CsGeBr_3$ and $CsGeI_3$ possess a rhombohedral distortion caused by a second-order Jahn-Teller effect (Figure 1).[32-34] This Jahn-Teller distortion results in octahedra containing two different Ge–X bonds, where three bonds are longer than the rest (Figure 1d).[40] Despite this lattice distortion and a large change in divalent metal ionic radii, the band gap values of germanium halide perovskites exhibit only minor differences when compared to those of the lead halide perovskites (see Supp. Info.). Moreover, $AGeX_3$ perovskites exhibit many beneficial properties such as direct band gaps[35-37] tunable between 1.6–3.7 eV,[36,38-40] strong absorption coefficients,[38,41-43] large dielectric constants,[44] small effective masses,[43] non-linear optical behavior,[45,46] strong ferroelectric polarization,[41] and a ns^2 electron configuration commonly found in defect tolerant semiconductors.[47] Surprisingly, even though they exhibit so many desirable properties, the synthesis of germanium halide perovskites is relatively unexplored compared to other lead-free halide perovskites, with only a few reports on photovoltaic devices[48-50] and one recently on nanocrystals.[51]

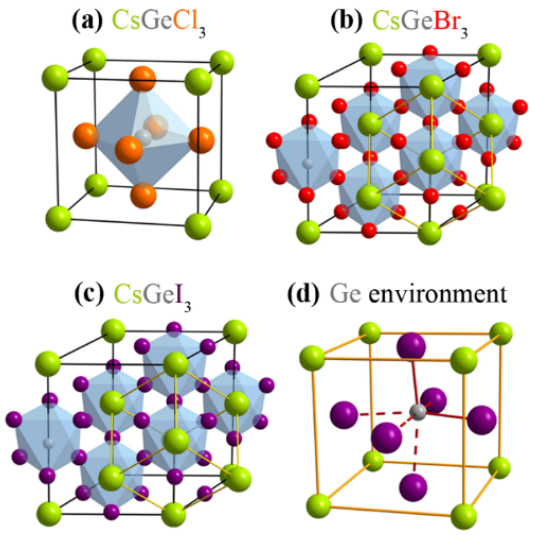

Figure 1. Unit cells of cesium germanium halide perovskites. $CsGeCl_3$ (a), $CsGeBr_3$ (b), $CsGeI_3$ (c). Rhombohedral distortion in $CsGeI_3$ and $CsGeBr_3$ (d).

Metal doping can expand the application of semiconductor nanocrystals by introducing new or modifying existing electronic, optical and magnetic properties.[52-55] Recently, significant research focused on doping metal halide perovskites with transition or main group metals.[56-58] Doping with up to 46% Mn^{2+} is currently possible,[59] leading to modified magnetic and optical properties.[60-64] Mn^{2+}-doping enhances stability,[65-67] increases quantum yield to 60%,[68] and results in long exciton lifetimes.[69,70] These enhanced properties are useful for LEDs[67,71] and solar cell downconverters.[72]

Herein, we report the synthesis and optical properties of $CsGeX_3$ (X = I, Br) nanocrystals with size control achieved by varying the ligand concentration. We demonstrate the first successful Mn^{2+}-doping into the germanium halide perovskite lattice. We observe systematic lattice expansion with increasing Mn^{2+} synthetic loading, which is consistent with larger Mn^{2+} ions replacing smaller Ge^{2+} in the lattice. These results present a leap forward in the synthesis of lead-free metal halide perovskites.

Results and discussion

Aqueous Nanocrystal Synthesis. We successfully prepared $CsGeX_3$ (X = I, Br) nanocrystals by introducing short-chain cysteammonium halide ($HSCH_2CH_2NH_3X$, $cysteNH_3X$) to a previously reported aqueous synthesis of bulk $CsGeI_3$[40] (Scheme 1). This synthesis employs GeO_2 and H_3PO_2

as Ge(IV) source and chemical reductant, respectively. Reaction of GeO_2 with HX produces GeX_4 as a partially soluble intermediate (see S.I.).[40] Reduction of the latter with H_3PO_2 produces highly soluble yellow form of Ge(II). In the absence of cysteNH$_3$X, this synthesis produces $CsGeX_3$ crystals with a size greater than 100 nm as determined from XRD peak widths using the Scherrer equation (Figure 2 and Table 1). Introducing cysteNH$_3$X at concentrations up to 2.50 M for $CsGeI_3$ and 3.33 M for $CsGeBr_3$ reduces the Scherrer size to 26±2 nm and 50±5 nm, respectively. CysteNH$_3$X concentrations beyond these values and attempts to synthesize $CsGeCl_3$ did not yield a precipitate (see Experimental).

Table 1. Synthesis of $CsGeX_3$ (X = I, Br) Nanocrystals.[a]

Compound	[Ligand] (M)	XRD Size (nm)[b]	TEM Size (nm)	E_g (eV)[c]
$CsGeI_3$	0	>100	50–500μm[d]	1.61
	0.05	78±4	-	1.62
	0.50	63±12	79±26	1.64
	2.50	26±2	34±8	1.66
$CsGeBr_3$	0	>100	-	2.37
	0.67	89±19	-	2.41
	3.33	50±5	53±10	2.41

[a][Ge^+] = [Cs^+] = 0.05 M for all reactions. [b]Scherrer equation. [c]From Tauc plots. [d]From SEM.

Scheme 1. Synthesis of $CsGeX_3$ Nanocrystals.

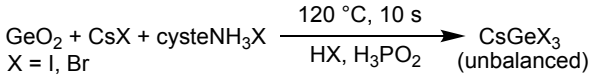

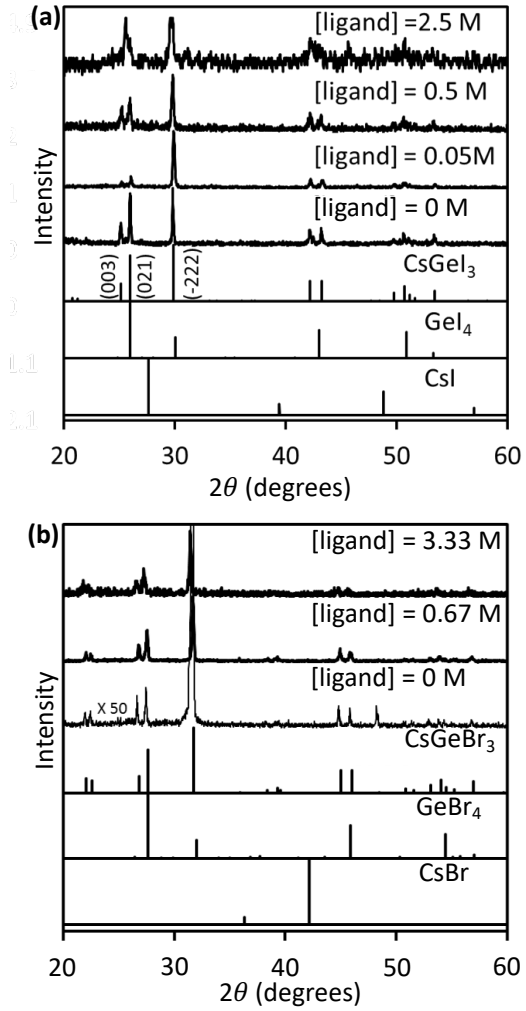

Figure 2. Powder XRD patterns of $CsGeI_3$ (a) and $CsGeBr_3$ (b) nanocrystals synthesized with different $cysteNH_3X$ concentrations.

We characterized the size, morphology, and elemental composition of $CsGeX_3$ nanocrystals by scanning and transmission electron microscopy (SEM and TEM). SEM analysis of samples grown in the absence of $cysteNH_3X$ show large 50–500 μm microcrystals with various morphologies (Figure 3). In agreement with XRD, TEM shows that introducing $cysteNH_3X$ at concentrations up to 2.50 M for $CsGeI_3$ and 3.33 M for $CsGeBr_3$ decreases and narrows their size distributions to 34±8 nm and 53±10 nm, respectively. Morphologies range from pyramidal and

hexagonal for $CsGeI_3$ to spheroidal for $CsGeBr_3$ nanocrystals. Selected area electron diffraction (SAED) analysis is consistent with the rhombohedral structure of $CsGeI_3$ nanocrystals. Energy dispersive X-ray spectroscopy (EDS) confirms the presence of all three elements with atomic percentages of 15±1% for Cs, 27±2% for Ge and 57±1% for I, roughly consistent with a Cs:Ge:I ratio of 1:1.8:3.8. High-resolution TEM shows lattice fringes with a d spacing of 3.425 Å, which is consistent with the (021) lattice planes of $CsGeI_3$.

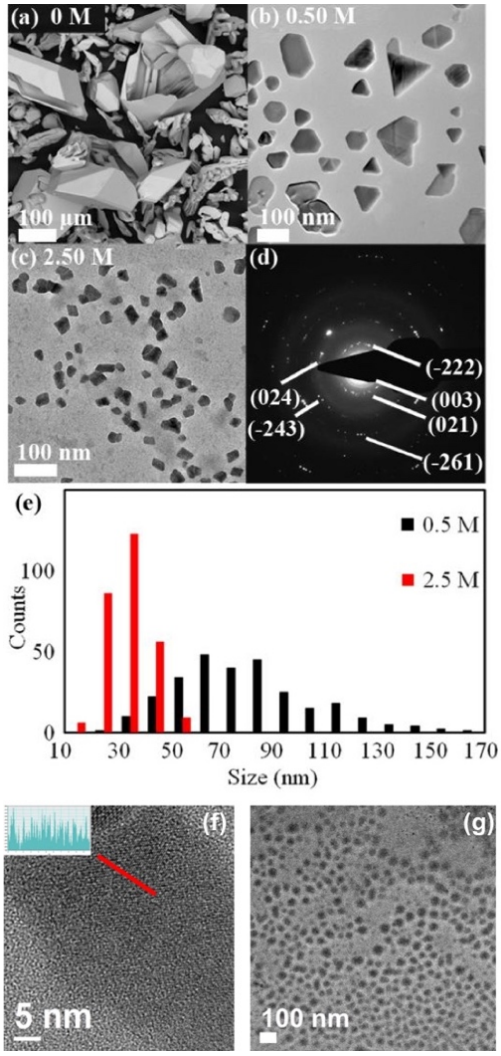

Figure 3. Representative SEM (a), TEM (b-c), and size distribution histograms (e) of $CsGeI_3$ synthesized with different cysteNH$_3$X concentrations. SAED (d) of $CsGeI_3$ synthesized with [cysteNH$_3$X] = 0.5 M. HRTEM image (f) of a $CsGeI_3$ nanocrystal showing lattice fringes along the (021) direction. TEM (g) of $CsGeBr_3$ synthesized with [cysteNH$_3$X] = 3.33 M.

Optical Properties. Diffuse reflectance measurements and Tauc plots show that the band gap of $CsGeI_3$ nanocrystals shifts from 1.61 eV to 1.66 eV as the cysteNH$_3$X concentration increases, while $CsGeBr_3$ nanocrystals maintain a band gap of 2.41 eV (Figure 4). We considered a couple possibilities that could explain the band gap shift observed in the $CsGeI_3$ case, namely: quantum confinement or ion replacement. To determine whether the observed change in band gap was caused by quantum confinement, we estimated the effective excitonic Bohr radius of $CsGeI_3$ nanocrystals. In effective mass theory,[73] the effective Bohr radius of a Wannier-Mott exciton can be determined from $a^* = 2a_0\varepsilon^{\infty}(\frac{m_0}{m_e} + \frac{m_0}{m_h})$, where the hydrogen Bohr radius is $a_0 = 0.0529$ nm, the effective dielectric constant is $\varepsilon^{\infty} = 5.0$, the electron-hole reduced effective masses are $m_h/m_0 = 0.2$, and $m_e/m_0 = 0.4$ (Z → L) or 0.2 (Z → Γ).[74] Using these values, we estimated the effective Bohr radius to be 4–5 nm. However, because our smallest crystal size (34±8 nm) is larger than the estimated Bohr radius (4–5 nm), it is unlikely that the observed band gap change is caused by quantum confinement. Therefore, we conclude that the most likely explanation for the slight change in band gap observed for $CsGeI_3$ stems from partial replacement of Cs^+ by cysteNH$_3^+$ cations. Based on crystallographic data available,[75] we estimate the size of the cysteNH$_3^+$ cation to be 283 pm, which is comparable to the size of very commonly incorporated guanidinium ($C(NH_2)_3^+$, 274 pm) cation.[76]

In contrast to recently reported carboxylate-capped $CsGeI_3$ nanocrystals,[51] $CsGeI_3$ nanocrystals prepared by our method unfortunately do not exhibit photoluminescence (PL) emission. However, $CsGeBr_3$ nanocrystals exhibit a weak PL peak at 500 nm, whose intensity increases with the introduction of cysteNH$_3$X, with a highest quantum yield of 0.34%.

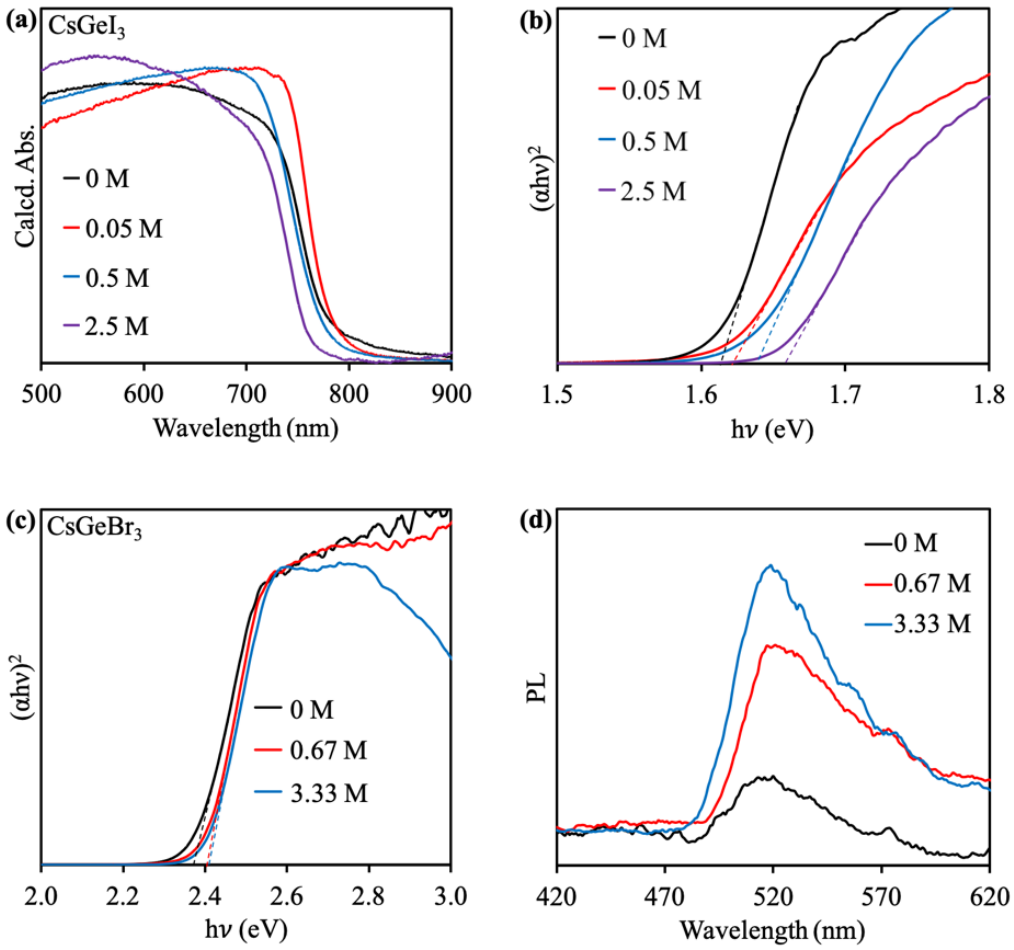

Figure 4. Diffuse reflectance spectra (a) and Tauc plots (b) of $CsGeI_3$ nanocrystals. Tauc plots (c) and PL spectra (d) of $CsGeBr_3$ nanocrystals synthesized with different cysteNH_3X concentrations (λ_{exc} = 350 nm).

Manganese Doping. We successfully incorporate Mn^{2+} into the $CsGeX_3$ (X = I, Br) lattice by introducing MnO or MnX_2 at the beginning of the reaction (Scheme 2, see below). Mn^{2+}-doped samples exhibit similar optical properties and morphologies as undoped $CsGeX_3$. This observation is consistent with Mn^{2+}-doped $CsPbI_3$ and $CsPbBr_3$ nanocrystals.[57,65,77] Tauc plots show that all absorption edges appear around 1.6 eV, indicating that Mn^{2+} doping has a limited effect on the electronic structure of $CsGeX_3$. No photoluminescence is observed from Mn^{2+} dopants because the $CsGeX_3$ band gaps are lower than the Mn^{2+} emission energies.[65,77]

Powder XRD shows that the $CsGeX_3$ structure is maintained across different synthetic Mn^{2+} loadings. XRD peaks of Mn^{2+}-doped bulk and nano $CsGeX_3$ samples, calibrated to Si as an internal standard are slightly shifted to lower angles with increased synthetic Mn^{2+} loading (Figure

5 and S.I.). The small XRD peak shifts are consistent with reports of Mn^{2+} doping into $CsPbX_3$ even at high doping levels.[57,65,78] The shift to lower 2θ angles is consistent with lattice expansion due to 6-coordinate replacement of Ge^{2+} ion (87 pm) with the larger high-spin Mn^{2+} ion (97 pm, see below).[79] X-band EPR spectra of Mn^{2+}-doped bulk and nano $CsGeX_3$ at 10 K exhibit a sextet hyperfine signal that confirms the presence of isolated high-spin Mn^{2+} ions (Figure 6).[57] Mn^{2+} ions occupying a rhombohedrally-distorted site cause extra splitting of this sextet hyperfine signal with additional weaker splittings observed outside the central +1/2 → -1/2 transition.[80] However, in cases where the complex is nearly octahedral, only the central +1/2 → -1/2 transition is observed.[80] We do not observe these extra weaker transitions in our spectra, likely because the rhombohedral distortion in germanium halide perovskites is relatively small (in fact, $CsGeCl_3$ is completely cubic). However, our observed extra splitting of the +1/2 → -1/2 transitions is consistent with a rhombohedral distortion and strongly indicates that Mn^{2+} is doped into the germanium halide perovskite lattice.[80] Interestingly, a similar observation is observed for Mn^{2+}-doped $CsPbCl_3$ at low temperatures that induce phase transitions to lower symmetry structures.[81] The hyperfine splitting constants of 90–96 G are larger than the 86–87 G values recently observed for Mn^{2+}-doped $CsPbCl_3$,[60,63,64,66,78,81,82] which is consistent with the higher lattice ionicity of germanium halide perovskites.[83]

Considering Vegard's Law, [84,85] we estimate we can incorporate Mn^{2+} ions up to 29% in bulk—and up to 16% in nanocrystalline samples—(Figure 5). Here, we note that the lattice parameter of undoped nano $CsGeX_3$ is slightly larger than that of undoped bulk $CsGeX_3$. As noted above, this lattice expansion is likely caused by partial replacement of Cs^+ (181 pm)[79] with larger cysteNH$_3^+$ (274 pm) cations into the lattice. In all cases, the actual Mn^{2+} incorporation is lower than the synthetic Mn^{2+} loading, which indicates that Ge^{2+} is preferentially incorporated into the $CsGeX_3$ lattice. This is consistent with previous reports on Mn^{2+}-doped $CsPbX_3$ nanocrystals, whose fast nucleation kinetics[86] reduces Mn^{2+} incorporation.[59-61,63,65,68] Interestingly, the chemical yield systematically decreases with increasing synthetic Mn^{2+} loading, likely because the parent $CsMnX_3$ compound is too soluble in water and fails to precipitate (see S.I.).[87]

Scheme 2. Manganese Doping of $CsGeX_3$.

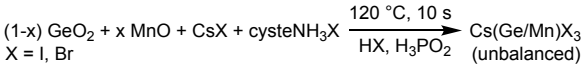

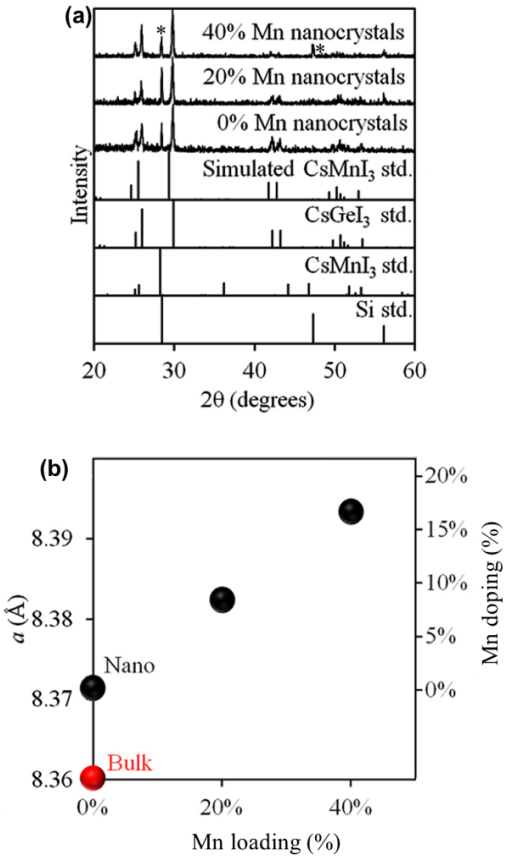

Figure 5. Powder XRD patterns (a) of Mn^{2+}-doped $CsGeI_3$ nanocrystals synthesized with [cysteNH$_3$X] = 0.50 M and different synthetic Mn^{2+} loading. Asterisks (*) denote silicon powder used as an internal standard. Shift in lattice parameter as a function of synthetic Mn^{2+} loading (b).

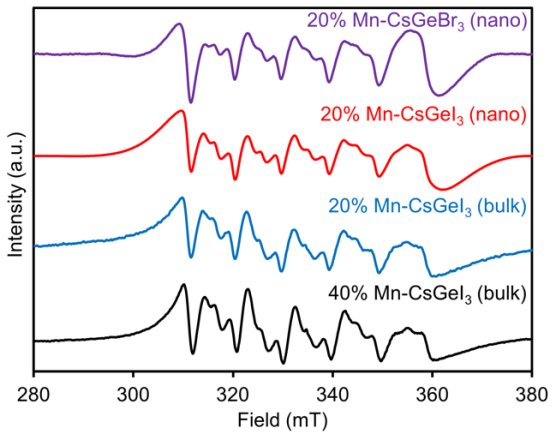

Figure 6. X-band EPR spectra of Mn^{2+}-doped $CsGeX_3$ collected at 10 K.

Conclusions

Concerns over the toxicity of lead towards the human nervous and reproductive systems as well as the environment have led to intense research aimed at replacing this toxic heavy metal with other elements. We report a facile aqueous synthesis of $CsGeX_3$ (X = I, Br) nanocrystals that are size tunable as low as 34±8 nm for $CsGeI_3$ and 53±10 nm for $CsGeBr_3$, specifically by varying the cysteammonium halide ligand concentration. The structure of these nanocrystals undergoes lattice expansion compared to their bulk counterparts, due to partial replacement of Cs^+ with the larger $cysteNH_3^+$ cation. Based on the calculated Bohr radius of $CsGeI_3$, we attribute a small observed band gap increase not to quantum confinement, but rather to $cysteNH_3^+$ incorporation. TEM shows that nanocrystal morphologies range from pyramidal and hexagonal for $CsGeI_3$ to spheroidal for $CsGeBr_3$.

We report here the first successful Mn^{2+}-doping of germanium halide perovskites. XRD peak shifts and EPR hyperfine splitting strongly indicate that Mn^{2+} is doped into the lattice with an incorporation of up to 29% in bulk and 16% in nanocrystalline samples. Mn^{2+}-doping seems to have a limited effect on the optical properties of $CsGeX_3$, which is consistent with similar reports on $CsPbX_3$ compounds. We believe that the results reported here will help advance the fundamental study of lead-free perovskites and move toward their application to optoelectronic devices.

Methods

Materials. Germanium(IV) oxide (≥99.99%), cesium iodide (99.999%), hydriodic acid (ACS, 55%), hydrobromic acid (ACS, 48%) and cysteamine (95%) were purchased from Sigma-Aldrich; cesium bromide (99.9%-Cs), manganese(II) oxide (99%), manganese(II) iodide (98+%) and silicon powder (99+%) from Strem; hypophosphorous acid (50% w/w aqueous solution) from Alfa Aesar. All chemicals used as received.

Synthesis. *Cysteammonium Halide ($CysteNH_3X$) Stock Solution.* Cysteamine (771 mg, 10 mmol) was mixed with hydrohalic acid solution (1.4 mL, 7.3 M for HI or 1.4 mL, 8.8 M for HBr). *Synthesis without Added Ligands.* Cesium germanium halide perovskites were prepared by a slightly modified literature procedure.[40] Briefly, germanium(IV) oxide (10.5 mg, 0.1 mmol), hydrohalic acid (0.7 mL of 7.3 M HI or 0.6 mL of 8.8 M HBr), and hypophosphorous acid (0.25 mL of 9.1 M) were stirred at 120 °C until the mixture became homogeneous. Cesium halide (0.3

mL of 0.3 M in ultrapure water) was injected at 120 °C and then the solution was immediately cooled to 0 °C using an ice-water bath until black ($CsGeI_3$) or orange ($CsGeBr_3$) precipitate was formed. The precipitate was collected by centrifugation for 5 min at 4500 rpm then kept under an inert atmosphere to prevent oxidation of Ge^{2+}.[40] *Germanium Halide Perovskite Nanocrystals*. Samples were prepared as above except cysteammonium halide stock solution (0.2 mL, 7.3 M) was added initially with other reagents. Addition of cysteammonium causes the formation of an orange precipitate that re-dissolves upon addition of cesium halide. *Manganese Doping.* Samples were prepared as above except germanium(IV) oxide was partially replaced with the desired synthetic loading of manganese oxide or halide.

Structural Characterization. *Powder X-ray diffraction* (XRD) data were measured using Cu Kα radiation on a Rigaku Ultima IV (40 kV, 44 mA) instrument with samples deposited on a "background-less" quartz slide. *Transmission electron microscopy* (TEM) images were collected on an FEI Tecnai G2 F20 field emission microscope operating up to 200 kV with a point-to-point resolution of less than 0.25 nm and a line-to-line resolution of less than 0.10 nm. Dilute sample solutions in toluene were dropped onto carbon-coated copper grids. Elemental composition was assessed by energy-dispersive spectroscopy (EDS). Size histograms were generated by measuring the longest edge of more than 300 crystals per trace.

Optical Characterization. *Diffuse reflectance* spectra of solid films were measured with a SL1 Tungsten Halogen lamp (vis-IR), a SL3 Deuterium Lamp (UV), and a BLACK-Comet C-SR-100 Spectrometer. Samples were prepared by drop-casting toluene solutions onto glass. *Steady-state photoluminescence* (PL) spectra were measured with a Horiba-Jobin Yvon Nanolog scanning spectrofluorometer equipped with a photomultiplier detector. Relative PL quantum yields (QYs) were measured against the Coumarin 460 dye using standard procedures.

Other Characterization. *Electron Paramagnetic Resonance* (EPR) spectra were measured using an ELEXYS E580 EPR Spectrometer (Bruker BioSpin) equipped with an SHQE resonator and an Oxford ESR900 cryostat at a temperature of 10 K. The samples were dispersed in ethanol, placed in a 4 mm quartz tube, and frozen in liquid N_2 prior to insertion into the cryostat. Typical spectra were acquired with a sweep width of 5000 G, 2048 points, 8 G amplitude modulation, and 1.986 mW microwave power. Simulations were performed using the "pepper" function of the computational package EasySpin that operates in MATLAB.

Acknowledgements

J.V. and B.A.R. thank the U.S. National Science Foundation for a CAREER Grant and an AGEP GR Supplement, respectively, from the Division of Chemistry, Macro- molecular, Supramolecular, and Nanochemistry Program (#1253058). Electron microscopy was performed at the Sensitive Instrument Facility of the Ames Laboratory, which is operated for the U.S. Department of Energy by Iowa State University under contract #DE-AC02-07CH11358.

References

(1) Li, W.; Wang, Z.; Deschler, F.; Gao, S.; Friend, R. H.; Cheetham, A. K. Chemically Diverse and Multifunctional Hybrid Organic-Inorganic Perovskites. *Nat. Rev. Mater.* **2017**, *2*, 16099.

(2) National Renewable Energy Laboratory. Best Research-Cell Efficiencies Chart. https://www.nrel.gov/pv/assets/images/efficiency_chart.jpg (accessed on October 7, 2018).

(3) Green, M. A.; Ho-Bailli, A. Perovskite Solar Cells: The Birth of a New Era in Photovoltaics. *ACS Energy Lett.* **2017**, *2*, 822–830.

(4) Wang, K.; Jin, Z.; Liang, L.; Bian, H.; Bai, D.; Wang, H.; Zhang, J.; Wang, Q.; Liu, S. All-Inorganic Cesium Lead Iodide Perovskite Solar Cells with Stabilized Efficiency Beyond 15%. *Nat. Commun.* **2018**, *9*, 4544.

(5) Li, Z.; Klein, T. R.; Kim, D. H.; Yang, M.; Berry, J. J.; van Hest, M. F. A. M.; Zhu, K. Scalable Fabrication of Perovskite Solar Cells. *Nat. Rev. Mater.* **2018**, *3*, 18017.

(6) Zhang, F.; Zhong, H.; Chen, C.; Wu, X.-g.; Hu, X.; Huang, H.; Han, J.; Zou, B.; Dong, Y. Brightly Luminescent and Color-Tunable Colloidal $CH_3NH_3PbX_3$ (X = Br, I, Cl) Quantum Dots: Potential Alternatives for Display Technology. *ACS Nano* **2015,** *9*, 4533–4542.

(7) Protesescu, L.; Yakunin, S.; Bodnarchuk, M. I.; Krieg, F.; Caputo, R.; Hendon, C. H.; Yang, R. X.; Walsh, A.; Kovalenko, M. V. Nanocrystals of Cesium Lead Halide Perovskites ($CsPbX_3$,

X= Cl, Br, and I): Novel Optoelectronic Materials Showing Bright Emission with Wide Color Gamut. *Nano Lett.* **2015**, *15*, 3692–3696.

(8) Luo, L.; Men, L.; Liu, Z.; Mudryk, Y.; Zhao, X.; Yao, Y.; Park, J. M.; Shinar, R.; Shinar, J.; Ho, K.-M.; Perakis, I. E.; Vela, J.; Wang, J. Ultrafast Terahertz Snapshots of Excitonic Rydberg States and Electronic Coherence in an Organometal Halide Perovskite. *Nat. Commun.* **2017**, *8*, 15565.

(9) Zhu, F.; Men, L.; Guo, Y.; Zhu, Q.; Bhattacharjee, U.; Goodwin, P. M.; Petrich, J. W.; Smith, E. A.; Vela, J. Shape Evolution and Single Particle Luminescence of Organometal Halide Perovskite Nanocrystals. *ACS Nano* **2015**, *9*, 2948–2959.

(10) Rosales, B. A.; Hanrahan, M. P.; Boote, B. W.; Rossini, A. J.; Smith, E. A.; Vela, J. Lead Halide Perovskites: Challenges and Opportunities in Advanced Synthesis and Spectroscopy. *ACS Energy Lett.* **2017**, *2*, 906–914.

(11) Sutherland, B. R.; Sargent, E. H. Perovskite Photonic Sources. *Nat. Photon.* **2016**, *10*, 295–302.

(12) Zhu, H.; Fu, Y.; Meng, F.; Wu, X.; Gong, Z.; Ding, Q.; Gustafsson, M.V.; Trinh, M.T.; Jin, S.; Zhu, X.Y. Lead Halide Perovskite Nanowire Lasers with Low Lasing Thresholds and High Quality Factors. *Nat. Mater.* **2015**, *14*, 636–642.

(13) Wang, Y.; Li, X.; Zhao, X.; Xiao, L.; Zeng, H.; Sun, H. Nonlinear Absorption and Low-Threshold Multiphoton Pumped Stimulated Emission from All-Inorganic Perovskite Nanocrystals. *Nano Lett.* **2016**, *16*, 448–453.

(14) Yakunin, S.; Protesescu, L.; Krieg, F.; Bodnarchuk, M. I.; Nedelcu, G.; Humer, M.; De Luca, G.; Fiebig, M.; Heiss, W.; Kovalenko, M. V. Low-Threshold Amplified Spontaneous Emission and Lasing from Colloidal Nanocrystals of Caesium Lead Halide Perovskites. *Nat. Comm.* **2015**, *6*, 8056.

(15) Pan, J.; Sarmah, S. P.; Murali, B.; Dursun, I.; Peng, W.; Parida, M. R.; Liu, J.; Sinatra, L.; Alyami, N.; Zhao, C.; Alarousu, E.; Ng, T. K.; Ooi, B. S.; Bakr, O. M.; Mohammed, O. F. Air-Stable Surface-Passivated Perovskite Quantum Dots for Ultra-Robust, Single- and Two-Photon-Induced Amplified Spontaneous Emission. *J. Phys. Chem. Lett.* **2015**, *6*, 5027–5033.

(16) Gidlow, D. A. Lead Toxicity. *Occup. Med.* **2015**, *65*, 348–356.

(17) Gidlow, D. A. Lead Toxicity. *Occup. Med.* **2004**, *52*, 76–81.

(18) Babayigit, A; Ethirajan, A.; Muller, M.; Conings, B. Toxicity of Organometal Halide Perovskite Solar Cells. *Nat. Mater*. **2016**, *15*, 247–251.

(19) Serrano-Lujan, L.; Espinosa, N.; Larsen-Olsen, T. T.; Abad, J.; Urbina, A.; Krebs, F. C. Tin- and Lead-Based Perovskite Solar Cells under Scrutiny: An Environmental Perspective. *Adv. Energy Mater.* **2015**, *5*, 1501119.

(20) Rosales, B. A.; White, M. A.; Vela, J. Solution-Grown Sodium Bismuth Dichalcogenides: Toward Earth-Abundance, Biocompatible Semiconductors. *J. Am. Chem. Soc.* **2018**, *140*, 3736–3742.

(21) Reiss, P.; Carrière, M.; Lincheneau, C.; Vaure, L.; Tamang, S. Synthesis of Semiconductor Nanocrystals, Focusing on Nontoxic and Earth-Abundant Materials. *Chem. Rev.* **2016**, *116*, 10731–10819.

(22) Zhu, F.; Gentry, N. E.; Men, L.; White, M. A.; Vela, J. Aliovalent Doping of Lead Halide Perovskites: Exploring the $CH_3NH_3PbI_3$-$(CH_3NH_3)_3Sb_2I_9$ Nanocrystalline Phase Space. *J. Phys. Chem. C* **2018**, *122*, 25, 14082–14090.

(23) Pazoki, M.; Edvinsson, T. Metal Replacement in Perovskite Solar Cell Materials: Chemical Bonding Effects and Optoelectronic Properties. *Sustain. Energy Fuels* **2018**, *2*, 1430–1445.

(24) Liang, L.; Gao, P. Lead-Free Hybrid Perovskite Absorbers for Viable Application: Can We Eat the Cake and Have It Too? *Adv. Sci.* **2018**, *5*, 1700331.

(25) Shi, Z.; Guo, J.; Chen, Y.; Li, Q.; Pan, Y.; Zhang, H.; Xia, Y.; Huang, W. Lead-Free Organic-Inorganic Hybrid Perovskites for Photovoltaic Applications: Recent Advances and Perspectives. *Adv. Mater.* **2017**, *29*, 1605005.

(26) Lyu, M.; Yun, J.-H.; Chen, P.; Hao, M.; Wang, L. Addressing Toxicity of Lead: Progress and Applications of Low-Toxic Metal Halide Perovskites and Their Derivatives. *Adv. Energy Mater.* **2017**, *7*, 1602512.

(27) Hu, H.; Dong, B.; Zhang, W. Low-Toxic Metal Halide Perovskites: Opportunities and Future Challenges. *J. Mater. Chem. A* **2017**, *5*, 11436–11449.

(28) Slavney, A. H.; Smaha, R. W.; Smith, I. C.; Jaffe, A.; Umeyama, D.; Karunadasa, H. I. Chemical Approaches to Addressing the Instability and Toxicity of Lead-Halide Perovskite Absorbers. *Inorg. Chem.* **2017**, *56*, 46–55.

(29) Yokoi K. (2013) Germanium, Toxicity. In: Kretsinger R.H., Uversky V.N., Permyakov E.A. (eds) Encyclopedia of Metalloproteins. Springer, New York, NY.

(30) Gerber, G. B.; Léonard, A. Mutagenicity, Carcinogenicity and Teratogenicity of Germanium Compounds. *Mutat. Res*., **1997**, *387*, 141–146.

(31) Kanisawa, M.; Schroeder, H. A. Life Term Studies on the Effect of Trace Elements on Spontaneous Tumors in Mice and Rats. *Cancer Res.* **1969**, *29*, 892–895.

(32) Goesten, M. G.; Hoffman, R. Mirrors of Bonding in Metal Halide Perovskites. *J. Am. Chem. Soc.* **2018**, *140*, 40, 12996–13010.

(33) Seo, D. K.; Gupta, N.; Whangbo, M. H.; Hillebrecht, H.; Thiele, G. Pressure-Induced Changes in the Structure and Band Gap of $CsGeX_3$ (X = Cl, Br) Studied by Electronic Band Structure Calculations. *Inorg. Chem.* **1998**, *37*, 407–410.

(34) Tang, L. C.; Huang, J. Y.; Chang, C. S.; Lee, M. H.; Liu, L. Q. New Infrared Nonlinear Optical Crystal $CsGeBr_3$: Synthesis, Structure and Powder Second-Harmonic Generation Properties. *J. Phys. Condens. Matter* **2005**, *17*, 7275–7286.

(35) Ray, D.; Clark, C.; Pham, H. Q.; Borycz, J.; Holmes, R. J.; Aydil, E. S.; Gagliardi, L. Computational Study of Structural and Electronic Properties of Lead-Free $CsMI_3$ Perovskites (M = Ge, Sn, Pb, Mg, Ca, Sr, and Ba). *J. Phys. Chem. C* **2018**, *122*, 7838–7848.

(36) Huang, L. Y.; Lambrecht, W. R. Electronic Band Structure Trends of Perovskite Halides: Beyond Pb and Sn to Ge and Si. *Phys. Rev. B* **2016**, *93*, 195211.

(37) Jiang, L.; Wu, T.; Sun, L.; Li, Y.-J.; Li, A.-L.; Lu, R.-F.; Zou, K.; Deng, W.-Q. First-Principles Screening of Lead-Free Methylammonium Metal Iodine Perovskites for Photovoltaic Application. *J. Phys. Chem. C* **2017**, *121*, 24359–24364.

(38) Sun, P. P.; Li, Q. S.; Yang, L. N.; Li, Z. S. Theoretical Insights into a Potential Lead-Free Hybrid Perovskite: Substituting Pb^{2+} with Ge^{2+}. *Nanoscale*, **2016**, *8*, 1503–1512.

(39) Zhao, Y.-Q.; Wang, X.; Liu, B.; Yu, Z.-L.; He, P.-B.; Wan, Q.; Cai, M.-Q.; Yu, H.-L. Geometric Structure and Photovoltaic Properties of Mixed Halide Germanium Perovskites from Theoretical View. *Org. Electron.* **2018**, *53*, 50–56.

(40) Stoumpos, C. C.; Frazer, L.; Clark, D. J.; Kim, Y. S.; Rhim, S. H.; Freeman, A. J.; Ketterson, J. B.; Jang, J. I.; Kanatzidis, M. G. Hybrid Germanium Iodide Perovskite Semiconductors: Active Lone Pairs, Structural Distortions, Direct and Indirect Energy Gaps, and Strong Nonlinear Optical Properties. *J. Am. Chem. Soc.* **2015**, 137, 6804–6819.

(41) Zhao, Y.-Q.; Liu, B.; Yu, Z.-L.; Ma, J.; Wan, Q.; He, P.-B.; Cai, M.-Q. Strong Ferroelectric Polarization of $CH_3NH_3GeI_3$ with High-Absorption and Mobility Transport Anisotropy: Theoretical Study. *J. Mater. Chem. C* **2017**, *5*, 5356–5364.

(42) Roknuzzaman, M.; Ostrikov, K.; Wang, H.; Du, A.; Tesfmichael, T. Towards Lead-Free Perovskite Photovoltaics and Optoelectronics by *Ab-Initio* Simulations. *Sci. Rep.* **2017**, *7*, 14025.

(43) Qian, J.; Zu, B.; Tian, W. A Comprehensive Theoretical Study of Halide Perovskites ABX_3. *Org. Electron.* **2016**, *37*, 61–73.

(44) Ming, W. M.; Shi, H. L.; Du, M. H. Large Dielectric Constant, High Acceptor Density, and Deep Electron Traps in Perovskite Solar Cell Material $CsGeI_3$. *J. Mater. Chem. A* **2016**, *4*, 13852–13858.

(45) Tang, L. C.; Chang, Y. C.; Huang, J. Y.; Lee, M. H.; Chang, C. S. First Principles Calculations of Linear and Second-Order Optical Responses in Rhombohedrally Distorted Perovskite Ternary Halides, $CsGeX_3$ (X = Cl, Br, and I). *Jpn. J. Appl. Phys.* **2009**, *48*, 112402.

(46) Walters, G.; Sargent, E. H. Electro-Optic Response in Germanium Halide Perovskites. *J. Phys. Chem. Lett.* **2018**, *9*, 1018–1027.

(47) Ganose, A. M.; Savory, C. N.; Scanlon, D. O. Beyond Methylammonium Lead Iodide: Prospects for the Emergent Field of ns^2 Containing Solar Absorbers. *Chem. Commun.* **2017**, *53*, 20–44.

(48) Kopacic, I.; Friesenbichler, B.; Hoefler, S. F.; Kunert, B.; Plank, H.; Rath, T.; Trimmel, G. Enhanced Performance of Germanium Halide Perovskite Solar Cells Through Compositional Engineering. *ACS Appl. Energy Mater.* **2018**, *1*, 343–347.

(49) Cheng, P.; Wu, T.; Zhang, J.; Li, Y.; Liu, J.; Jiang, L.; Mao, X.; Lu, R.-F.; Deng, W.-Q.; Han, K. $(C_6H_5C_2H_4NH_3)_2GeI_4$: A Layered Two-Dimensional Perovskite with Potential for Photovoltaic Applications. *J. Phys. Chem. Lett.* **2017**, *8*, 4402–4406.

(50) Krishnamoorthy, T.; Ding, H.; Yan, C.; Leong, W. L.; Baikie, T.; Zhang, Z.; Sherburne, M.; Li, S.; Asta, M.; Mathews, N.; Mhaisalkar, S. G. Lead-Free Germanium Iodide Perovskite Materials for Photovoltaic Applications. *J. Mater. Chem. A* **2015**, *3*, 23829–23832.

(51) Wu, X.; Song, W.; Li, Q.; Zhao, X.; He, D.; Quan, Z. Synthesis of Lead-Free $CsGeI_3$ Perovskite Colloidal Nanocrystals and Electron Beam-Induced Transformations. *Chem. Asian J.* **2018**, *13*, 1654–1659.

(52) Norris, D. J.; Efros, A. L.; Erwin, S. C. Doped Nanocrystals. *Science* **2008**, *319*, 1776–1779.

(53) Erwin, S. C.; Zu, L.; Haftel, M. I.; Efros, A. L. Doping Semiconductor Nanocrystals. *Nature* **2005**, *436*, 91–94.

(54) Buonsanti, R.; Milliron, D. J. Chemistry of Doped Colloidal Nanocrystals. *Chem. Mater.* **2013**, *25*, 1305–1317.

(55) Beaulac, R.; Archer, P. I.; Ochsenbein, S. T.; Gamelin, D. R. Mn^{2+}-Doped CdSe Quantum Dots: New Inorganic Materials for Spin-Electronics and Spin-Photonics. *Adv. Funct. Mater.* **2008**. *18*, 3873–3891.

(56) Zhou, Y.; Chen, J.; Bakr, O. M.; Sun, H.-T.; Metal-Doped Lead Halide Perovskites: Synthesis, Properties, and Optoelectronic Applications. *Chem. Mater.* **2018**, 30, 19, 6589–6613.

(57) Swarnkar, A.; Ravi, V. K.; Nag, Angshuman. Beyond Colloidal Cesium Lead Halide Perovskite Nanocrystals: Analogous Metal Halides and Doping. *ACS Energy Lett.* **2017**, *2*, 1089–1098.

(58) Guria, A. K.; Dutta, S. K.; Adhikari, S. D.; Pradhan, N. Doping Mn^{2+} in Lead Halide Perovskite Nanocrystals: Successes and Challenges. *ACS Energy Lett.* **2017**, *2*, 1014–1021.

(59) Liu, H.; Wu, Z.; Shao, J.; Yao, D.; Gao, H.; Liu, Y.; Yu, W.; Zhang, H.; Yang, B. $CsPb_xMn_{1-x}Cl_3$ Perovskite Quantum Dots with High Mn Substitution Ratio. *ACS Nano* **2017**, *11*, 2239–2247.

(60) Parobek, D.; Roman, B. J.; Dong, Y. T.; Jin, H.; Lee, E.; Sheldon, M.; Son, D. H. Exciton-to-Dopant Energy Transfer in Mn-Doped Cesium Lead Halide Perovskite Nanocrystals. *Nano Lett.* **2016,** 16, 7376–7380.

(61) Parobek, D.; Dong, Y.; Quao, T.; Son, D. H. Direct Hot-Injection Synthesis of Mn-Doped $CsPbBr_3$ Nanocrystals. *Chem. Mater.* **2018**, *30*, 2939–2944.

(62) Liu, W. Y.; Lin, Q. L.; Li, H. B.; Wu, K. F.; Robel, I.; Pietryga, J. M.; Klimov, V. I. Mn^{2+}-Doped Lead Halide Perovskite Nanocrystals with Dual-Color Emission Controlled by Halide Content. *J. Am. Chem. Soc.* **2016,** 138, 14954–14961.

(63) Mir, W. J.; Jagadeeswararao, M.; Das, S.; Nag, A. Colloidal Mn-Doped Cesium Lead Halide Perovskite Nanoplatelets. *ACS Energy Lett.* **2017**, *2*, 537–543.

(64) De, A.; Mondal, N.; Samanta, A. Luminescence Tuning and Exciton Dynamics of Mn-Doped $CsPbCl_3$ Nanocrystals. *Nanoscale* **2017**, *9*, 16722–16727.

(65) Akkerman, Q. A.; Meggiolaro, D.; Dang, Z.; De Angelis, F.; Manna, L. Fluorescent Alloy CsPbxMn1-xI3 Perovskite Nanocrystals with High Structural and Optical Stability. *ACS Energy Lett.* **2017**, *2*, 2183–2186.

(66) Zou, S.; Liu, Y.; Li, J.; Liu, C.; Feng, R.; Jiang, F.; Li, Y.; Song, J.; Zeng, H.; Hong, M.; Chen, X. Stabilizing Cesium Lead Halide Perovskite Lattice Through Mn(II) Substitution for Air-Stable Light-Emitting Diodes. *J. Am. Chem. Soc.* **2017**, *139*, 11443–11450.

(67) Zhu, J.; Yang, X.; Zhu, Y.; Wang, Y.; Cai, J.; Shen, J.; Sun, L.; Li, C. Room-Temperature Synthesis of Mn-Doped Cesium Lead Halide Quantum Dots with High Mn Substitution Ratio. *J. Phys. Chem. Lett.* **2017**, *8*, 4167–4171.

(68) Yuan, X.; Ji, S.; De Siena, M. C.; Fei, L.; Zhao, Z.; Wang, Y.; Li, H.; Zhao, J.; Gamelin, D. R. Photoluminescence Temperature Dependence, Dynamics, and Quantum Efficiencies in Mn^{2+}-Doped $CsPbCl_3$ Perovskite Nanocrystals with Varied Dopant Concentration. *Chem. Mater.* **2017**, *29*, 8003–8011.

(69) Xu, K.; Lin, C. C.; Xie, X.; Meijerink, A. Efficient and Stable Luminescence from Mn^{2+} in Core and Core-Isocrystalline Shell $CsPbCl_3$ Perovskite Nanocrystals. *Chem. Mater.* **2017**, *29*, 4265–4272.

(70) Ji, S.; Yuan, X.; Li, J.; Hua, J.; Wang, Y.; Zeng, R.; Li, H.; Zhao, J. Photoluminescence Lifetimes and Thermal Degradation of Mn^{2+}-Doped $CsPbCl_3$ Perovskite Nanocrystals. *J. Phys. Chem. C* **2018**, *122*, 40, 23217–23223.

(71) Chen, D.; Fang, Chen, X.; Lei, L.; Zhong, J. Mao, Q. Zhou, S.; Li, J. Mn-Doped $CsPbCl_3$ Perovskite Nanocrystals: Solvothermal Synthesis, Dual-Color Luminescence and Improved Stability. *J. Mater. Chem. C* **2018**, *6*, 8990–8998.

(72) Wang, Q.; Zhang, X.; Jin, Z.; Zhang, J.; Gao, Z.; Li, Y.; Liu, S. F. Energy-Down-Shift $CsPbCl_3$:Mn Quantum Dots for Boosting the Efficiency and Stability of Perovskite Solar Cells. *ACS Energy Lett.* **2017**, *2*, 1479–1486.

(73) Yu, P. Y.; Cardona, M. *Fundamentals of Semiconductors*; Springer, 1996.

(74) Seo, D. K.; Gupta, N.; Whangbo, M. H.; Hillebrecht, H.; Thiele, G. Pressure-Induced Changes in the Structure and Band Gap of $CsGeX_3$ (X = Cl, Br) Studied by Electronic Band Structure Calculations. *Inorg. Chem.* **1998**, *37*, 407–410.

(75) Gana, I.; Barrio, M.; Ghaddar, C.; Nicolaï, B.; Do, B.; Tamarit, J.-L.; Safta, F.; Rietveld, I. B. An Integrated View of the Influence of Temperature, Pressure, and Humidity on the Stability of Trimorphic Cysteamine Hydrochloride. *Mol. Pharmaceutics* **2015**, *12*, 2276–2288.

(76) Kieslich, G.; Sun, S.; Cheetham, A.K. Solid-State Principles Applied to Organic–Inorganic Perovskites: New Tricks for an Old Dog. *Chem. Sci.* **2014**, *5*, 4712–4715.

(77) Zou, S.; Liu, Y.; Li, J.; Liu, C.; Feng, R.; Jiang, F.; Li, Y.; Song, J.; Zeng, H.; Hong, M.; Chen, X. Stabilizing Cesium Lead Halide Perovskite Lattice Through Mn(II) Substitution for Air-Stable Light-Emitting Diodes. *J. Am. Chem. Soc.* **2017**, *139*, 11443–11450.

(78) Li, Z.-J.; Hofman, E.; Davis, A. H.; Khammang, A.; Wright, J. T.; Dzikovski, B.; Meulenberg, R. W.; Zheng, W. Complete Dopant Substitution by Spinodal Decomposition in Mn-Doped Two-Dimensional $CsPbCl_3$ Nanoplatelets. *Chem. Mater.* **2018**, *30*, 6400–6409.

(79) Shannon, R. D.; Prewitt, C. T. Effective Ionic Radii in Oxides and Fluorides. *Acta Crystallogr. Sect. B.* **1969**, *25*, 925–946.

(80) Woltermann, G. M.; Wasson, J. R. An Electron Spin Resonance Study of Hexakis(pyridine N-oxide)manganese(II) Perchlorate Complexes. *Inorg. Chem.* **1973**, *12*, 10, 2366–2370.

(81) Cape, J. A.; White, R. L.; Feigelson, R. S. EPR Study of the Structure of $CsPbCl_3$. *J. Appl. Phys.* **1969**, *40*, 5001–5005.

(82) Nandha, N. K.; Nag, A. Synthesis and Luminescence of Mn-Doped $Cs_2AgInCl_6$ Double Perovskites. *Chem. Comm.* **2018**, *54*, 5205–5208.

(83) Title, R. S. Electron Paramagnetic Resonance Spectra of Cr^{+}, Mn^{++}, and Fe^{3+} in Cubic ZnS. *Phys. Rev.* **1963**, *131*, 2, 623–627.

(84) Vegard, L. Die Konstitution der Mischkristalle und die Raumfüllung der Atome. *Eur. Phys. J. A* **1921**, *5*, 17–26.

(85) Denton, A. R.; Ashcroft, N. W. Vegard 's Law. *Phys. Rev. A: At., Mol., Opt. Phys.* **1991**, *43*, 3161–3164.

(86) Koolyk, M.; Amgar, D.; Aharon, S.; Etgar, L. Kinetics of Cesium Lead Halide Perovskite Nanoparticle Growth; Focusing and De-Focusing of Size Distribution. *Nanoscale* **2016**, *8*, 6403–6409.

(87) Zandbergen, H. W. Neutron Powder Diffraction and Magnetic Measurements on $CsMnI_3$. *J. Solid State Chem.* **1980**, *35*, 367–375.

Appendix of supporting information

Table S1. Comparison Between Pb- and Ge-Based Perovskites.

Compound	E_g (eV)	Bohr Radius (nm)
$CsGeCl_3$	3.67	-
$CsGeBr_3$	2.36	-
$CsGeI_3$	1.60	4–5 (this study)
$CsPbCl_3$	3.0	5
$CsPbBr_3$	2.2	7
$CsPbI_3$	1.7	12
$CH_3NH_3PbCl_3$	3.1	-
$CH_3NH_3PbBr_3$	2.3	2
$CH_3NH_3PbI_3$	1.6	2.2

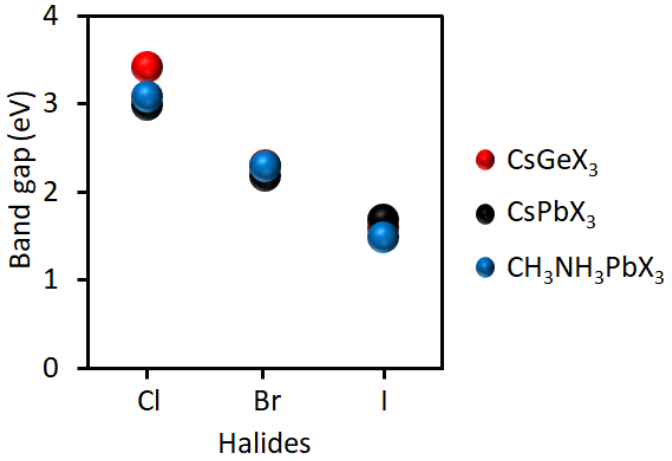

Figure S1. Band gap comparison of germanium and lead halide perovskites.

Scheme S1. Synthesis of Bulk $CsGeI_3$.

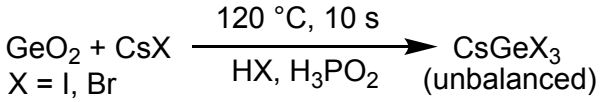

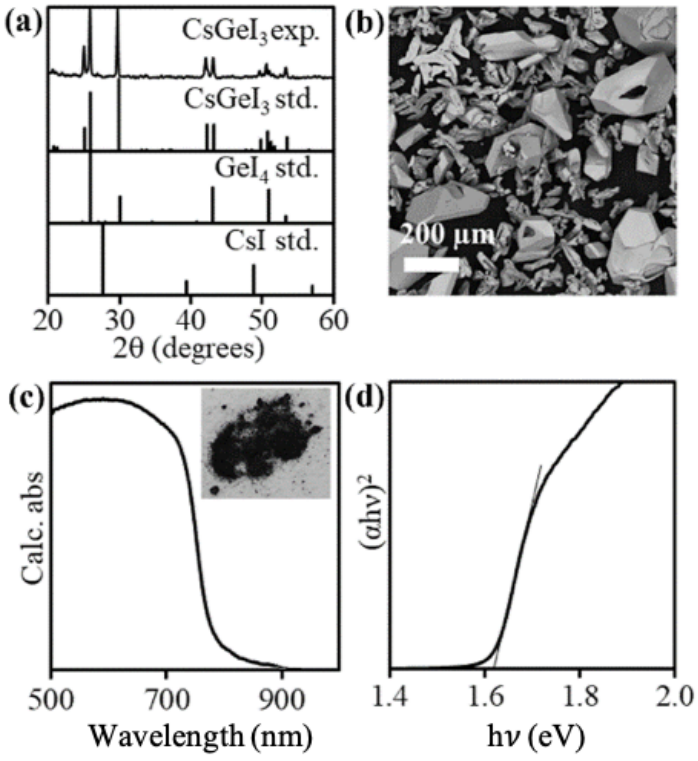

Figure S2. (a) Powder XRD, (b) SEM, (c) diffuse reflectance, and (d) Tauc plot of bulk $CsGeI_3$.

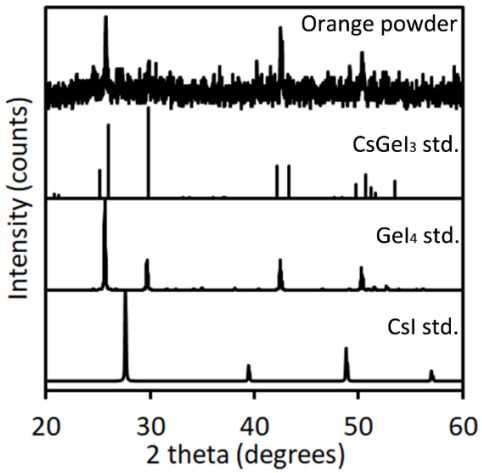

Figure S3. Powder XRD of the orange precipitate obtained soon after GeO_2 is added into the acidic solution. This orange solid then re-dissolves at 120 °C to form a transparent yellow solution. This result shows that GeI_4 is an intermediate that initially forms from the reaction between GeO_2 and HI, followed by reduction with H_3PO_2 to produce a highly soluble form of Ge^{2+}.

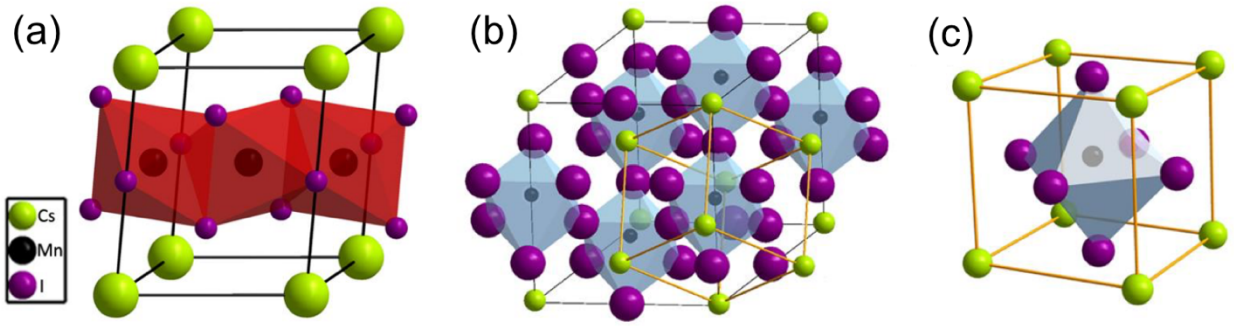

Figure S4. Unit cells of (a) hexagonal $CsMnI_3$, (b) $CsMnI_3$ simulated with the rhombohedral $CsGeI_3$ structure, and (c) zoomed in view showing the octahedral Mn(II) coordination geometry of the small cube in (b). $CsGeI_3$ has a rhombohedral structure with a = 8.3582 Å and c = 10.6098 Å. High spin octahedral Mn^{2+} has an ionic size of 0.97 Å whereas the diameter of Ge^{2+} is 0.87 Å. Assuming the central atoms in the octahedra are in contact with the surrounding halide anions, by substituting Ge^{2+} with Mn^{2+}, this will expand the octahedra by 0.1 Å. This leads to an expansion of the edge of the small cube in (c) by 0.1 Å. Because the longer edge c in (b) is the space diagonal

of the small cube in (c), 0.1 Å expansion of the octahedron will result in an expansion of 0.1 Å × $\sqrt{3}$ = 0.1732 Å for the longer edge c, which gives the length of c axis 10.6098 Å + 0.1732 Å = 10.7830 Å. Because the simulated $CsMnI_3$ retains the structure of $CsGeI_3$, they should have the same value of c/a, which is 1.2694. Therefore, the shorter edge of the simulated $CsMnI_3$ should be 8.4946 Å.

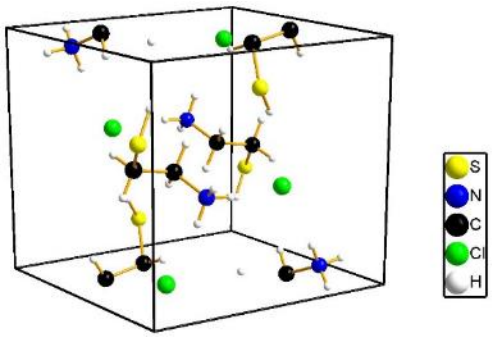

Figure S5. Unit cell of cysteammonium chloride. The volume of cysteammonium chloride unit cell is V(unit cell) = 560 Å^3 and Z = 4. Radius of Cl^- is 1.67 Å. If we assume cysteammonium cations and chloride anions are spheres, the volume of one cation should be V($HSCH_2CH_2NH_3^+$) = V(unit cell)/4 -V(Cl^-) = 120.5 Å^3. Therefore, the radius of cysteammonium cation should be 283 pm.

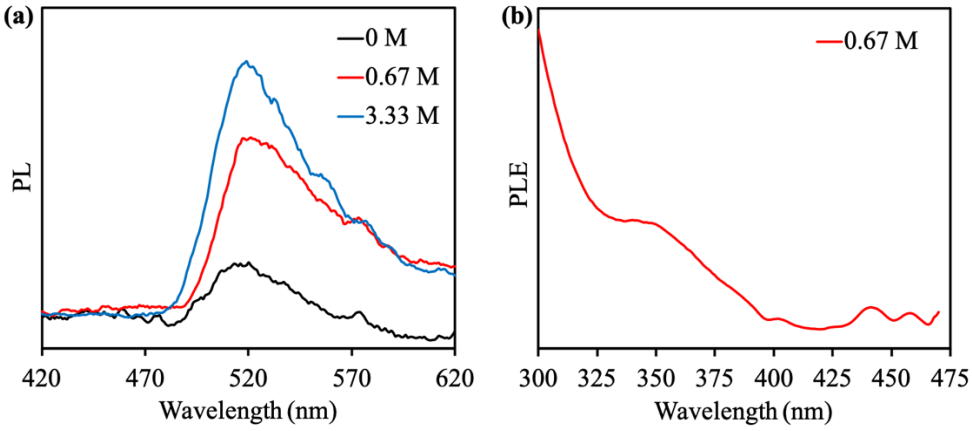

Figure S6. (a) PL with λ_{exc} = 350 nm and (b) representative PLE with λ_{detect} = 517 nm of $CsGeBr_3$ nanocrystals synthesized with different cysteNH$_3$Br concentrations.

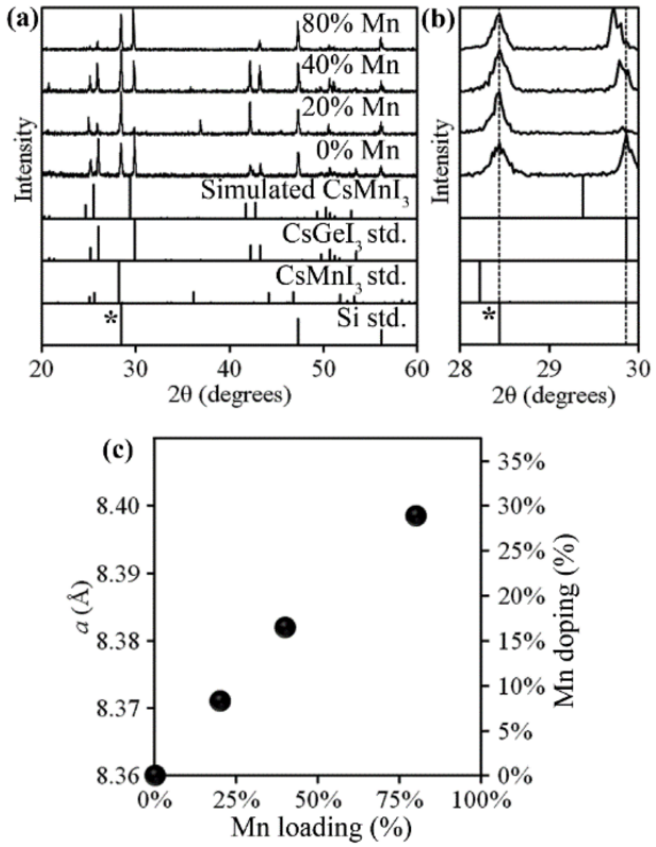

Figure S7. (a) Powder XRD, (b) zoomed in view showing XRD peak shifts, and (c) lattice parameter shift of Mn^{2+}-doped bulk $CsGeI_3$ crystals as a function of synthetic Mn^{2+} loading. Asterisks (*) denote silicon powder used as an internal standard.

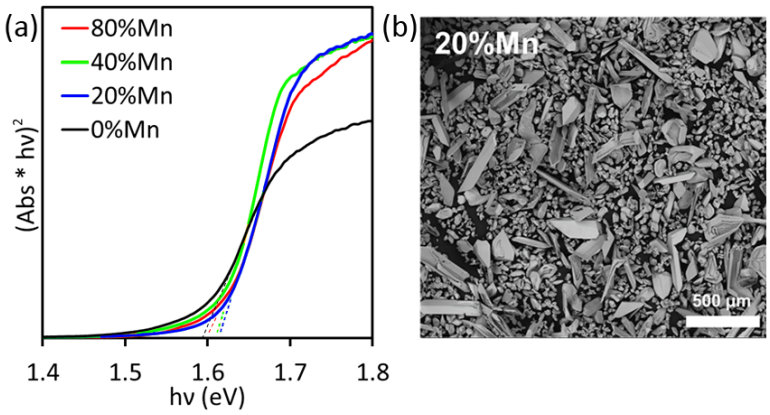

Figure S8. (a) Tauc plot and (b) representative SEM image of Mn^{2+}-doped bulk $CsGeI_3$ crystals made with different synthetic Mn^{2+} loadings.

Table S2. Mn^{2+}-Doped bulk $CsGeI_3$ crystals.

Mn Loading	a (Å)	Mn-Doping (%)	E_g (eV)
0%	8.358	0%	1.61
20%	8.369	8%	1.62
40%	8.380	16%	1.62
80%	8.397	29%	1.60

[

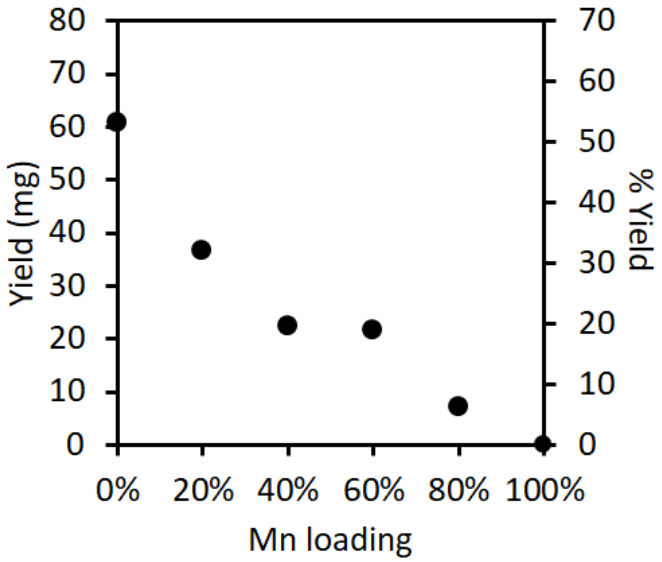

Figure S9. Reaction yields of Mn^{2+}-doped bulk $CsGeI_3$ crystals as a function of synthetic Mn^{2+} loading.

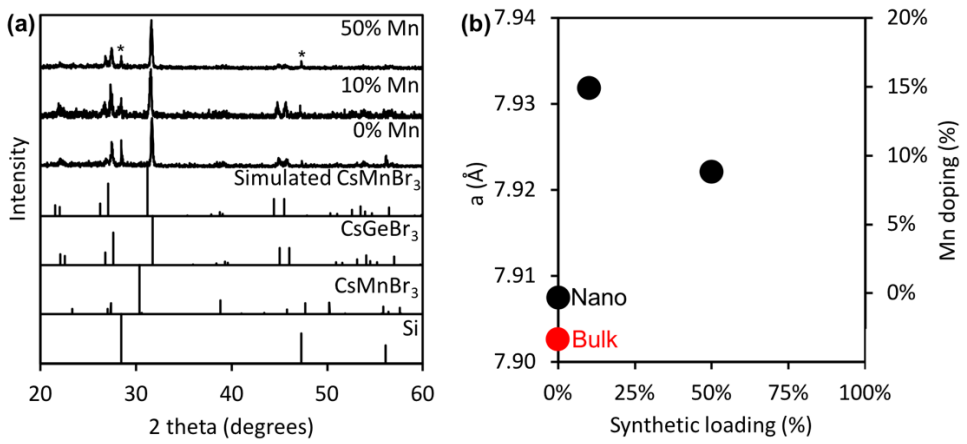

Figure S10. (a) Powder XRD and (b) lattice parameter shift of Mn^{2+}-doped $CsGeBr_3$ nanocrystals as a function of synthetic Mn^{2+} loading. Asterisks (*) denote silicon powder used as an internal standard.

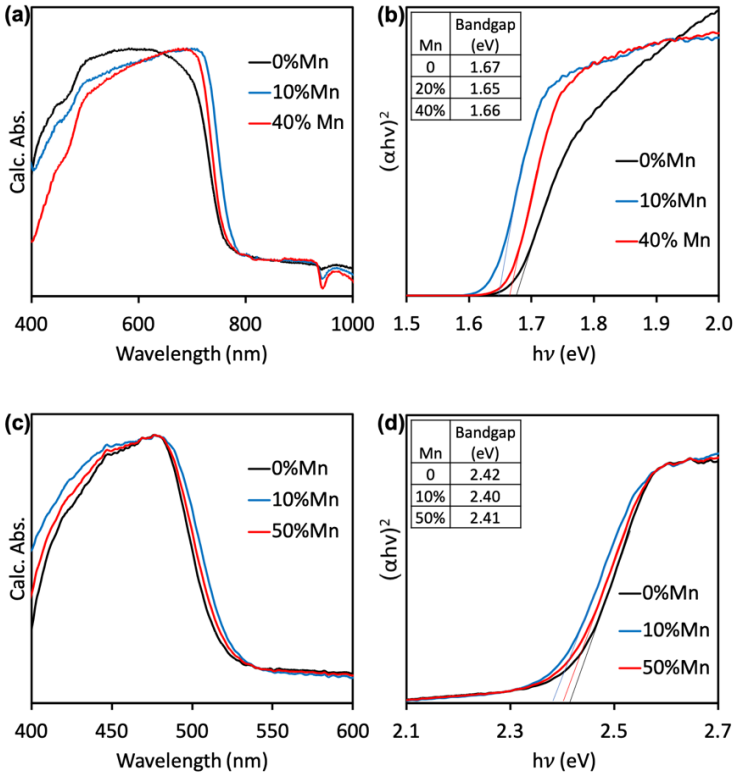

Figure S11. (a) Diffuse reflectance and (b) Tauc plots of $CsGeI_3$ nanocrystals as well as (c) diffuse reflectance and (d) Tauc plots of $CsGeBr_3$ nanocrystals synthesized with various synthetic Mn^{2+} loadings.

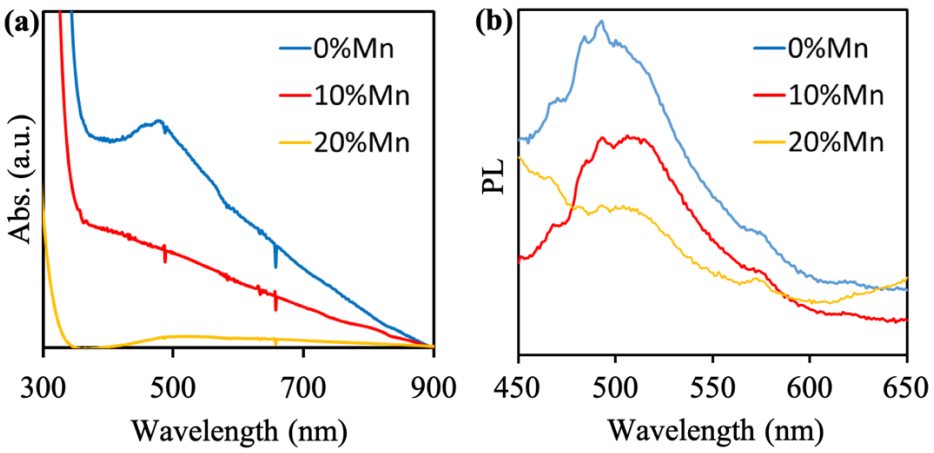

Figure S12. (a) Absorbance and (b) PL of $CsGeBr_3$ nanocrystals synthesized with various synthetic Mn^{2+} loadings (λ_{exc} = 350 nm).

CHAPTER 4

SOLUTION-GROWN SODIUM BISMUTH DICHALCOGENIDES: TOWARD EARTH-ABUNDANT, BIOCOMPATIBLE SEMICONDUCTORS

Reprinted with permission from *J. Am. Chem. Soc.* **2018**, *140*, 3736–3742.

Bryan A. Rosales, Miles A. White, and Javier Vela

Abstract

Many technologically relevant semiconductors contain toxic, heavily regulated (Cd, Pb, As) or relatively scarce (Li, In) elements, and often require high manufacturing costs. We report a facile, general, low-temperature, and size tunable (4–28 nm) solution phase synthesis of ternary $APnE_2$ semiconductors based on Earth-abundant and biocompatible elements (A = Na, Pn = Bi, E = S or Se). The observed experimental band gaps (1.20–1.45 eV) fall within the ideal range for solar cells. Computational investigation of the lowest energy superstructures that result from 'coloring', caused by mixed cation sites present in their rock salt lattice agree with other better-known members of this family of materials. Our synthesis unlocks a new class of low cost and environmentally friendly ternary semiconductors that show properties of interest for applications in energy conversion.

Introduction

Many technologically relevant semiconductors contain toxic and highly regulated elements such as Cd, Pb, or As. Others contain elements that are relatively scarce or poorly distributed in the Earth's crust, such as In (0.05 ppm abundance) or Li (17 ppm),[1] respectively. In contrast, alkali metal-based $APnE_2$ semiconductors are made of relatively abundant and/or biocompatible elements such as Na or K (A), Sb or Bi (Pn), and S or Se (E). The presence of Bi in these compounds is particularly benign because, despite its location among the 'poisoner's corridor' of the periodic table (along with Cd, Hg, Tl, Pb, Po, Rn), Bi-containing compounds are regularly used

in cosmetics (BiOCl) and pharmaceuticals (Pepto-Bismol®).[2] In addition, while relatively scarce (0.03 ppm),[1] Bi is overproduced during Pb mining,[3] leading to a similar market price to that of Ni or Ti (0.96–0.99 ¢/g).

Ternary $APnE_2$ compounds (A = Li, Na, K, Rb, Cs, Cu, Ag, Tl; Pn = As, Sb, Bi; E = S, Se, Te) are an interesting class of semiconductors that hold great technological promise. These materials often adopt a rock salt structure, with the chalcogenide (E) forming an fcc lattice, and a mixture of monovalent/trivalent cations (A/Pn) occupying the octahedral holes (Fig. 1). This disordered structure and the presence of polarizable lone s^2 electrons on Pn[4] lead to efficient phonon scattering,[5] which explains the inherently low thermal conductivity of $AgSbTe_2$ and $AgBiSe_2$.[6] $AgSbTe_2$ exhibits a thermoelectric zT figure of merit of 1.3 at 720K,[5,7] rising to 2.2 at 800K upon alloying with PbTe (lead-antimony-silver-tellurium, or LAST).[8] $AgSb_{0.96}Zn_{0.04}Te_2$ has a zT of 1.9 at 585K, one of the highest among mid-temperature, p-type thermoelectrics.[9] In addition, photovoltaic solar cells made of nanocrystalline $AgBiS_2$ have reached a 6.3% certified power conversion efficiency.[10]

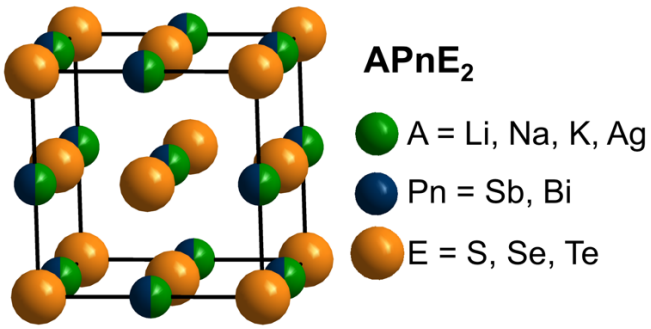

Figure 1. Rock salt structure with mixed cation sites of ternary $APnE_2$ compounds.

Alkali metal-based $APnE_2$ compounds are usually prepared by high temperature solid-state synthesis. A common reaction employs alkali metal carbonates or chalcogenides with either a mixture of Pn (Sb or Bi) and E elements or pnicto-chalcogenide precursors at temperatures between 600–800 °C.[11,12] To our knowledge, there are only a few reports on the solution-phase synthesis of $NaBiS_2$.[13,14] An intermediate $NaBiS_2$ phase forms during the hydrothermal synthesis of Bi_2S_3.[15,16] However, attempts to isolate it resulted in highly aggregated, polydisperse $NaBiS_2$ particles.[13,14] In contrast, reports on the solution phase synthesis of coinage metal(A)-based $ABiE_2$

compounds, in some cases with excellent particle uniformity, are more common.[10,17] Nevertheless, the synthesis of more affordable and biocompatible alkali-based $APnE_2$ compounds remains underdeveloped.

Results and discussion

Solution grown $NaBiS_2$. We have successfully prepared $NaBiS_2$ from the reaction between commercially available NaH, Ph_3Bi and elemental sulfur in 1-octadecene (ODE) (Scheme 1). At 180 °C, single crystallite domains—Scherrer particle sizes measured by powder X-ray diffraction (XRD) peak widths—increase from 13±1 nm at 0.5 h to 28±6 nm after 3 h (Fig. 2, Table 1). In the absence of added surface-binding ligands, transmission electron microscopy (TEM) shows particles with sizes consistent with those calculated from XRD (see SI). A very small amount of Na_2SO_3 (minor phase)—likely produced from post synthetic oxidation of HS^- intermediate upon exposure to air[18] is sometimes observed, but is easily removed with a water-ethanol mixture (see below and Experimental section). Extrapolating the linear region of direct $((Abs \cdot h\nu)^2)$ and indirect $((Abs \cdot h\nu)^{1/2})$ Tauc plots (*vs.* $h\nu$)[19] made from optical absorption measurements yields apparent band gaps of 1.41(0.5 h)–1.37(1 h) eV and 1.07 eV(0.5–1 h), respectively. These values are in rough agreement with prior literature data that report $NaBiS_2$ band gaps ranging from 1.4 eV (direct, from experiment)[13] to 1.28 eV (indirect, from theory).[20] We note that both direct and indirect gaps may be present in $NaBiS_2$, as observed with other semiconductors such as $RbBiS_2$,[21] $NaSbS_2$,[22] and even Ge[23] or $CH_3NH_3PbI_3$.[24]

Scheme 1.

$$3NaH + Ph_3Bi + 3E \xrightarrow[S]{T,\ t} NaBiE_2 + 3Ph\text{-}H + Na_2E$$

E = S or Se
T = 70–180 °C
S = ODE, oleylNH$_2$, or both

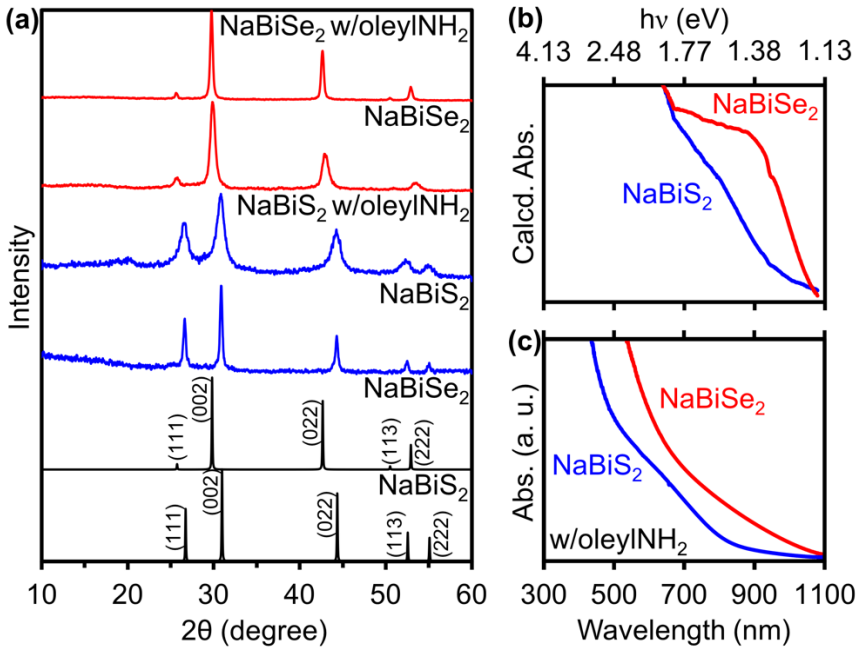

Figure 2. Powder XRD (a), corrected solid-phase diffuse-reflectance (b, see SI), and solution-phase absorption (c) of $NaBiE_2$ made in the presence (c) or absence (b) of $oleylNH_2$.

Table 1. Solution-phase synthesis of $NaBiE_2$ semiconductors.

Product	Conditions[a]	T (°C)	t (h)	Size (nm)		E_g (eV)[b]	
				Scherrer	TEM	d.	i.
$NaBiS_2$[c]	ODE	180	3	28±6	n.d.	1.37	1.07
$NaBiS_2$	ODE + 10 eq. $oleylNH_2$	180	3	27±4	n.d.	1.41	1.01
$NaBiS_2$	$oleylNH_2$	180	3	17±3	n.d.	1.43	1.11
$NaBiS_2$	$oleylNH_2$	180	t_o[d]	10±1	18±4	1.45	1.20
$NaBiS_2$	$oleylNH_2$	70	0.17	3.3±0.5	4.2±0.7	1.41	1.24
$NaBiS_2$	carboxylate + $oleylNH_2$	180	2	4±1	4.4±0.7	1.38	1.16
$NaBiSe_2$	ODE	180	3	10±1	13±5[e]	1.22	1.10
$NaBiSe_2$	$oleylNH_2$ + ODE (1.2:1)	180	3	25±2	21±5	1.23	1.10

[a]$[Na]_0 = [Bi]_0 = [E]_0/2 = 0.023$ M; see experimental. [b]Direct (d.) & indirect (i.) band gaps (E_g) from Tauc plots.[19] [c]Benzene and 73% unreacted Ph_3Bi observed by GC-MS (see SI). [d]Immediate cooling (t_o < 10 s). [e]Major morphology.

Effect of added ligands. Replacing ODE solvent with neat N-oleylamine ($oleylNH_2$) while keeping other conditions constant (3 h at 180 °C) decreases the $NaBiS_2$ Scherrer size to 17±3 nm (Fig. 2, Table 1). Immediate removal from the heating mantle upon reaching the reaction temperature (< 10 s at 180 °C) further decreases the Scherrer size to 10±1 nm. The effect of $oleylNH_2$ appears to be two-fold as, in addition to decreasing particle size, it decreases the $NaBiS_2$

nucleation temperature to only 70 °C, compared to 180 °C in the absence of ligand (neat ODE). Combining these two effects, *i.e.*, running the reaction for 10 min at 70 °C results in a Scherrer size of only 3.3±0.5 nm.

The use of more strongly binding ligands is often used to enhance the morphology, size distribution and colloidal stability of nanocrystals. However, alternative ligands do not always allow the formation of the desired ternary product. For example, introducing trioctylphosphine (TOP)—known as a mild reducing agent under a range of conditions[25] leads instead to the formation of metallic Bi (see SI). Introducing 2-aminoethanethiol to an aqueous mixture of $Na_2S{\cdot}9H_2O$ and Bi(acetate)$_3$ produces black, amorphous solids, regardless of the pH used (2.4, 7 or 12).

Similarly, other precursors and conditions that have been used to prepare coinage metal(A)-based $ABiS_2$ materials[10] are not easily translated to the preparation of $NaBiS_2$. For example, introducing free oleic acid to our synthesis produces binary Bi_2S_3, likely because it quickly reacts with NaH to form Na(oleate). Reaction between Na(oleate), Ph_3Bi and S in ODE at 140 °C results in phase segregated Na(oleate) and binary Bi_2S_3. We have succeeded in introducing strong-binding carboxylate ligands to our synthesis by utilizing carboxylate-based precursors of both metals. Specifically, reaction between Na(oleate), Bi(neodecanoate)$_3$ and S in neat oleylNH_2 at 180 °C yields $NaBiS_2$ nanocrystals with a 4±1 nm Scherrer size (Table 1).

Direct and indirect band gap values[19] measured for all solution grown $NaBiS_2$ samples remain at 1.38–1.45 eV and 1.01–1.24 eV, respectively, indicating that quantum confinement is not present in these samples, unlike the related $AgBiS_2$ system.[26,27] However, their absorption edges become systematically sharper with decreasing particle size (see SI). We also measure a relatively large extinction coefficient of 10^4 $cm^{-1}M^{-1}$. Based on these observations, we hypothesize that the apparent band gap of $NaBiS_2$ transitions from mostly indirect to mostly direct as particle size decreases, as seen for MoS_2.[28]

Our solution-phase synthesis thus enables access to a relatively wide range of $NaBiS_2$ particle sizes (4–28 nm), specifically through tuning the concentration of added oleylNH_2, reaction temperature and time, and through the choice of metal ion precursors used. Further, in all cases studied, even a small amount of oleylNH_2—as little as 10 equiv. relative to Na and Bi—vastly improves solubility and colloidal stability, likely by helping passivate the $NaBiS_2$ particle surface and suppressing agglomeration. TEM analysis shows that the $NaBiS_2$ morphology ranges from

uniformly spherical without agglomeration for the smallest nanocrystals made with carboxylate precursors in oleylNH_2, to cuboctahedral for the larger particles made in the absence of ligands (see SI). Single area electron diffraction (SAED) is consistent with the XRD of phase pure $NaBiS_2$ (Fig. 3). Elemental mapping of the smallest $NaBiS_2$ nanocrystals by energy dispersive X-ray spectroscopy (EDX) yields a slightly metal-rich stoichiometric composition of $Na_{1.18}Bi_{1.17}S_2$, likely compensated by the binding of the anionic ligands.[29]

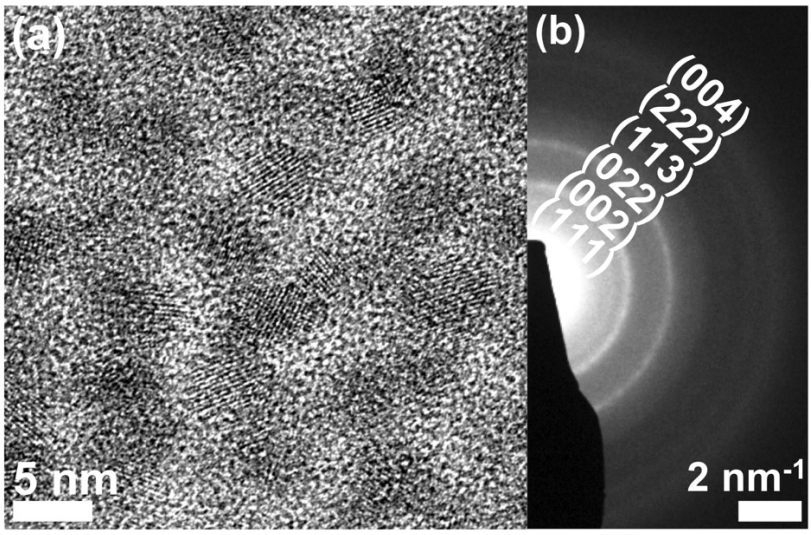

Figure 3. Representative TEM image (a) and SAED (b) of small (4.4±0.7 nm) $NaBiS_2$ nanocrystals prepared with carboxylate ligands.

Extension to $NaBiSe_2$ and mechanism. Successful extension to the synthesis of $NaBiSe_2$ highlights the generality of our method. Replacing elemental S with Se while maintaining similar reaction conditions (NaH, Ph_3Bi, 180 °C for 3 h) results in $NaBiSe_2$ with a Scherrer size of 10±1 nm. A sharp absorption edge is observed, corresponding to either a 1.22 eV direct or a 1.10 eV indirect band gap (see above). Either value is significantly larger than that previously reported of 0.28 eV.[11] However, this latter literature measurement came from a $NaBiSe_2$ sample made from Na_2CO_3 and Bi_2Se_3;[11,30] therefore, a possible explanation may be the presence of unreacted Bi_2Se_3, which is known to have a band gap of only 0.3 eV.[31]

TEM shows that $NaBiSe_2$ prepared in the absence of ligands is mainly comprised of spherical particles (13±5 nm, Table 1); it also contains a minor fraction of cubes, sheets, and wires (8.4±0.8 diameter and 570±160 nm length with (111) lattice fringes perpendicular to their axis) (see SI). Semiconductor nanowires typically form through a solution-liquid-solid (SLS) mechanism, a heterogeneous nucleation process catalyzed by a seed of a low melting metal, such as Bi.[32,33] Thus, the observation of $NaBiSe_2$ nanowires strongly suggests that Ph_3Bi decomposes into an intermediate Bi phase prior to the formation of $NaBiSe_2$. Facile, low temperature (80 °C) reduction of Bi(III) precursors to Bi with both strong and mild reducing agents is well known.[34,35]

XRD monitoring of phase evolution after introducing oleylNH_2 provides additional mechanistic insights. Immediate removal from the heating mantle upon reaching the reaction temperature (< 10 s at 180 °C) and isolation by centrifugation reveals a mixture of unreacted Se, Bi and Na_2SeO_3 (selenite). After 0.5 h, Se is completely consumed and $NaBiSe_2$ (major), Bi^0 and Na_2SeO_3 (minor) phases are observed. After 3 h, only phase pure $NaBiSe_2$ is present. The observation of Na_2SeO_3 at early reaction times strongly indicates the formation of an intermediate HSe^- species. Produced by the reaction between NaH and dissolved Se, HSe^- is easily oxidized post synthesis upon exposure to air to produce Na_2SeO_3—similar to the observation of Na_2SO_3 in the synthesis of the lighter ternary disulfide (see above).[18] The reaction between the metallic Bi and HSe- intermediates and dissolved Se regenerates Bi(III) and produces Se^{2-}, as required for the formation of the final product. This type of redox cycling, while counterintuitive, has ample precedent in the literature.[36,37]

Introducing oleylNH_2 to the synthesis produces $NaBiSe_2$ nanocrystals with a Scherrer size of 25±2 nm and an absorption edge corresponding to direct or indirect band gaps of 1.23 or 1.10 eV, respectively (Fig. 2). These nanocrystals display a very large extinction coefficient of 10^6 $cm^{-1}M^{-1}$. HR TEM and SAED reveal uniform 21±5 nm particle size and morphology (Fig. 4 and SI). Slow leaching of Na when exposed to the electron beam—known to easily reduce and vaporize alkali metals[38,39] may be responsible for the observed slightly off-stoichiometric EDX composition of $Na_{0.8}Bi_{1.2}Se_2$.

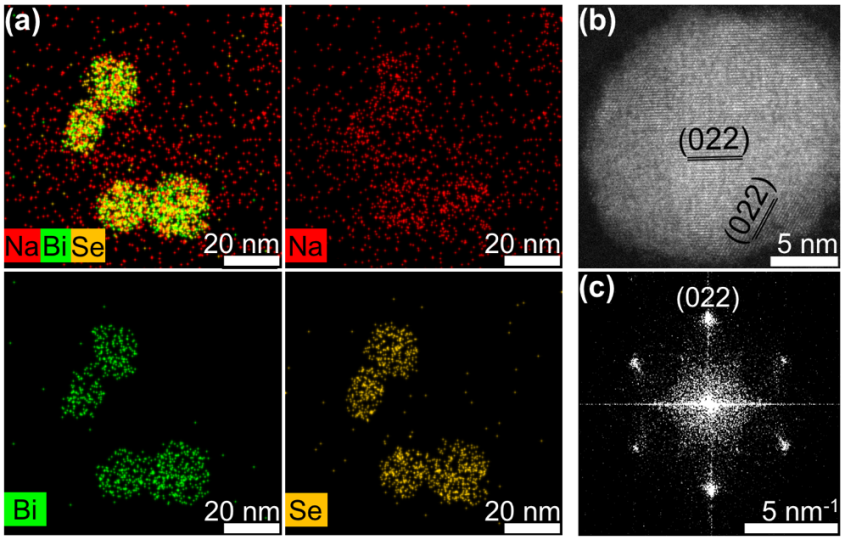

Figure 4. Representative EDX elemental mapping (a), HR TEM (b), and fast Fourier transform (FFT) (b) of $NaBiSe_2$ nanocrystals prepared with oleylNH_2 at 180 °C for 3 h.

Surface chemistry. The infrared (IR) spectra of ligand-stabilized $NaBiS_2$ and $NaBiSe_2$ show stretching and bending modes typical of unsaturated amines (see SI), indicating both are capped with oleylNH_2. The IR spectrum of $NaBiS_2$ also contains three strong extra peaks at 1133 cm^{-1} (C=S), 1007 cm^{-1} (C-N) and 675 cm^{-1} (C-S),[40] which were previously shown to arise from thioamides, amidines, and thioethers formed upon reaction of oleylNH_2 with elemental S.[41,42]

X-ray photoelectron spectroscopy (XPS) shows that Na^+, Bi^{3+}, E^{2-} and R-NH_2 surface species are present in both $NaBiE_2$ compounds (see SI). The XPS spectrum of $NaBiS_2$ shows one additional SO_4^{2-} species, indicating this material undergoes surface oxidation upon exposure to air (within *ca.* 20 min). We note that this sulfate species is unrelated to the sulfite species formed post synthesis when not all the HS^- intermediate was consumed during the synthesis of $NaBiS_2$ (as observed by XRD, see above). The lack of a similarly oxidized Se species in $NaBiSe_2$ suggests its surface is comparatively more resistant to oxidation.

Interestingly, we observe that $NaBiS_2$ crystals larger than 10 nm lose colloidal stability within 2 h after exposure to air, even though they are stable for over 1 mo. when stored in a dry glovebox. In contrast, smaller, 4.2 nm $NaBiS_2$ crystals are stable for at least 3 days upon exposure to air. We rationalize this size-dependent stability toward oxidation based on the well-known surface structures of other rock salt materials. For example, IV-VI semiconductors display cation-

rich surfaces composed of Pb-only (111) or stoichiometric PbE (100) facets.[29] A decrease in particle size is accompanied by a shape transition from cuboctahedal (both (111) and (100) facets) to octahedral (only (111) facets).[43] In other words, the rock salt surface becomes more cation rich with decreasing particle size. Because the oleylNH_2 used here is an L type ligand that preferentially binds to cations,[44,45] it makes sense that smaller particles containing mostly cation-only (111) facets are better passivated and thus more stable against surface oxidation.[36] Additional enhancement in colloidal stability results when a more strongly-binding surface ligand such as X-type (anionic), bidentate carboxylates are used.[44,45] Small carboxylate-stabilized $NaBiS_2$ nanocrystals are soluble as crude or toluene solutions for over two weeks without signs of precipitation. Additional surface ligand engineering will be required to further enhance the stability of larger sized particles.

Correlating theory and spectroscopy. The mixed cation site occupancies in rock salt $APnE_2$ compounds are a consequence of various superstructures known as 'coloring' patterns in solid state chemistry.[46–48] Thus, a thorough analysis of these coloring patterns is required to understand their optoelectronic properties. Partial computational investigations into the band gap of alkali-based $ABiS_2$ compounds exist,[19,49] but a wider selection of coloring patterns and their relative stability remain to be investigated.

Each chalcogenide in the rock-salt structure is octahedrally coordinated to six cations that may have different A:Bi ratios of: 3:3, where three similar cations lie on the same plane (mer) or face (fac) of the octahedron; 4:2 and 2:4, where two similar cations are in opposite (trans) or neighboring (cis) positions relative to each other; 1:5 and 5:1; and 6:0 and 0:6 (Fig. 5a). Among these, the 3:3 fac octahedra can be used to build two possible extended structures: rhombohedral ($R\bar{3}m$, known as $L1_1$[5] and AF-II[50,51]), with alternating A and Bi layers sandwiched in between E layers; and cubic ($Fd\bar{3}m$, known as D4[5] and AF-IIb[50,51]), where every (001) plane alternates between rows of a single cation or alternating A and Bi (Fig. 5b). Coloring patterns of 6:0 and 0:6 cannot be used to build a $ABiE_2$ stoichiometry and need not be considered.

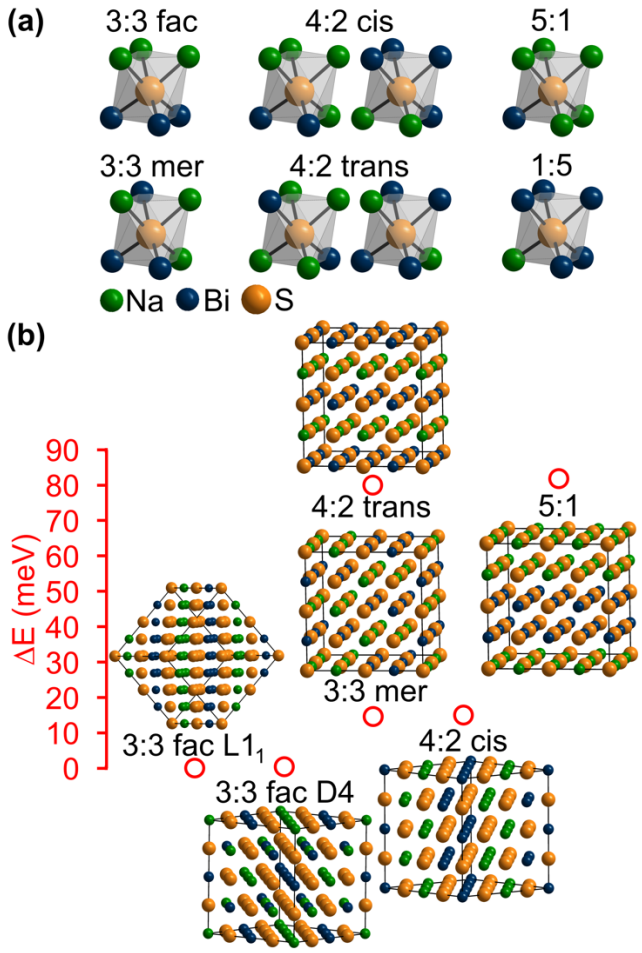

Figure 5. Mixed cation and ordered superstructures of $APnE_2$ compounds. (a) Rock salt structure. (b) Site occupancies of $A_xBi_{6-x}S$ octahedra that can be used to build (a). (c) Calculated energies for the local superstructures derived from the possible coloring patterns[46–48] in (b) (relative to lowest energy 3:3 fac $L1_1$, see Methods).

Using the Vienna *Ab-initio* Simulation Package (VASP)[52] with the local density approximation (LDA) yields two relatively close, lowest energy superstructures 3:3 fac $L1_1$ (0 in Fig. 5b) and 3:3 fac D4 ($\Delta E = +0.2$ meV), which agrees with previous calculations on other $APnE_2$ compounds.[5,50,51] Density of states (DOS) calculations for the lowest energy superstructure (3:3 fac $L1_1$) obtained using TB-mBJ[53,54] yield band gap values that are 30-50% larger than those experimentally observed for "bulk" $NaBiS_2$ and $NaBiSe_2$ obtained in the absence of added ligands (Fig. 6). To probe this issue, we performed similar band gap calculations for the related compound $AgBiS_2$, and found a very similar overestimation of 50% (see SI). A recent theoretical study of

$AgBiS_2$, using more accurate HSE06 hybrid functions yielded even higher values (overestimation of 93%), and attributed this discrepancy to cation disorder.[55] Therefore, the band gaps of $NaBiS_2$ and $NaBiSe_2$ may be tunable through additional synthetic manipulation of the extent of cation disorder present in these systems.

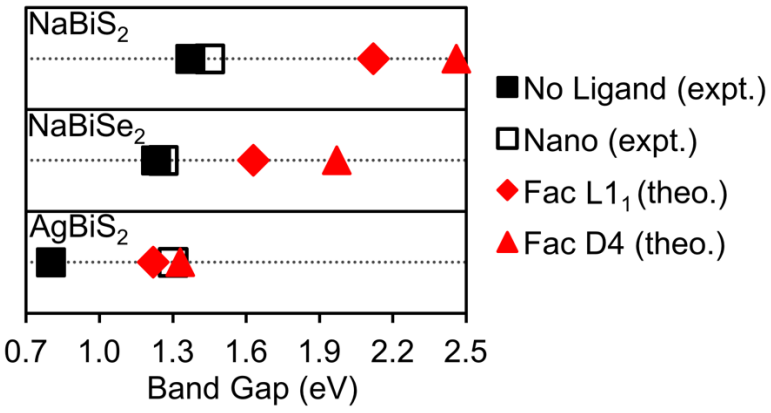

Figure 6. Experimental, and theoretical band gaps for two lowest energy superstructures (both 3:3 fac), of $NaBiS_2$ and $NaBiSe_2$.

Conclusions

Herein, we report a facile, general, low-temperature and size-tunable solution phase synthesis of ternary alkali bismuth dichalcogenides ($ABiE_2$) that utilizes readily accessible, commercially available precursors. The synthesis of $NaBiS_2$ is very sensitive to the specific choice of precursors and ligands. For example, oleylNH_2 results in $NaBiS_2$ while, depending on the precursors used, free (protonated) oleic acid or TOP can lead to Bi_2S_3 or metallic Bi, respectively. Controlling oleylNH_2 concentration, reaction temperature and time, and introducing carboxylate-based precursors give access to particle sizes between 4–28 nm. OleylNH_2, in particular has a three-fold effect: it decreases particle size, it improves colloidal stability, and it reduces the nucleation temperature of $NaBiS_2$ to as little as 70 °C. The $NaBiS_2$ prepared in this way displays an inverse relationship between air stability and particle size. Similar to other rock salt IV-VI compounds, $NaBiS_2$ particles larger than >10 nm lose colloidal stability within 2 h after exposure to air. In contrast, smaller $NaBiS_2$ particles contain a larger fraction of cation-only (111) facets and are better passivated by carboxylates and/or oleylNH_2, remaining stable for at least 2 weeks after

exposure to air. XPS taken within 20 min of exposure to air shows the presence of oxidized chalcogen species (SO_4^{2-}) on the surface of $NaBiS_2$, but not on the surface of $NaBiSe_2$, indicating the former is more prone to surface oxidation.

Successful extension to the preparation of both $NaBiS_2$ and $NaBiSe_2$ demonstrates the generality of our synthetic method. The inability to grow $NaBiSe_2$ below 180 °C suggests that formation of $NaBiSe_2$ is significantly slower than that of $NaBiS_2$. A phase evolution XRD study of $NaBiSe_2$ formation as a function of time found that both metallic Bi and HSe^-—observed indirectly as its air-oxidation product, Na_2SeO_3—are intermediates in the reaction. Therefore, we propose a mechanism whereby NaH reacts first with Ph_3Bi and Se to form Bi and HSe^-, respectively. Subsequently, Bi and HSe^- react with Se to produce the ternary $NaBiSe_2$ phase. The available evidence (for example, the observation of Na_2SO_3 in some cases) points to a similar mechanism for the formation of $NaBiS_2$.

We note that both direct and indirect band gaps may be present in $NaBiS_2$, as observed with other semiconductors including $NaSbS_2$, $RbBiS_2$, Ge, and $CH_3NH_3PbI_3$. Tauc analysis of the optical absorption edge in solution-made $NaBiS_2$ yields apparent band gaps that are consistent with prior literature data, namely: 1.4(direct)–1.07(indirect) eV. Interestingly, the $NaBiS_2$ absorption edge becomes sharper for smaller particles, suggesting a transition from indirect to direct with decreasing particle size, as seen for MoS_2. Similar 1.2(direct)–1.1(indirect) eV band gap values for $NaBiSe_2$ indicate that the previously reported value of 0.28 eV was actually due to sample contamination by the well-known narrow band gap binary, Bi_2Se_3. Both $NaBiS_2$ and $NaBiSe_2$ nanocrystals exhibit large extinction coefficients in the range 10^4–10^6 $cm^{-1}M^{-1}$, suggestive of direct band gap character.

Ternary alkali bismuth dichalcogenides have various possible coloring patterns due to their mixed cation sites. Using *ab initio* calculations, we determined the lowest energy superstructures that result from these coloring patterns, and found 3:3 fac $L1_1$ and 3:3 fac D4 to be lowest in energy. TB-mBJ calculations yield theoretical band gap values that are 30-50% larger than those experimentally observed for solution-made $NaBiS_2$ and $NaBiSe_2$. This is consistent with a similar overestimation of 50% for the better studied ternary material $AgBiS_2$. As observed in this system, such overestimation is accounted for by additional cation disorder in the crystalline lattice. In contrast to many technologically relevant semiconductors made of highly regulated (Cd, Pb, As) or poorly distributed elements (Li, In), ternary $NaBiS_2$ semiconductors are made of relatively

abundant and biocompatible elements. We believe the experimental and computational results reported here will help advance the fundamental study and exploration of these and similar materials for energy conversion devices.

Methods

Materials. Sulfur (99.999) and oleic acid (90%) were purchased from Alfa Aesar; NaH (95%,) from Sigma; 1-octadecene (ODE, technical grade, 90%), oleylamine (oleylNH_2, technical grade, 70%), bismuth(III) neodecanoate and selenium (100 mesh powder, 99.99%) from Aldrich; Ph_3Bi (99%), trioctylphosphine (TOP, min. 97%), and sodium oleate (99%) from Strem; toluene (99.9%) from Fisher. All chemicals were used as received.

Synthesis. *Selenium stock solution.* Se powder (2.20 mmol, 174 mg) and anhydrous ODE (22 mL) were heated at 180 °C for 5 h until homogeneous. *Synthesis without added ligands.* NaH (0.11 mmol, 2.9 mg), Ph_3Bi (0.11 mmol, 50 mg), chalcogen (0.22 mmol, 7.3 mg S or 2.3 mL of Se stock solution), and degassed ODE (5 mL for S or 2.7 mL for Se) were stirred under Ar for 0.5–1 h, heated at 180 °C for 3 h, then cooled by removal from the heating mantle. CAUTION! NaH is a highly corrosive, flammable solid that releases H_2 upon exposure to acids and moisture. NaH should be handled under inert gas. *$NaBiS_2$ ligand screening*. NaH (0.11 mmol, 2.9 mg), Ph_3Bi (0.11 mmol, 50 mg), S (0.22 mmol, 7.3 mg), ligand (1.1 mmol, 0.52 mL TOP or 0.40 mL oleic acid or 0.54 mL oleylNH_2), and enough degassed ODE to complete a total volume of 5 mL were stirred under Ar at 21 °C (RT) for 0.5–1 h, heated at 180 °C for 3 h, then cooled by removal of the heating mantle. *Effect of oleylNH_2*. NaH (0.11 mmol, 2.9 mg), Ph_3Bi (0.11 mmol, 50 mg), chalcogen (0.22 mmol, 7.3 mg S or 2.3 mL Se stock solution), and degassed oleylNH_2 (5 mL for S or 2.7 mL for Se) were stirred at RT under Ar for 0.5–1 h, heated at 70 °C or 180 °C for 0–3 h (see discussion above and Table 1), then cooled by removal of heating mantle. CAUTION! OleylNH_2 is a strong highly-corrosive base. Safety goggles, gloves, and a lab coat should be worn whenever handling oleylNH_2. *Effect of carboxylates*. Sodium oleate (0.11 mmol, 35 mg), bismuth(III) neodecanoate (0.11 mmol, 70 μL), S (0.22 mmol, 7.3 mg), and degassed oleylNH_2 (5 mL) were stirred at RT under Ar for 0.5–1 h, heated at 180 °C for 2 h, then cooled by removal from the heating mantle. *Purification.* The crude solution was diluted to 15 mL with acetone, centrifuged at 5000 rpm for 3 min, and the supernatant discarded. The precipitate was then washed with a mixture of toluene (~ 0.5–1 mL) and acetone (15 mL). $NaBiS_2$ synthesized in neat ODE

(without oleylNH_2) requires further purification by a 1:1 water-ethanol mixture (10 mL) to remove Na_2SO_3.

Optical Characterization. *Diffuse-reflectance* spectra were measured with a SL1 Tungsten Halogen lamp (vis-IR), a SL3 Deuterium Lamp (UV), and a BLACK-Comet C-SR-100 spectrometer. Samples were prepared by drop-casting toluene solutions onto glass slides. *Solution absorbance* spectra were measured with a photodiode array Agilent 8453 UV-Vis spectrophotometer with solvent absorption (toluene) subtracted from all spectra. *Band gap values* were estimated by extrapolating the linear slope of Tauc plots by plotting $(Ah\nu)^{1/r}$ *vs.* $h\nu$ where A = absorbance, $h\nu$ = incident photon energy in eV, r = ½ for direct and r = 2 for indirect semiconductors.[19] *Infrared spectroscopy* measurements were performed on a Bruker Tensor 37 Fourier transform IR spectrophotometer (16 scans, transmittance mode, 4 cm^{-1} resolution).

Structural Characterization. *Powder X-ray diffraction* patterns were measured using Cu Kα radiation on a Rigaku Ultima IV (40 kV, 44 mA) diffractometer using a background-less quartz sample holder. Scherrer analysis was performed with Jade using a κ value of 0.9. Percent compositions were determined with PowderCell. *Transmission Electron Microscopy* imaging and selected area electron diffraction were performed on an FEI Tecnai G2-F20 scanning transmission electron microscope. All size distributions contain information from at least 300 particles.[56] *EDS Elemental Mapping* was performed on an FEI Titan Themis Cubed Aberration Corrected Scanning Transmission Electron Microscope (STEM)

Other. *X-Ray Photoelectron Spectroscopy* measurements were performed using a Kratos Amicus/ESCA 3400 instrument. The sample was irradiated with 240 W unmonochromated Mg *Kα* x-rays, and photoelectrons emitted at 0° from the surface normal were energy analyzed using a DuPont type analyzer. The pass energy was set at 150 eV and either a Shirley or linear baseline was removed from all reported spectra. CasaXPS was used to process raw data files. XPS spectra were energy calibrated to the C 1s peak position at 284.6 eV. Bi 4f and S 2p were deconvoluted by applying constraints that require the Bi 4f 5/2 and 4f 7/2 peaks to have a ratio of 3:4 with a peak separation of 5.3 eV. *Gas Chromatography-Mass-Spectrometry* was performed on an Agilent 8453 nominal mass GC-MS based on quadrupole technology with a DB5 column. The column was maintained at 40 °C for 4 min, then heated to 320 °C over 15 min.

Calculations. Electronic structure calculations were performed using the Vienna *Ab-initio* Simulation Package (VASP)[52] with projected augmented-wave (PAW) pseudopotentials

with a cutoff energy of 500 eV and a convergence energy of $1x10^{-6}$ eV. A conjugated algorithm was applied to the structural optimization with an 11×11×11 Monkhorst-pack k-points grid. During structural optimization, atomic coordinates and cell volumes were allowed to relax. Total energies were calculated using the tetrahedron method with Blöchl corrections applied. All calculations treated exchange and correlation by the local density approximation (LDA). Band gaps were determined from DOS calculated by TB-mBJ[53,54] using the experimental lattice parameter. TB-mBJ band gaps generally better agree with experiment, while LDA considerably underestimates them.[57,58] Each coloring pattern investigated was constructed using 2x2x2 supercells composed of 16 atoms each.

Acknowledgements

J.V. and B.A.R. thank the U.S. National Science Foundation for a CAREER Grant and an AGEP GR Supplement, respectively, from the Division of Chemistry, Macro- molecular, Supramolecular, and Nanochemistry Program (#1253058). XPS work was performed at the Materials Analysis and Research Laboratory of the ISU Office of Biotech. Electron microscopy was performed at the Sensitive Instrument Facility of the Ames Laboratory, which is operated for the U.S. Department of Energy by Iowa State University under contract #DE-AC02-07CH11358. We thank D. Jing for comments.

References

(1) British Geological Survey, Risk List 2012. http://www.bgs.ac.uk/ (accessed January 15th, 2017)

(2) Mohan, R. Green Bismuth. *Nat. Chem.* **2010**, *2*, 336.

(3) Vesborg, P. C. K.; Jaramillo, T. F. Addressing the Terawatt Challenge: Scalability in the Supply of Chemical Elements for Renewable Energy. *RSC Adv.* **2012**, *2*, 7933–7947.

(4) Nielsen, M. D.; Ozolins, V.; Heremans, J. P. Lone Pair Electrons Minimize Lattice Thermal Conductivity. *Energy Environ. Sci.* **2013**, *6*, 570–578.

(5) Ma, J.; Delaire, O.; May, A. F.; Carlton, C. E.; McGuire, M. A.; VanBebber, L. H.; Abernathy, D. L.; Ehlers, G.; Hong, T.; Huq, A.; Tian, W.; Keppens, V. M.; Shao-Horn, Y.; Sales, B. C. Glass-Like Phonon Scattering From a Spontaneous Nanostructure in $AgSbTe_2$. *Nat. Nanotechnol.* **2013**, *8*, 445–451.

(6) Morelli, D. T.; Jovovic, V.; Heremans, J. P. Intrinsically Minimal Thermal Conductivity in Cubic I-V-VI_2 Semiconductors. *Phys. Rev. Lett.* **2008**, *101*, 035901, 1–4.

(7) Wood, C. Materials for Thermoelectric Energy Conversion. *Rep. Prog. Phys.* **1988**, *51*, 459–539.

(8) Hsu, K. F.; Loo, S.; Guo, F.; Chen, W.; Dyck, J. S.; Uher, C.; Hogan, T.; Polychroniadis, E. K.; Kanatzidis, M. G. Cubic $AgPb_mSbTe_{2+m}$: Bulk Thermoelectric Materials with High Figure of Merit. *Science* **2004**, *303*, 818–821.

(9) Roychowdhury, S.; Panigrahi, R.; Perumal, S.; Biswas, K. Ultrahigh Thermoelectric Figure of Merit and Enhanced Mechanical Stability of p-Type $AgSb_{1-x}Zn_xTe_2$. *ACS Energy Lett.* **2017**, *2*, 349–356.

(10) Bernechea, M; Miller, N. C.; Xercavins, G.; So, D.; Stavrinadis, A.; Konstantatos, G. Solution-Processed Solar Cells Based on Environmentally Friendly $AgBiS_2$ Nanocrystals. *Nat. Photon.* **2016**, *10*, 521–526.

(11) Lazarev, V. B.; Salov, A. V.; Berul, S. I. Preparation and Physicochemical Properties of A-IB-VX-VI_2-Type Compounds. *Zh. Neorg. Khim.* **1979**, *24*, 3, 563–580.

(12) Park, Y.; McCarthy, T. J.; Sutorlk, A. C.; Kanatzidis, M. G.; Gillan, E. G. Synthesis of Ternary Chalcogenides in Molten Polychalcogenide Salts: α-$KCuQ_4$, $KAuS_5$, $NaBiS_2$, $KFeQ_2$ (Q = S, Se). *Inorg. Synth.* **1995**, *30*, 88–95.

(13) Kang, S.; Hong, Y.; Jeon, Y. A Facile Synthesis and Characterization of Sodium Bismuth Sulfide ($NaBiS_2$) Under Hydrothermal Condition. *Bull. Korean Chem. Soc.* **2014**, *35*, 6, 1887–1890.

(14) Fei, H.; Feng, Z.; Liu, X. Novel Sodium Bismuth Sulfide Nanostructures: A Promising Anode Materials for Sodium-Ion Batteries with High Capacity. *Ionics* **2015**, *21*, 1967–1972.

(15) Liu, Z.; Peng, S.; Xie, Q.; Hu, Z.; Yang, Y.; Zhang, S.; Qian, Y. Large-Scale Synthesis of Ultralong Bi_2S_3 Nanoribbons via a Solvothermal Process. *Adv. Mater.* **2003**, *15*, 11, 936–940.

(16) Liu, Z.; Liang, J.; Li, S.; Peng, S.; Qian, Y. Synthesis and Growth Mechanism of Bi_2S_3 Nanoribbons. *Chem. Eur. J.* **2004**, *10*, 634–640.

(17) Shi, L.; Wu, C.; Ding, J. *J.* Effect of Solvent on the Synthesis of $AgBiSe_2$ Nanostructures. *Alloys Compd*. **2016**, *684*, 112–115.

(18) Sada, E.; Kumazawa, H.; Hashizume, I.; Shimono, M.; Sakaki, T. Oxidation of Aqueous Sodium Sulfide Solutions with Activated Carbon. *Ind. Eng. Chem. Res.* **1987**, *26*, 1782–1787.

(19) Viezbicke, B. D.; Patel, S.; Davis, B. E.; Birnie III, D. P. Evaluation of the Tauc Method for Optical Absorption Edge Determination: ZnO Thin Films as a Model System. *Phys. Status Solidi B* **2015**, *8*, 1700−1710.

(20) Gabrel'yan, B. V.; Lavrentiev, A. A.; Nikiforov, I. Y.; Sobolev, V. V. Electronic Energy Structure of $MBiS_2$ (M = Li, Na, K) Calculated with Allowance for the Difference Between the M-S and Bi-S Bond Lengths. *J. Struct. Chem.* **2008**, *49*, 5, 788–794.

(21) Brandt, R. E.; Stevanović, V.; Ginley, D. S.; Buonassisi, T. Identifying Defect-Tolerant Semiconductors with High Minority Carrier Lifetimes: Beyond Hybrid Lead Halide Perovskites. *MRS Commun.* **2015**, *5*, 2, 265–275.

(22) Sun, J.; Singh, D. J. Electronic Properties, Screening, and Efficient Carrier Transport in $NaSbS_2$. *Phys. Rev. Appl.* **2017**, *7*, 024015.

(23) Ramasamy, K.; Kotula, P. G.; Fidler, A. F.; Brumbach, M. T.; Pietryga, J. M. Ivanov, S. A. Sn_xGe_{1-x} Alloy Nanocrystals: A First Step Toward Solution-Processed Group IV Photovoltaics. *Chem. Mater.* **2015**, *27*, 13, 4640–4649.

(24) Hutter, E. M.; Gélvez-Rueda, M. C.; Osherov, A.; Bulović, V.; Grozema, F. C.; Stranks, S. D.; Savenije, T. J. Direct-Indirect Character of the Bandgap in Methylammonium Lead Iodide Perovskite. *Nat. Mater.* **2017**, *16*, 115–121.

(25) Liu, J.; Jeong, H.; Liu, J.; Lee, K.; Park, J.-Y.; Ahn, Y. H.; Lee, S. Reduction of Functionalized Graphite Oxides by Trioctylphosphine in Non-Polar Organic Solvents. *Carbon* **2010**, *48*, 2282–2289.

(26) Viñes, F.; Bernechea, M.; Konstantatos, G.; Illas, F. Matildite Versus Schapbachite: First-Principles Investigation of the Origin of Photoactivity in $AgBiS_2$. *Phys. Rev. B* **2016**, *94*, 235203.

(27) Pejova, B.; Nesheva, D.; Aneva, Z.; Petrova, A. Photoconductivity and Relaxation Dynamics in Sonochemically Synthesized Assemblies of $AgBiS_2$ Quantum Dots. *J. Phys. Chem. C* **2011**, *115*, 37–46.

(28) Mak, K. F.; Lee, C.; Hone, J.; Shan, J.; Heinz, T. F. Atomically Thin MoS_2: A New Direct-Gap Semiconductor. *Phys. Rev. Lett.* **2010**, *105*, 136805.

(29) Ko, J.-H.; Yoo, D.; Kim, Y.-H. Atomic Models for Anionic Ligand Passivation of Cation-Rich Surfaces of IV-VI, II-VI, and III-V Colloidal Quantum Dots. *Chem. Com.* **2017**, *53*, 388–391.

(30) Golovei, M. I.; Berul, S. I.; Luzhnaya, N. P.; Peresh, E. Y. Preparation and Certain Properties of Alkali Metal Metaselenobismuthites. *Izv. Akad. Nauk SSSR, Neorg. Mater.* **1970**, *6*, 6, 1100–1104.

(31) Nechaev, I. A.; Hatch, R. C.; Bianchi, M.; Guan, D.; Friedrich, C.; Aguilera, I.; Mi, J. L.; Iversen, B. B.; Blügel, S.; Hofmann, P.; Chulkov, E. V. Evidence for a Direct Band Gap in the Topological Insulator Bi_2Se_3 from Theory and Experiment. *Phys. Rev. B* **2013**, *87*, 121111.

(32) Wang, F.; Dong, A.; Buhro, W. E. Solution-Liquid-Solid Synthesis, Properties, and Applications of One-Dimensional Colloidal Semiconductor Nanorods and Nanowires. *Chem. Rev.* **2016**, *116*, 10888–10933.

(33) Tongying P., Zhukovskyi M., Kuno M. Synthesis and Application of Solution-Based II–VI and IV–VI Semiconductor Nanowires. In *Anisotropic Nanomaterials. Preparation, Properties, and Applications;* Li, Q., Eds.; Springer: Cham, 2015; Chapter 4, pp 119–156.

(34) Son, J. S.; Park, K.; Han, M.-K.; Kang, C.; Park, S.-G.; Kim, J.-H.; Kim, W.; Kim, S.-J.; Hyeon, T. Large-Scale Synthesis and Characterization of the Size-Dependent Thermoelectric Properties of Uniformly Sized Bismuth Nanocrystals. *Angew. Chem. Int. Ed.* **2011**, *50*, 1363–1366.

(35) He, M.; Protesescu, L.; Caputo, R.; Krumeich, F.; Kovalenko, M. V. A General Synthesis Strategy for Monodisperse Metallic and Metalloid Nanoparticles (In, Ga, Bi, Sb, Zn, Cu, Sn, and Their Alloys) via in Situ Formed Metal Long-Chain Amides. *Chem. Mater.* **2015**, *27*, 635–647.

(36) Mobarok, M. H.; Luber, E. J.; Bernard, G. M.; Peng, L.; Wasyl-ishen, R. E.; Buriak, J. M. Phase-Pure Crystalline Zinc Phosphide Nanoparticles: Synthetic Approaches and Characterization. *Chem. Mater.* **2014**, *26*, 1925–1935.

(37) Henkes, A. E.; Vasquez, Y.; Schaak, R. E. Converting Metals into Phosphides: A General Strategy for the Synthesis of Metal Phosphide Nanocrystals. *J. Am. Chem. Soc.* **2007**, *129*, 1896–1897.

(38) Powell, C. J. Beam Effects, Surface Topography, and Depth Profiling in Surface Analysis. Czanderna, A. W., Madey, T. E., Powell, C. J., Eds.; Kluwer Academic Publishers: New York, 2002; pp 67.

(39) White, M. A.; Thompson, M. J.; Miller, G. J.; Vela, J. Got LiZnP? Solution Phase Synthesis of Filled Tetrahedral Semiconductors in the Nanoregime. *Chem. Commun.* **2016**, 3497–3499.

(40) Rao, C. N, R.; Venkataraghavan, R.; Kasturi, T. R. Contribution to the Infrared Spectra of Organosulphur Compounds. *Can. J. Chem.* **1964**, *42*, 36–42.

(41) Thomson, J. W.; Nagashima, K.; Macdonald, P. M.; Ozin, G. A. From Sulfur-Amine Solutions to Metal Sulfide Nanocrystals: Peering into the Oleylamine-Sulfur Black Box. *J. Am. Chem. Soc.* **2011**, *133*, 5036–5041.

(42) Ley, S. V. Comprehensive Organic Functional Group Transformations; Katritzky, A., Taylor, R., Eds.; Springer: New York, 1995; Vol. 2, pp. 137.

(43) Choi, H.; Ko, J.-H.; Kim, Y.-H.; Jeong, S. Steric-Hindrance-Driven Shape Transition in PbS Quantum Dots: Understanding Size-Dependent Stability. *J. Am. Chem. Soc.* **2013**, *135*, 5278–5281.

(44) Owen, J. The Coordination Chemistry of Nanocrystal Surfaces. *Science* **2015**, *347*, 6222, 615–616.

(45) Anderson, N. C.; Hendricks, M. P.; Choi, J. J.; Owen, J. S. Ligand Exchange and the Stoichiometry of Metal Chalcogenide Nanocrystals: Spectroscopic Observation of Facile Metal-Carboxylate Displacement and Binding. *J. Am. Chem. Soc.* **2013**, *135*, 18536–18548.

(46) Burdett, J. K.; Lee, S.; McLarnan, T. J. Coloring Problem. *J. Am. Chem. Soc.* **1985**, *107*, 3083–3089.

(47) Miller, G. J. The “Coloring Problem” in Solids: How It Affects Structure, Composition, and Properties. *Eur. J. Inorg. Chem.* **1998**, 523–536.

(48) White, M. A.; Miller, G. J.; Vela, J. Polytypism and Unique Site Preference in LiZnSb: A Superior Thermoelectric Reveals Its True Colors. *J. Am. Chem. Soc.* **2016**, *138*, 44, 14574–14577.

(49) Gabrelian, B. V.; Lavrentiev, A. A.; Nikiforov, I. Y.; Sobolev, V. V. Effect of Differences in $NaBiS_2$ Structure Fragments on Electronic Properties of Compound. *Bull. Russ. Acad. Sci. Phys.* **2005**, *69*, 4, 668–671.

(50) Hoang, K.; Mahanti, S. D.; Salvador, J. R.; Kanatzidis, M. G. Atomic Ordering and Gap Formation in Ag-Sb-Based Ternary Chalcogenides. *Phys. Rev. Lett.* **2007**, *99,* 156403.

(51) Hoang, K.; Mahanti, S. D. Atomic and Electronic Structures of I-V-VI_2 Ternary Chalcogenides. *J. Sci.: Adv. Mater. Dev.* **2016**, *1*, 51–56.

(52) Kresse, G.; Furthmüller, J. Efficient Iterative Schemes for *Ab Initio* Total-Energy Calculations Using a Plane-Wave Basis Set. *Phys. Rev. B* **1996**, *54*, 16, 11169–11186.

(53) Becke, A. D.; Johnson, E. R. A Simple Effective Potential for Exchange. *J. Chem. Phys.* **2006**, *124*, 221101.

(54) Tran, F.; Blaha, P. Accurate Band Gaps of Semiconductors and Insulators with a Semilocal Exchange-Correlation Potential. *Phys. Rev. Lett.* **2009**, *102*, 226401.

(55) Viñes, F.; Konstantatos, G.; Illas, F. Bandgap Engineering by Cationic Disorder: Case Study on AgBiS2. *Phys. Chem. Chem. Phys.* **2017**, *19*, 27940−27944.

(56) Murphy, C. J.; Buriak, J. M. Best Practices for the Reporting of Colloidal Inorganic Nanomaterials. *Chem. Mater.* **2015**, *27*, 4911–4913.

(57) Singh, D. J. Electronic Structure Calculations with the Tran-Blaha Modified Becke-Johnson Density Functional. *Phys. Rev. B* **2010**, *82*, 205102.

(58) Koller, D.; Tran, F.; Blaha, P. Merits and Limits of the Modified Becke-Johnson Exchange Potential. *Phys. Rev. B* **2011**, *83*, 195134.

Appendix for supporting information

Scheme S1

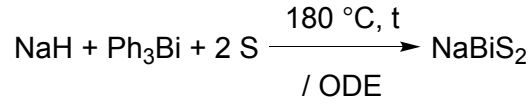

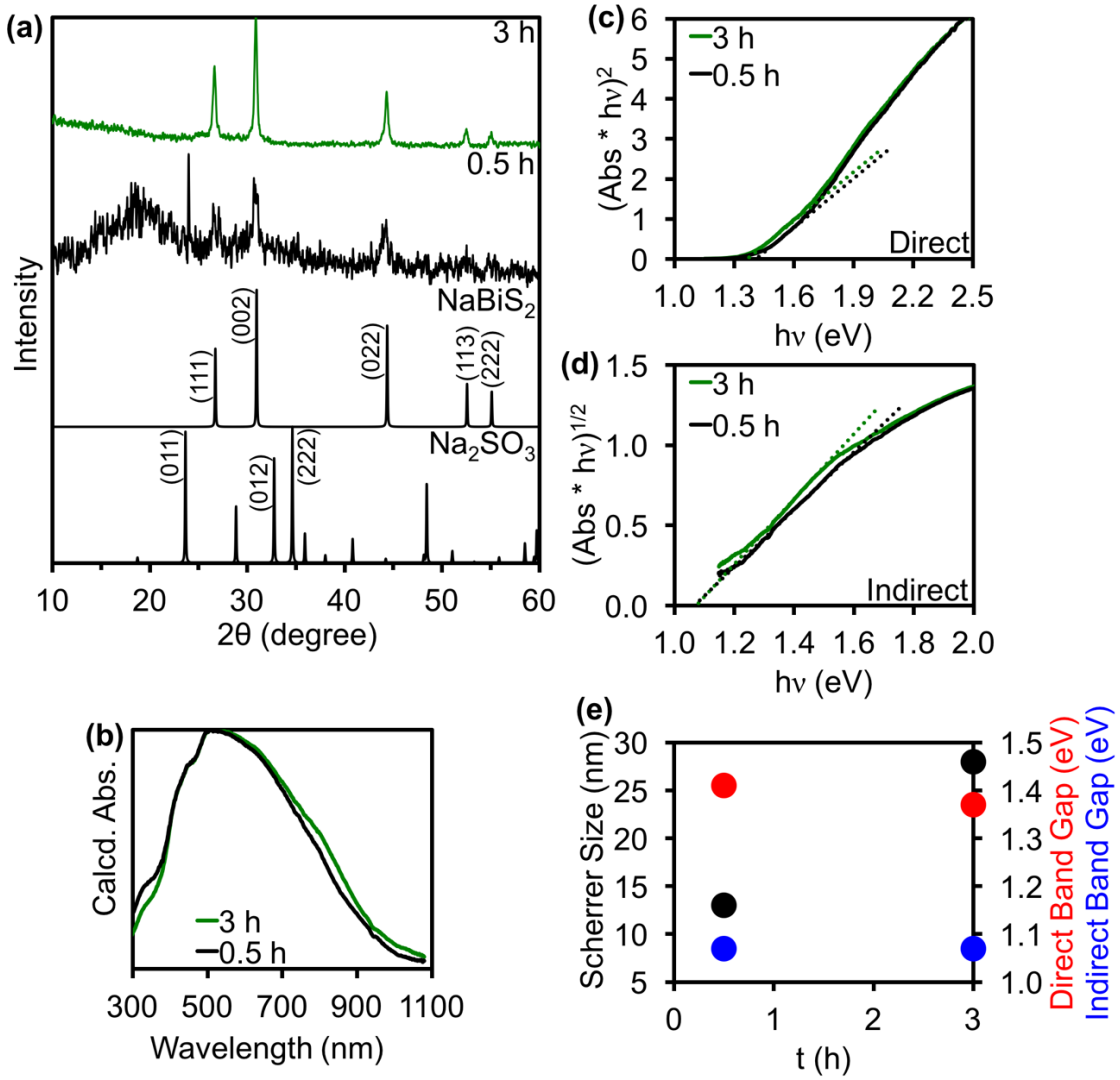

Figure S1. (a) XRD, (b) uncorrected solid-state diffuse-reflectance, (c) direct Tauc plot, and (d) indirect Tauc plot of $NaBiS_2$ prepared in ODE without a ligand at 180 °C for different lengths of time. (e) Comparison between Scherrer size, and direct and indirect band gaps *vs.* time. The minima between 300–500 nm in (b) is the result of an instrument artifact (see Figures S19–21). Tauc plots are calculated from diffuse-reflectance. Prior literature is ambiguous about whether the band gap in $NaBiS_2$ is indirect (by theory)[S1] or direct (by experiment).[S2] Related compounds have both ($RbBiS_2$,[S3] $NaSbS_2$[S4]).

Scheme S2

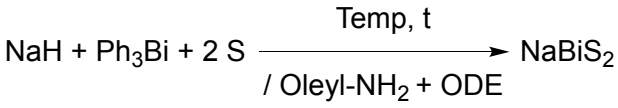

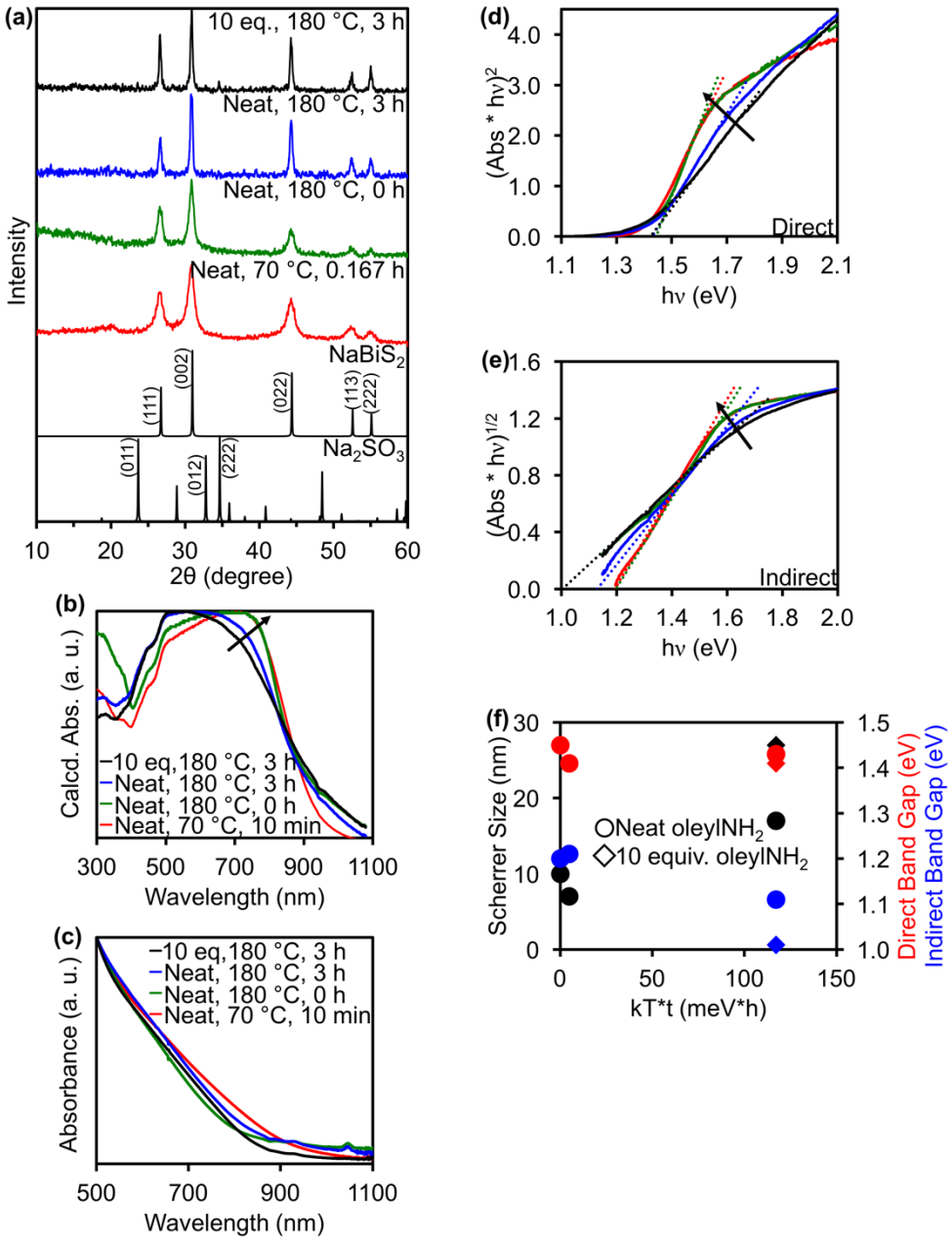

Figure S2. (a) XRD, (b) solution-phase absorption, (c) uncorrected solid-state diffuse-reflectance, (d) direct Tauc plot, and (e) indirect Tauc plot of $NaBiS_2$ prepared with varying $oleylNH_2$ concentration, reaction time, and reaction temperature. (f) Comparison between Scherrer size and

band gaps *vs.* the product of energy and time. The minima between 300–500 nm in (b) is the result of an instrument artifact (see Figures S19–21). Tauc plots are calculated from diffuse-reflectance. Arrows show increasing slope with decreasing Scherrer size. Prior literature is ambiguous about whether the band gap in $NaBiSe_2$ is indirect (by theory[S1]) or direct (by experiment[S2]). Related compounds have both ($RbBiS_2$,[S3] $NaSbS_2$[S4]).

Scheme S3

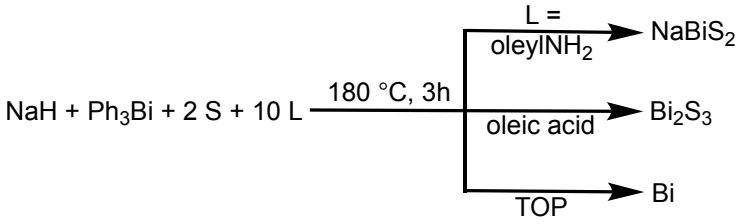

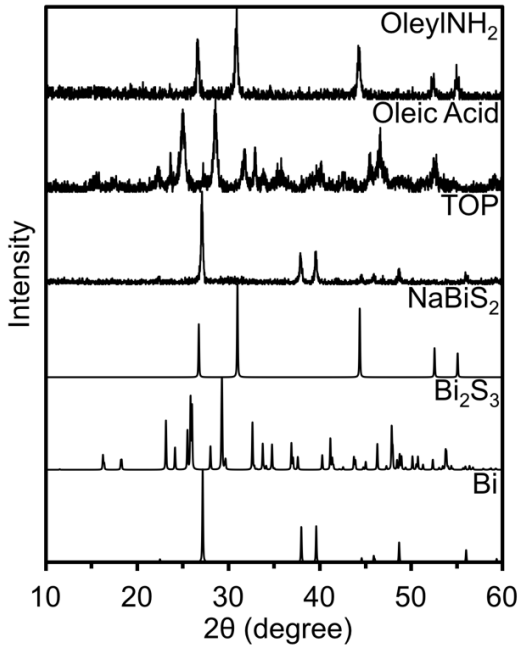

Figure S3. XRD of $NaBiS_2$ prepared with oleylNH_2, oleic acid, or TOP.

Reaction stoichiometry.

The overall chemical equation for the formation of sodium bismuth disulfide from NaH and Ph_3Bi can be easily balanced as:

Scheme S4.

$$3NaH + Ph_3Bi + 3S \longrightarrow NaBiS_2 + 3Ph\text{-}H + Na_2S$$

In this fully balanced redox equation, each hydride ($H:^-$) is a $2e^-$ reductant (to H^+) and each sulfur is a $2e^-$ oxidant. This should not be taken to mean however, that when run in this particular stoichiometry the reaction will proceed smoothly, or at a reasonable rate, or in high yield, etc. Neither kinetics nor thermodynamic information can be assumed from a balanced chemical equation alone. In fact, when we ran this reaction with a 3:1:3 precursor ratio (*i.e.*, 3NaH, 1Ph_3Bi, and 3S equivalents; $[Bi]_{total}$ = 23 mM), the solid isolated after centrifugation contained a complex mixture of products.

However, whenever we ran the reaction with a 1:1:2 precursor ratio (Na:Bi:S; same $[Bi]_{total}$ = 23 mM), the solid isolated after centrifugation contained phase pure ternary $NaBiS_2$. Interestingly, according to the above balanced equation, this new stoichiometry should produce:

Scheme S5.

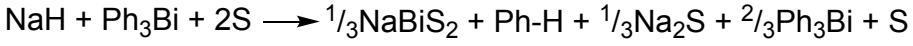

$$NaH + Ph_3Bi + 2S \longrightarrow {}^1/_3NaBiS_2 + Ph\text{-}H + {}^1/_3Na_2S + {}^2/_3Ph_3Bi + S$$

In agreement with this prediction, GCMS analysis of the first supernatant (after removal of solid $NaBiS_2$ by centrifugation) shows the presence of both benzene and unreacted Ph_3Bi. Using a calibration curve made with pure Ph_3Bi gave a GCMS yield of 73% unreacted Ph_3Bi, which is very close to the 67% Ph_3Bi predicted above.

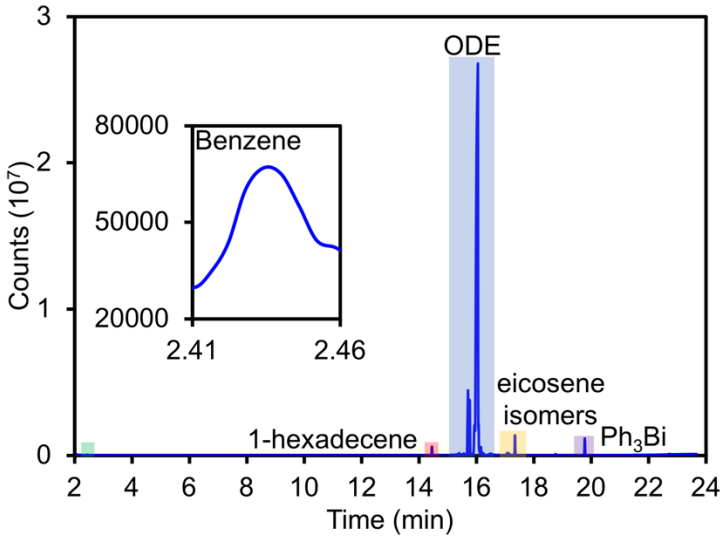

Figure S4. Sample GC-MS trace from the first supernatant after separating $NaBiS_2$ solids by centrifugation; $NaBiS_2$ made with a 1:1:2 ratio of NaH:Ph_3Bi:S in ODE at 180 °C for 3 h ($[Na]_0$ = $[Bi]_0$ = [S]/2 = 23 mM). A calibration curve made with pure Ph_3Bi gives a GCMS yield of 73% unreacted Ph_3Bi.

Scheme S6

$$(x < 1)\ NaH + Ph_3Bi + 2\ S \xrightarrow[/\ ODE]{180\ °C,\ 3\ h} NaBiS_2\ (major) + Bi_2S_3\ (minor)$$

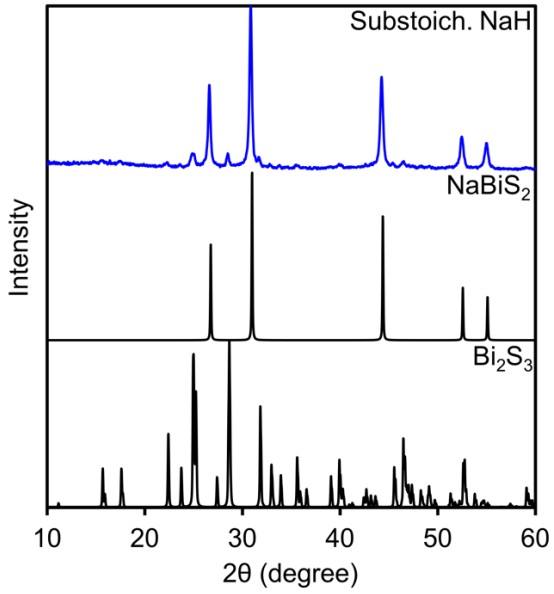

Figure S5. Representative XRD showing formation of binary Bi_2S_3 when substoichiometric NaH is used.

Reaction mechanism.

Main reaction - formation of ternary phase (i-iii):

Scheme S7(i)

$Ph_3Bi + 3H:^- \longrightarrow Bi^0 + 3Ph\text{-}H$

We observe benzene (Ph-H) by GC (see Figure S4 above); we also see the formation of an intermediate Bi^0 metal phase (see Figures S8 and S16 below). The reduction of Bi(III) precursors to metallic Bi^0 is common and well documented to occur with both strong and mild reducing agents, even at relatively low temperatures (50-80 °C).[S5,S6]

Scheme S7(ii)

$H:^- + E \longrightarrow HE^-$ (E = S or Se)

We observe HE^- indirectly by XRD, in the form of its oxidation product, EO_3^{2-} (see Figures S1, S2, and S8).

Scheme S7(iii)

$Bi^0 + E + Na^+ + HE^- \longrightarrow NaBiE_2 + H\bullet$ (E = S or Se)

Although re-oxidizing the intermediate Bi^0 phase back to Bi(III) may at first seem counterintuitive, related redox cycling processes appear to be prevalent in colloidal preparations and have been documented in the literature.[S7,S8]

Secondary reactions - formation of byproducts (iv-vi):

Scheme S7(iv)

$3Bi^0 + 2S \longrightarrow Bi_2S_3$

Bi_2S_3 is observed by XRD whenever we used small, sub stoichiometric amounts of NaH (see Figure S5 above).

Scheme S7(v)

$2HE^- + 3O_2 \longrightarrow 2EO_3^{2-} + 2H^+$ (E = S or Se)

HE^- is observed as Na_2EO_3 by XRD; such HE^- oxidation is well known to occur upon exposure to air.[S9]

Scheme S7(vi)

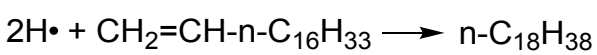

Terminal olefin as hydrogen atom acceptor.

Scheme S8

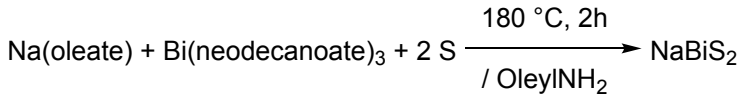

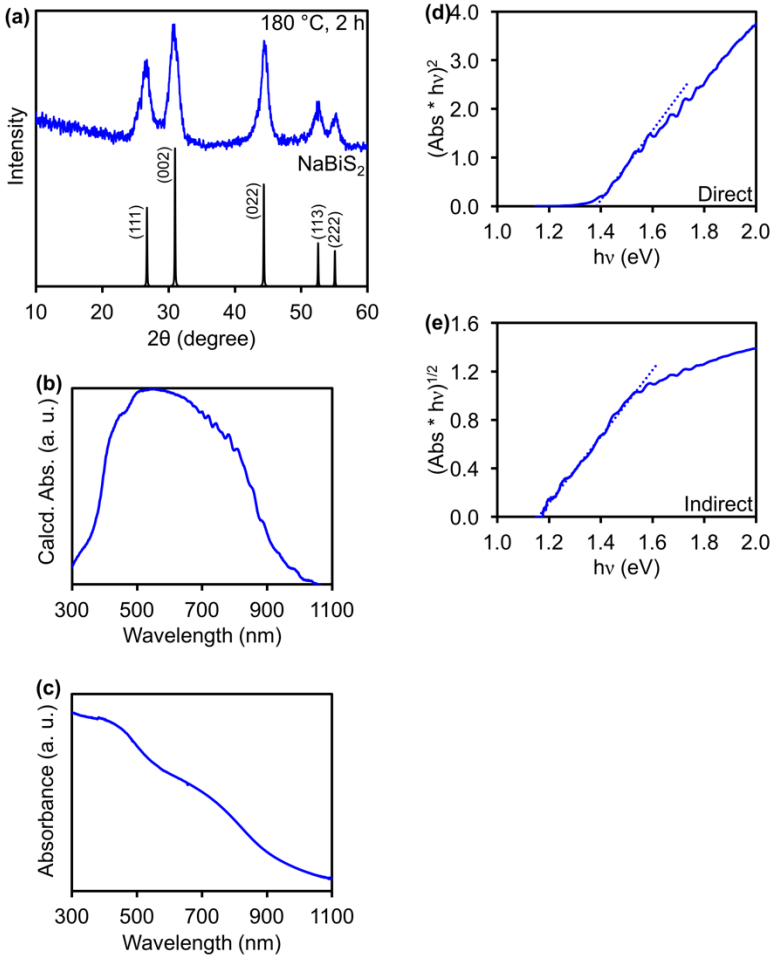

Figure S6. (a) XRD, (b) uncorrected solid-state diffuse-reflectance, (c) solution-phase absorption, (d) direct Tauc plot, and (e) indirect Tauc plot of $NaBiS_2$ prepared in $oleylNH_2$ in the presence of

carboxylates at 180 °C for 2 h. The minima between 300–500 nm in (b) is the result of an instrument artifact (see Figures S19–21). Tauc plots are calculated from diffuse-reflectance. Prior literature is ambiguous about whether the band gap in $NaBiS_2$ is indirect (by theory[S1]) or direct (by experiment[S2]). Related compounds have both ($RbBiS_2$,[S3] $NaSbS_2$[S4]).

Scheme S9

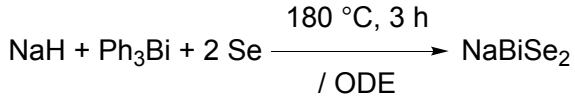

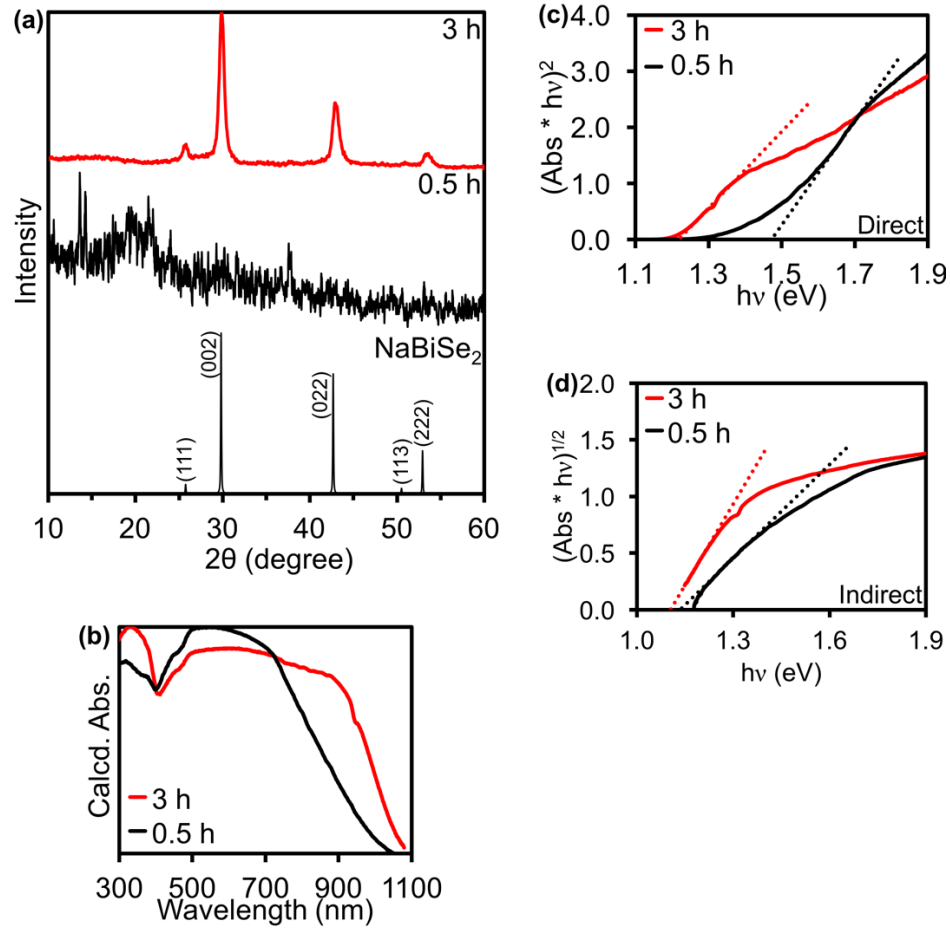

Figure S7. (a) XRD, (b) uncorrected solid-state diffuse-reflectance, (c) direct Tauc plot, and (d) indirect Tauc plot of bulk $NaBiSe_2$ prepared in ODE without a ligand at 180 °C. The minima between 300–500 nm in (b) is the result of an instrument artifact (see Figures S19–21). Tauc plots are calculated from diffuse-reflectance. Prior literature is ambiguous about whether the band gap in $NaBiSe_2$ is indirect (by theory[S1]) or direct (by experiment[S2]). Related compounds have both ($RbBiS_2$,[S3] $NaSbS_2$[S4]).

Scheme S10

$$NaH + Ph_3Bi + 2\ Se \xrightarrow[/\ Oleyl\text{-}NH_2 + ODE]{180\ ^\circ C,\ t} NaBiSe_2$$

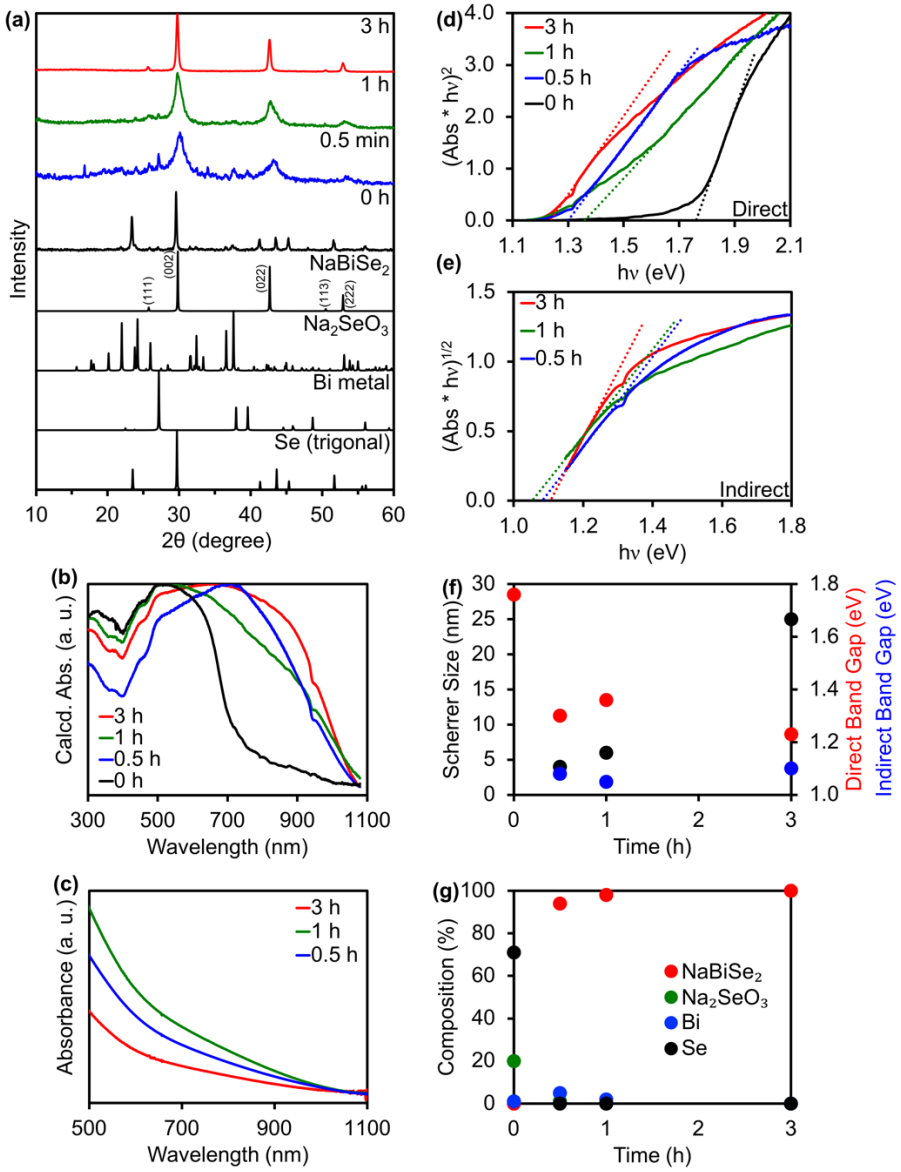

Figure S8. (a) XRD, (b) uncorrected solid-state diffuse-reflectance, (c) solution-phase absorption, (d) direct Tauc plot, and (e) indirect Tauc plot of $NaBiSe_2$ prepared in the presence of oleylNH_2 at 180 °C for 0-3 h. (f) Comparison between Scherrer size and band gaps *vs*.time. (g) Percent composition *vs* time. Trigonal (black) Se has a 1.8 eV direct band gap.[S10] The minima between 300–500 nm in (b) is the result of an instrument artifact (see Figures S19–21). Tauc plots are

calculated from diffuse-reflectance. Trigonal Se is a known direct band gap semiconductor so no indirect band gap is reported for the 0 h sample. Prior literature is ambiguous about whether the band gap in $NaBiSe_2$ is indirect (by theory[S1]) or direct (by experiment[S2]). Related compounds have both ($RbBiS_2$,[S3] $NaSbS_2$[S4]).

Scheme S11

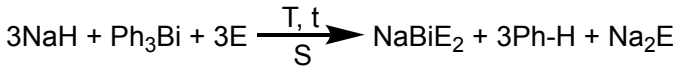

E = S or Se
T = 70–180 °C
S = ODE, oleylNH$_2$, or both

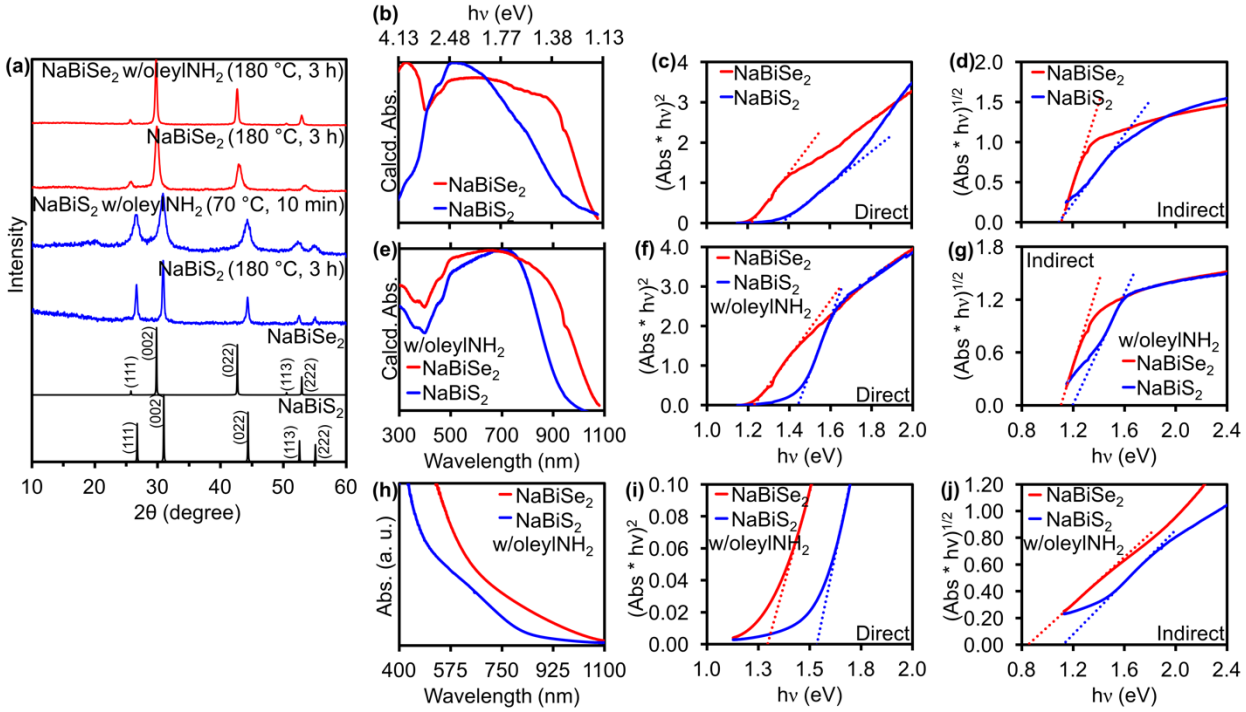

Figure S9. Select data for $NaBiS_2$ and $NaBiSe_2$ prepared with and without oleylNH$_2$. (a) XRD. (b) Uncorrected solid-state diffuse-reflectance, (c) direct Tauc plot, and (d) indirect Tauc plot of $NaBiS_2$ and $NaBiSe_2$ prepared without oleylNH$_2$. (e) Uncorrected solid-state diffuse-reflectance, (h) solution-phase absorption, (f,i) direct Tauc plot, and (g,j) indirect Tauc plot of $NaBiS_2$ and $NaBiSe_2$ prepared in the presence of oleylNH$_2$. The minima between 300–500 nm in (b,e) is the result of an instrument artifact (see Figures S19–21). Tauc plots (c,d) and (f,g) were calculated from diffuse-reflectance (b) and (e), respectively, while (i,j) were calculated from solution absorbance (h).

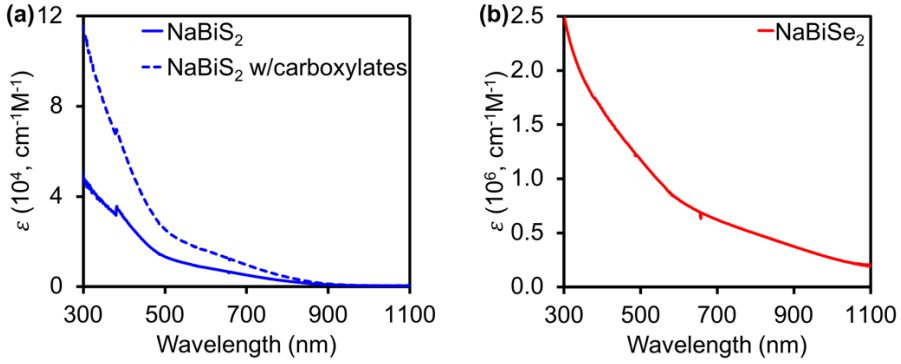

Figure S10. Extinction coefficients of (a) $NaBiS_2$ nanocrystals in presence (4.4±0.7 nm by TEM) and absence (4.2±0.7 nm by TEM) of carboxylates, and (b) $NaBiSe_2$ nanocrystals prepared in the absence of carboxylates (18±1 nm Scherrer size) (all samples made in the presence of oleylNH_2).

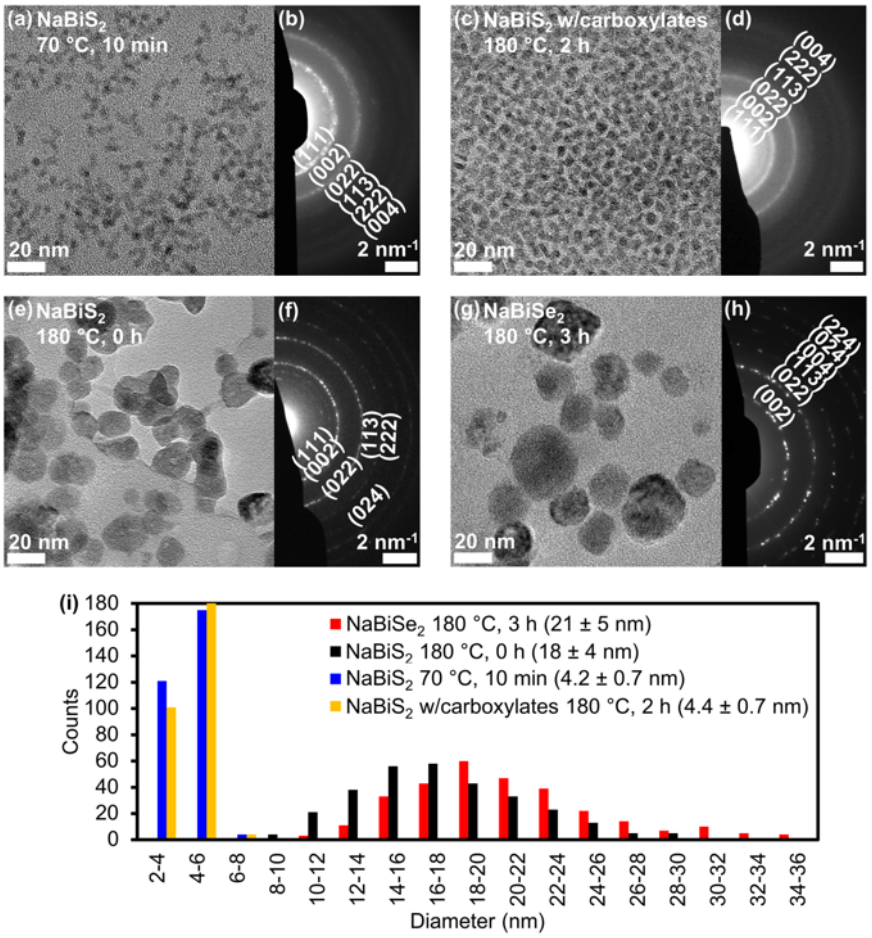

Figure S11. (a) TEM and (b) SAED of $NaBiS_2$ prepared from NaH, Ph_3Bi, and S in neat oleylNH_2 at 70 °C for 10 min. (c) TEM and (d) SAED of $NaBiS_2$ prepared from Na(oleate),

$Bi(neodecanoate)_3$, and S in neat oleylNH_2 at 180 °C for 2 h. (e) TEM and (f) SAED of $NaBiS_2$ prepared from NaH, Ph_3Bi, and S in neat oleylNH_2 at 180 °C for 0 h (immediate cooling). (g) TEM and (h) SAED of $NaBiSe_2$ prepared in the presence of oleylNH_2 at 180 °C for 3 h. (g) Histogram showing size distributions of 300 nanocrystals each for samples shown in (a-h).

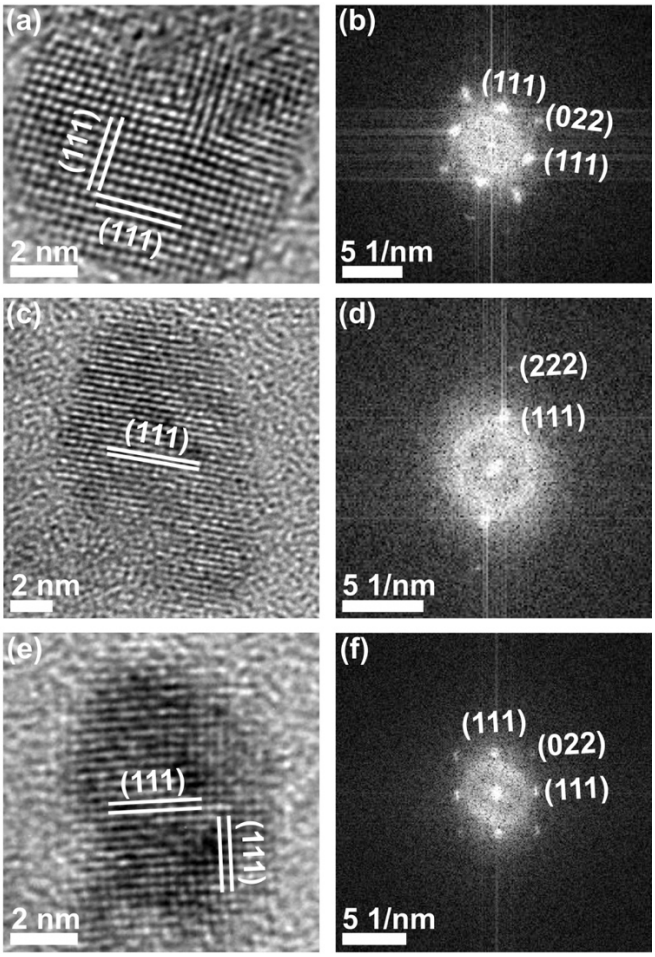

Figure S12. (a,c,e) High-resolution TEM and (b,d,f) respective FFT of three different $NaBiS_2$ nanocrystals prepared in neat oleylNH_2 at 70 °C for 10 min.

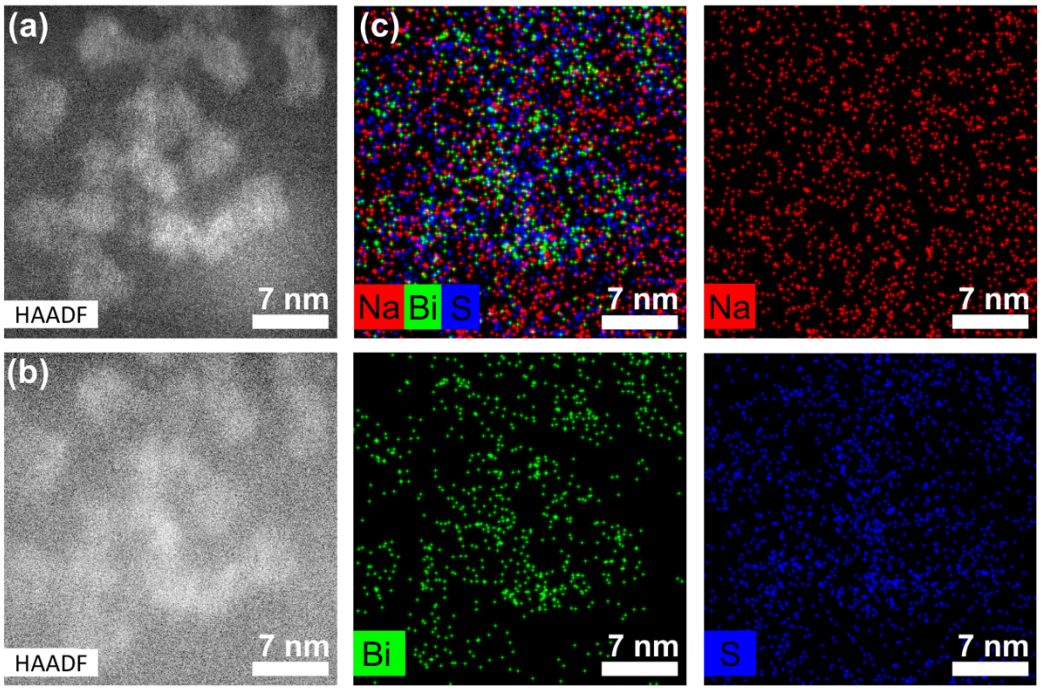

Figure S13. Elemental analysis of $NaBiS_2$ prepared with NaH, Ph_3Bi, and S in neat oleylNH$_2$ at 70 °C for 10 min. Region before (a) and after (b) exposure to the electron beam during EDX elemental mapping (c).

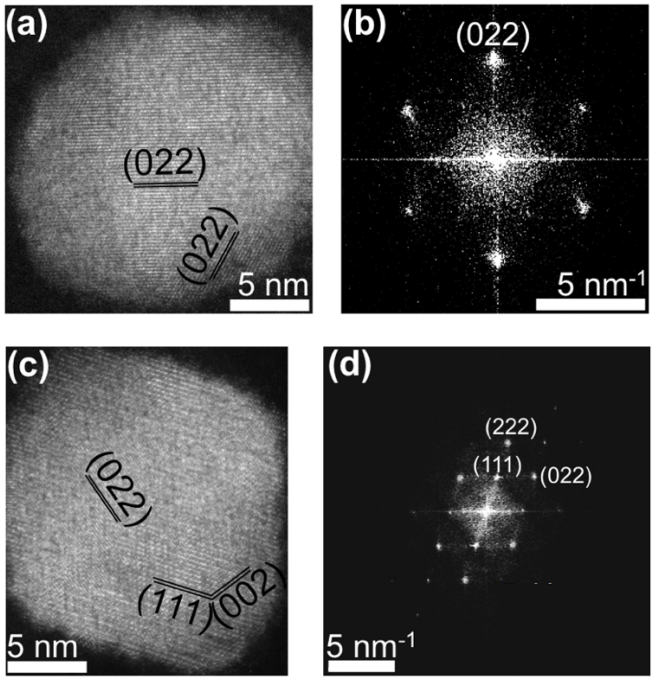

Figure S14. (a,c) High-resolution STEM and (b,d) respective FFT of two different $NaBiSe_2$ nanocrystals.

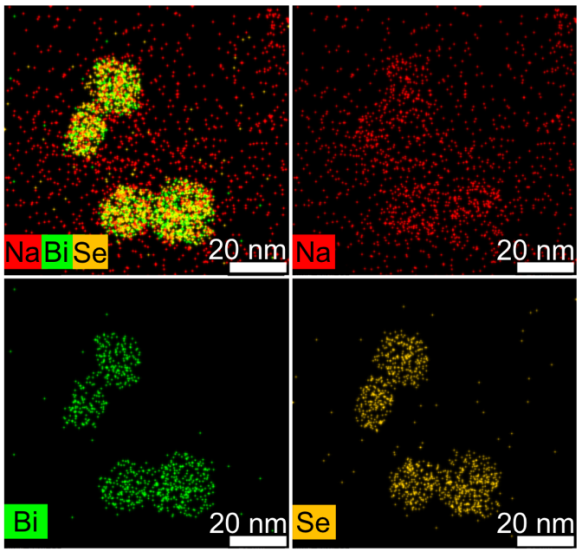

Figure S15. Elemental analysis of $NaBiSe_2$ prepared with oleylNH_2 at 180 °C for 3 h.

Scheme S12

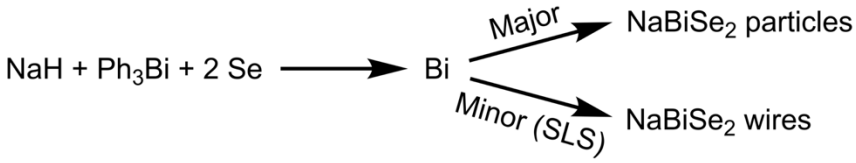

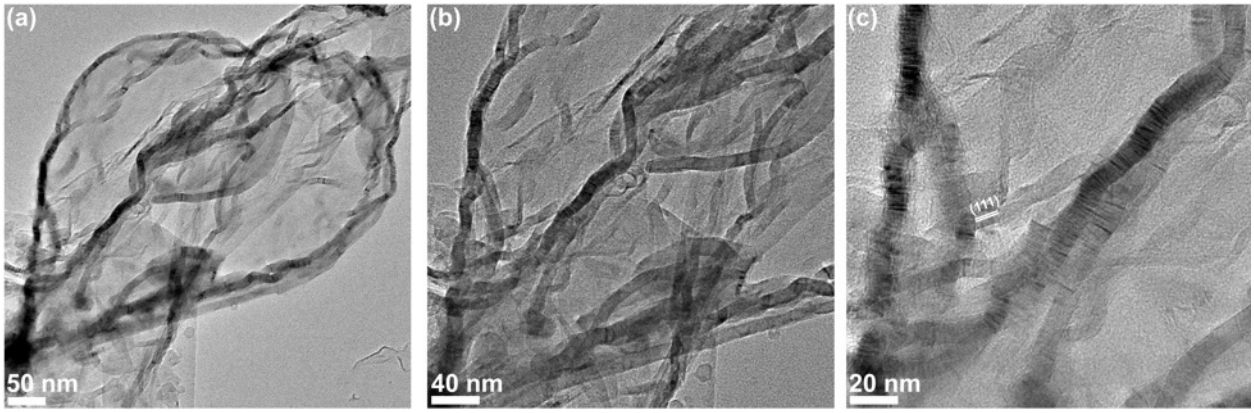

Figure S16. Select TEM of $NaBiSe_2$ prepared in ODE without a ligand that show: (a) plates and wires, (b) wires with seeds, and (c) wires with (111) lattice fringes along the nanowire diameter. We attribute the formation of wires to solution-liquid-solid (SLS) growth *via* Bi-metal seeds (Scheme S12).[S11,S12]

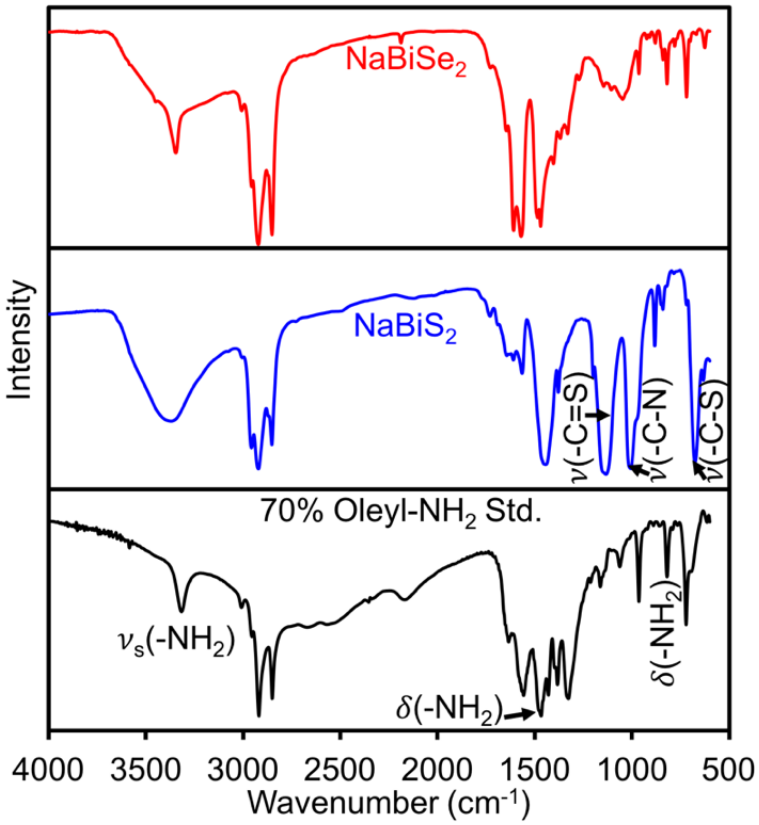

Figure S17. FTIR of $NaBiS_2$ prepared in neat oleylNH_2 at 180 °C for 0 h and $NaBiSe_2$ nanocrystals prepared in the presence of oleylNH_2 at 180 °C for 3 h. $NaBiS_2$ sample shows strong peaks at 1133 cm^{-1}, 1007 cm^{-1}, and 675 cm^{-1} that are consistent with C=S, C-N, and C-S stretching vibrational modes.[S13] These modes are consistent with the presence of thioamides, amidines, and alkene cross-linking by H_2S,[S14] which are all produced in sulfur-alkylamine solutions heated above 130 °C.[S15]

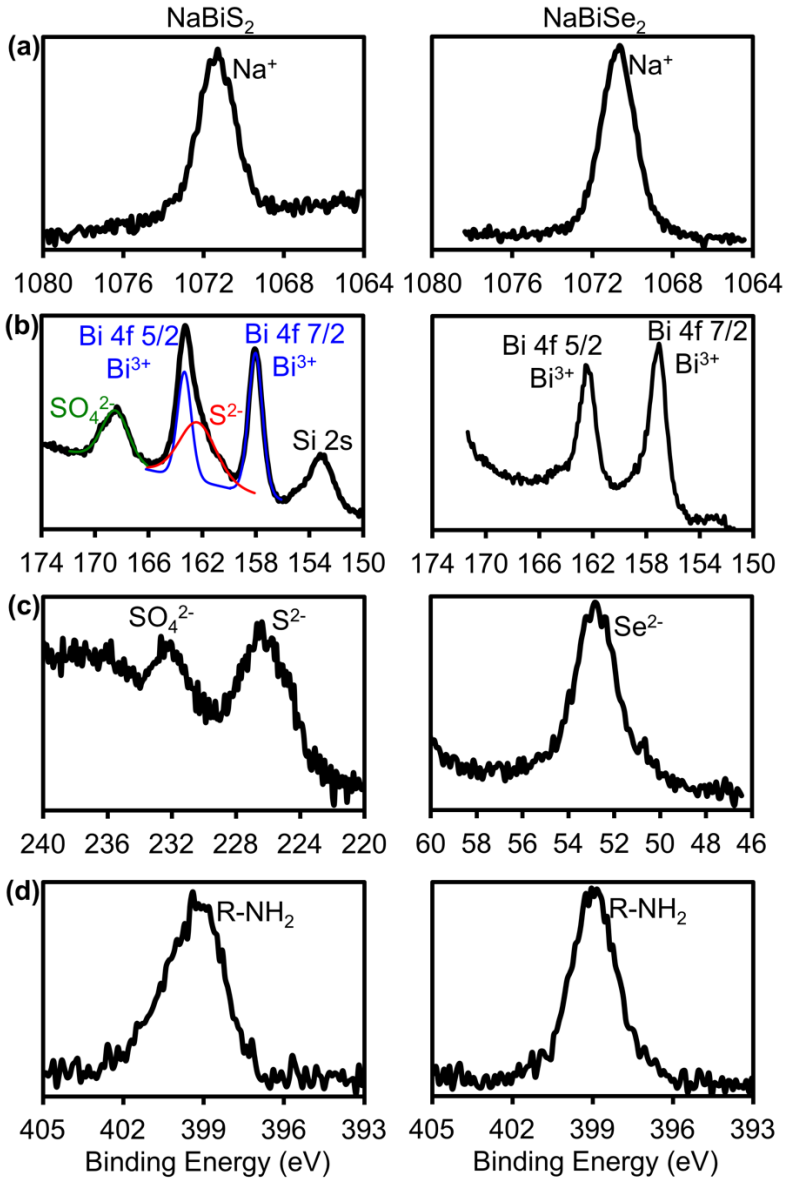

Figure S18. XPS data of $NaBiE_2$ prepared in the presence of oleylNH_2: (a) Na 1s region, (b) Bi 4f and S 2p region, (c) S 2s region (left) and Se 3d region (right), (d) N 1s region. In (b), the Bi 4f and S 2p regions overlap, and the Si 2s peak is from the substrate (data collected *ca.* 20 min after exposure to air).

Table S1. XPS Binding Energies of $NaBiE_2$ Nanocrystals and Relevant Species.

Sample	Na 1s (eV)	Bi 4f 5/2 (eV)	Bi 4f 7/2 (eV)	S 2p SO_4^{2-} (eV)	S 2p SO_3^{2-} (eV)	S 2s S^{2-} (eV)	Se 3d (eV)	N 1s (eV)
$NaBiS_2$	1071.4	163.3	158.1	168.4	-	162.6	-	399.2
$NaBiSe_2$	1070.7	162.6	157.1	-	-	-	52.8	399.2
Literature[S16]	1070.5-1075	162-166	157-161	168-171	165-167.5	160-164	54-60	398-400

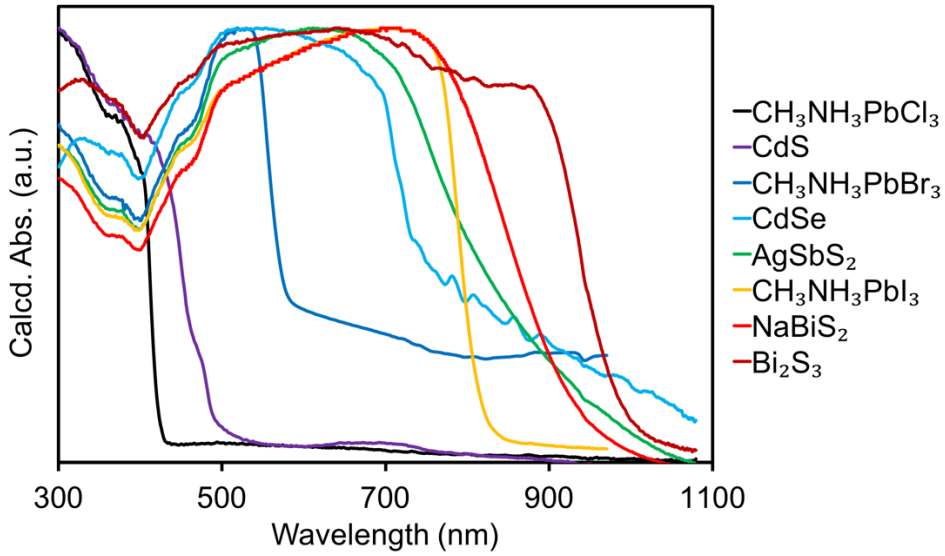

Figure S19. Solid-state diffuse-reflectance collected for several semiconductors with a wide range of absorption onsets (different band gaps). The apparent absorption minima between 300–500 nm is observed across all samples, clearly indicating that these correspond to an instrument artifact.

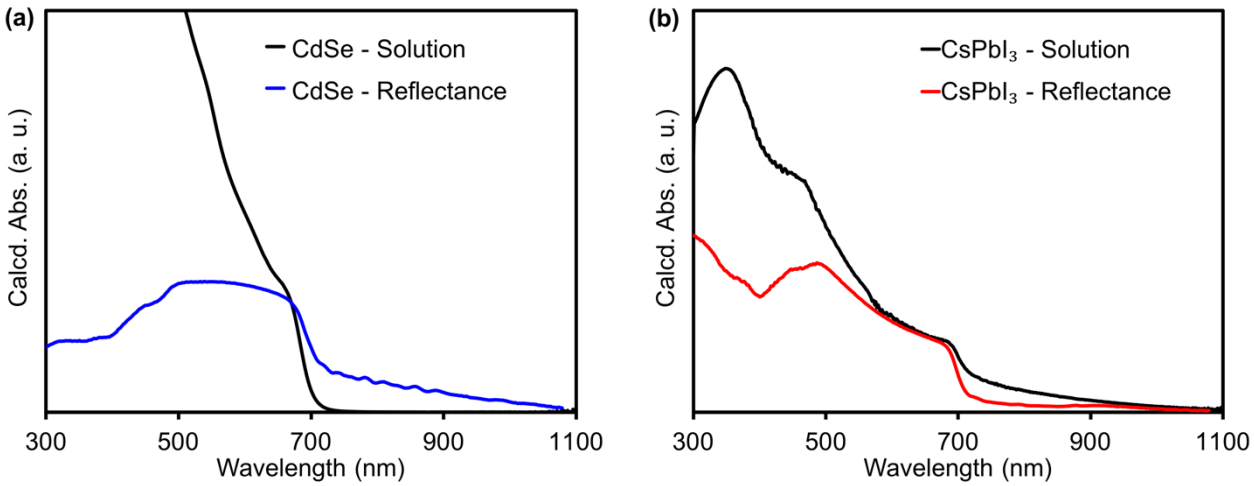

Figure S20. Solution-phase absorption and solid-state diffuse-reflectance collected for (a) CdSe and (b) $CsPbI_3$. Dividing the solution-phase data by the solid-phase data in each case below the first excitonic peak, and taking the average of the two samples gave us an approximate correction factor, which we could use to correct the diffuse-reflectance data (for example, see Figure S21 and Figure 2b).

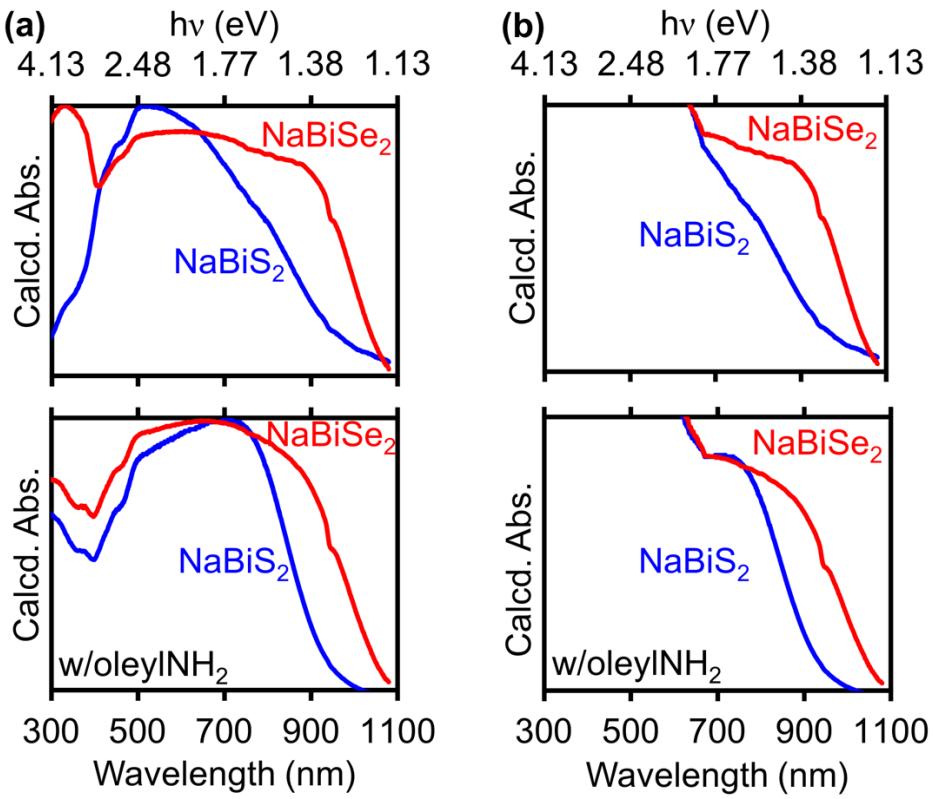

Figure S21. Comparison of solid-state diffuse-reflectance before (a) and after (b) applying the correction mentioned above (Figure S20).

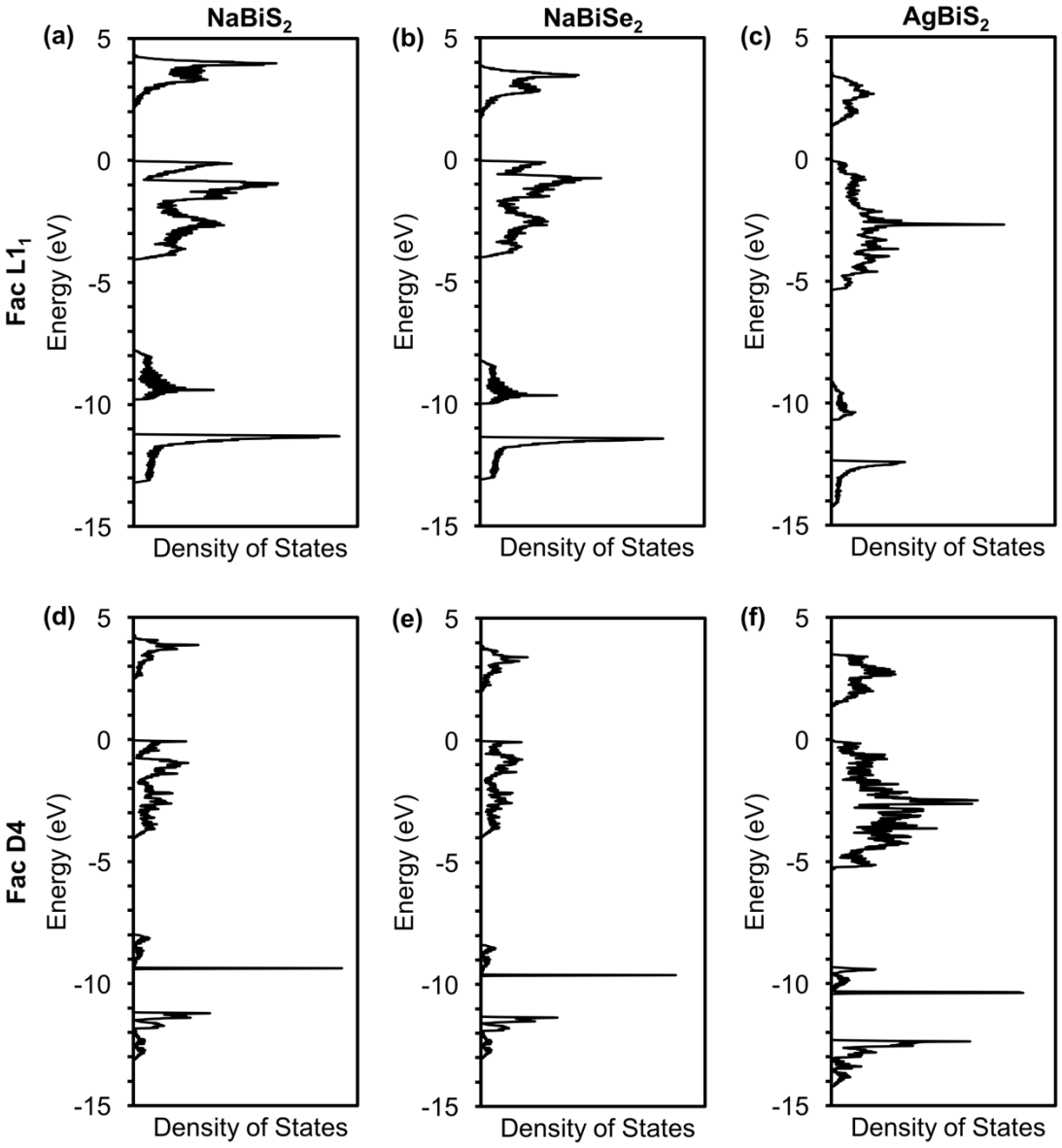

Figure S22. Density of states (DOS) of the two lowest-energy structures (3:3 fac $L1_1$ and 3:3 fac D4, see Figure 5) of (a) $NaBiS_2$ and (b) $NaBiSe_2$. DOS were performed on 2x2x2 supercells using VASP[S17] with TB-mBJ[S18,S19] and an 11x11x11 Monkhorst-pack k-point grid (see Methods).

Table S2. Experimental *vs.* Theoretical Band Gaps for $ABiE_2$ Compounds.

Band gap	Experimental (eV)		Calculated (eV)[a]					
Compound	No ligand ("bulk")	Nano	TB-mBJ, exptl.[b]		TB-mBJ, geom.[c]		LDA	
			Fac $L1_1$ (%)[d]	Fac D4	Fac $L1_1$	Fac D4	Fac $L1_1$	Fac D4
$NaBiS_2$	1.37[e]	1.45[f]	2.12 (55)	2.46	2.21	2.53	1.35	1.70
$NaBiSe_2$	1.23[e]	1.26[f]	1.63 (33)	1.97	1.72	2.03	1.00	1.35
$AgBiS_2$	0.8[e,S20]	1.3[S21]	1.22 (53)	1.33	1.02	1.26	0.34	0.55

[a]See methods. [b,c]TB-mBJ[S18,S19] using the experimental-[b] or geometry-optimized[c] lattice parameter. [d]Over-estimation relative to experimentally-observed "bulk" value. [e]Prepared without added ligand. [f]Soluble nanocrystals prepared in the presence of oleylNH_2.

References

(S1) Gabrel'yan, B. V.; Lavrentiev, A. A.; Nikiforov, I. Y.; Sobolev, V. V. Electronic Energy Structure of $MBiS_2$ (M = Li, Na, K) Calculated with Allowance for the Difference Between the M-S and Bi-S Bond Lengths. *J. Struct. Chem.* **2008**, *49*, 5, 788–794.

(S2) Kang, S.; Hong, Y.; Jeon, Y. A Facile Synthesis and Characterization of Sodium Bismuth Sulfide ($NaBiS_2$) Under Hydrothermal Condition. *Bull. Korean Chem. Soc.* **2014**, *35*, 6, 1887–1890.

(S3) Brandt, R. E.; Stevanović, V.; Ginley, D. S.; Buonassisi, T. Identifying Defect-Tolerant Semiconductors with High Minority Carrier Lifetimes: Beyond Hybrid Lead Halide Perovskites. *MRS Commun.* **2015**, *5*, 2, 265–275.

(S4) Sun, J.; Singh, D. J. Electronic Properties, Screening, and Efficient Carrier Transport in $NaSbS_2$. *Phys. Rev. Appl.* **2017**, *7*, 024015.

(S5) Son, J. S.; Park, K.; Han, M.-K.; Kang, C.; Park, S.-G.; Kim, J.-H.; Kim, W.; Kim, S.-J.; Hyeon, T. Large-Scale Synthesis and Characterization of the Size-Dependent Thermoelectric Properties of Uniformly Sized Bismuth Nanocrystals. *Angew. Chem. Int. Ed.* **2011**, *50*, 1363–1366.

(S6) He, M.; Protesescu, L.; Caputo, R.; Krumeich, F.; Kovalenko, M. V. A General Synthesis Strategy for Monodisperse Metallic and Metalloid Nanoparticles (In, Ga, Bi, Sb, Zn, Cu, Sn, and Their Alloys) via in Situ Formed Metal Long-Chain Amides. *Chem. Mater.* **2015**, *27*, 635–647.

(S7) Mobarok, M. H.; Luber, E. J.; Bernard, G. M.; Peng, L.; Wasylishen, R. E.; Buriak, J. M. Phase-Pure Crystalline Zinc Phosphide Nanoparticles: Synthetic Approaches and Characterization. *Chem. Mater.* **2014**, *26*, 1925–1935.

(S8) Henkes, A. E.; Vasquez, Y.; Schaak, R. E. Converting Metals into Phosphides: A General Strategy for the Synthesis of Metal Phosphide Nanocrystals. *J. Am. Chem. Soc.* **2007**, *129*, 1896–1897.

(S9) Sada, E.; Kumazawa, H.; Hashizume, I.; Shimono, M.; Sakaki, T. Oxidation of Aqueous Sodium Sulfide Solutions with Activated Carbon. *Ind. Eng. Chem. Res.* **1987**, *26*, 1782–1787.

(S10) Berger, L. *Semiconductor Materials;* CRC Press: Boca Raton, 1997; pp. 87.

(S11) Wang, F.; Dong, A.; Buhro, W. E. Solution-Liquid-Solid Synthesis, Properties, and Applications of One-Dimensional Colloidal Semiconductor Nanorods and Nanowires. *Chem. Rev.* **2016**, *116*, 10888–10933.

(S12) Tongying P., Zhukovskyi M., Kuno M. Synthesis and Application of Solution-Based II–VI and IV–VI Semiconductor Nanowires. In Anisotropic Nanomaterials. Prepara-tion, Properties, and Applications; Li, Q., Eds.; Springer: Cham, 2015; Chapter 4, pp 119–156.

(S13) Rao, C. N, R.; Venkataraghavan, R.; Kasturi, T. R. Contribution to the Infrared Spectra of Organosulphur Compounds. *Can. J. Chem.* **1964**, *42*, 36–42.

(S14) Ley, S. V. Comprehensive Organic Functional Group Transformations; Katriktzky, A., Taylor, R., Eds.; Springer: New York, 1995; Vol. 2, pp. 137.

(S15) Thomson, J. W.; Nagashima, K.; Macdonald, P. M.; Ozin, G. A. From Sulfur-Amine Solutions to Metal Sulfide Nanocrystals: Peering into the Oleylamine-Sulfur Black Box. *J. Am. Chem. Soc.* **2011**, *133*, 5036–5041.

(S16) Moulder, J. F.; Stickle, W. F.; Sobol, P. E.; Bomben, K. D. *Handbook of X-ray Photoelectron Spectroscopy: A Reference Book of Standard Spectra for Identification and Interpretation of XPS Data*; Chastain, J., King, R. C. Jr., Eds.; ULVAC-PHI: Japan, 1995.

(S17) Kresse, G.; Furthmüller, J. Efficient Iterative Schemes for Ab Initio Total-Energy Calculations Using a Plane-Wave Basis Set. *Phys. Rev. B* **1996**, *54*, 16, 11169–11186.

(S18) Becke, A. D.; Johnson, E. R. A Simple Effective Potential for Exchange. *J. Chem. Phys.* **2006**, *124*, 221101.

(S19) Tran, F.; Blaha, P. Accurate Band Gaps of Semiconductors and Insulators with a Semilocal Exchange-Correlation Potential. *Phys. Rev. Lett.* **2009**, *102*, 226401.

(S20) Guin, S. N.; Biswas, K. Nanoscale Stabilization of Nonequilibrium Rock Salt BiAgSeS: Colloidal Synthesis and Temperature Driven Unusual Phase Transition. *Chem. Mater.* **2013**, 25, 3225–3231.

(S21) Bernechea, M; Miller, N. C.; Xercavins, G.; So, D.; Stavrinadis, A.; Konstantatos, G. Solution-Processed Solar Cells Based on Environmentally Friendly $AgBiS_2$ Nanocrystals. *Nat. Photon.* **2016**, *10*, 521–526.

CHAPTER 5

GENERAL CONCLUSIONS

In conclusion, this dissertation described the synthesis and properties of two emerging multinary families of semiconductors that exhibit properties beneficial to technologies that can generate energy cleanly and efficiently without the release of harmful pollutants into the environment: halide perovskites and alkali bismuth dichalcogenides.

We initially showed by ^{207}Pb solid state nuclear magnetic resonance (ssNMR) spectroscopy that when methylammonium lead mixed halide perovskites are prepared in solution, dopants and semicrystalline phases survive and persist even upon annealing. We developed a novel solid phase synthesis that successfully eliminates semicrystalline phases and show that dopants are an inherent property in the mixed-halide perovskites because of the presence of miscibility gaps and spontaneous spinodal decomposition at room temperature. These results suggest that better optoelectronic properties and improved device performance may be achieved through careful manipulation of the different phases and nanodomains present in these materials.

Many of the best-performing, technologically-relevant semiconductors are composed of toxic (Cd, Pb, As) or relatively scarce (Li, In) elements. Therefore, there is need to develop new semiconductor families composed of environmentally friendly and Earth-abundant elements. Toward this aim, we described the nanocrystalline synthesis of two new ternary semiconductor families: cesium germanium halide perovskites and alkali bismuth dichalcogenides. We showed that size control of cesium germanium halide perovskite nanocrystals can be achieved by varying the concentration of cysteammonium halide ligands. We successfully doped Mn^{2+} (29% in bulk and 16% in nano samples) into the halide lattice for the first time. We also reported a facile, low-temperature (< 100 °C), and size-tunable (4–28 nm) solution phase synthesis of ternary alkali bismuth dichalcogenides. We observed 1.20–1.45 eV band gaps that all fall within the ideal range for solar cells with high extinction coefficients in the 10^4–10^6 cm^{-1} M^{-1} range. We computationally investigated the lowest energy superstructures that result from “coloring” caused by mixed-cation sites present in the rock salt lattice. The novel syntheses reported in this dissertation unlock two new classes of low cost and environmentally friendly semiconductors that show properties of interest for applications in energy conversion.